UNIVERSITY OF BERGEN

Measurements of the Photonuclear Neutron Yield During Radiotherapy Using Bubble Detectors and Thermoluminescence Detectors

Master Thesis in Nuclear Physics

by

Camilla Hanquist Stokkevåg

Department of Physics and Technology
February 2010

Gratefully I dedicate this work to my parents,
Johannes Stokkevåg and Irmelin Hanquist Larsen;
for beginning my education,
for encouraging me on the way,
and for always to remain an inspiration to continue.

Acknowledgements

To begin with I would like to thank everyone who has contributed to this thesis.

Thank you Professor Dieter Röhrich for introducing me to this subject, and for making my master studies an interesting experience as well as giving me the opportunity to work with great people.

Dr. Scient Odd Harald Odland has been a great contribution to this work. I believe you have an extraordinary ability of bringing out the best in people. Thank you for your encourage and enthusiasm.

Thank you Kristian Ytre-Hauge for including me into what was initially your project. It has been a great time working with you these last two years and I do hope I have the opportunity to work with you in the future.

A great thank you to the Medical Physics Section at HUS for the contributions during this work. Thanks to Anfinn Mehus for supporting the project. Thank you Finn Totland for being helpful in every issue, especially concerning the TLD system. Thank you Dagfinn Knutsen for being helpful in constructing the phantoms used in the measurements of this work. Thank you to all the physicists and radiation therapists for being welcoming towards us during our time a HUS.

Thank you Jon Rambæk, Sverre Hval and Espen Graffer for all your assistance and favour during the calibration that was performed at IFE.

A special thanks to Dieter Schardt for introducing me to the work performed at GSI. This has been a great contribution in obtaining insight in procedures related to carbon ion therapy and attaining a conception of the research performed in the GSI biophysics group.

Thank you to senior engineer Jon Wikne at the University of Oslo for helping me at the beginning of the project.

At IFT, thank you to the nuclear physics group. Thank you Njål Brekke and Dominik Fehlker at the detector laboratory for your assistance. Thank you Sebastian Bablok, Gaute Øvrebekk, Ketil Røed, Kyrre Skjerdal and Henrik Qvigstad for always being helpful.

Thank you Eivind Larsen for assisting under the calibration at IFE.

Hege Erdal deserves a great thanks for always being supportive and helpful.

Thanks to Lars Husdal for being helpful with the reactor physics.

Thank you everyone in room 534 and the rest of the 5th floor.

To Kristine Helle and Anja Heggen I am grateful for your friendship throughout the years we have studied together at UiB.

Takk til kvinnene i mitt liv: Ingeborg, Helene, Helene, Thale, Liva, Hege, Signe og Charlie. Ingenting hadde vært det samme uten dere!

Sist men ikke minst takk til mannen i mitt liv, Rune, for din ubetingede støtte og oppmuntring.

Bergen, 21st February, 2010

Camilla Hanquist Stokkevåg

Abstract

Medical linear accelerators (linacs) used for radiotherapy with photons produce an undesirable neutron contribution as treatment energies exceed the (γ,n) threshold of the high-Z constituents of the linac. Secondary neutrons in radiotherapy can contribute to an additional dose outside the treatment volume in the patient. Treatment techniques offering improved confinement of the dose to the target volume are rapidly evolving and will contribute differently to the production of neutron doses outside the volume at target.

The intention in this work has been two-fold: (1) Investigation of the characteristics and the responses of the detectors applied. (2) Measurements of the secondary neutron yield outside the treatment volume of a 15 MV photon beam produced by a Varian 23iX medical linac at Haukeland University Hospital (HUS). Neutron yields measured during the treatment techniques Three-Dimensional Conventional Radiation Therapy (3D-CRT) are compared to Intensity Modulated Radiation Therapy (IMRT).

The neutron measurements were performed using bubble detectors and Thermoluminescence Detectors (TLDs). The TLD-600 is photon and thermal neutron sensitive, and the TLD-700 is photon sensitive. Pairs of TLDs were applied together in order to discriminate against the photon component of the mixed field. The bubble detectors employed were the Bubble Detector Spectrometer (BDS) used for obtaining information on the neutron energy spectrum, and the Bubble Detector Thermal (BDT) sensitive to thermal neutrons.

The response of the detectors was also measured in the mixed photon thermal-neutron field of the nuclear reactor at Institute for Energy Technology (IFE) at Kjeller (Norway). The BDS detectors were found to be sensitive in this field, either to neutrons with lower energy than the discrimination thresholds given from the vendor or to the photon component of the field. The BDT set was calibrated in this field and the sensitivity obtained from the measurements was four times higher than the calibration factors supplied by the manufacturer. The TLDs applied in the reactor field detected a strong photon background, which made reliable photon discrimination in the TLD signal a challenge.

The spatial distribution of the neutrons produced by the medical linac was measured outside the target volume with TLDs positioned in a plastic phantom. The neutrons were principally detected in the outer layers of the phantom, close to the treatment head where the neutrons are produced.

Two dose plans were created in the Eclipse dose plan system in order to compare the neutron yield during the IMRT and 3D-CRT treatment techniques. Measurements were performed in a solid state plastic phantom, with TLD and BDS detectors situated outside the photon treatment field. The IMRT dose plan resulted in a higher neutron dose than the dose produced during the 3D-CRT dose plan. The ratio of the neutron dose produced during the delivery of the two plans scales roughly with the ratio of the radiation output of the linac; the Monitor Units (MUs). The neutron fluences measured were on the order of 10^7 n/cm^2 per treatment Gy delivered to the target volume. For a full treatment of 70 Gy, the additional neutron doses measured were 0.2±0.1 Sv for the 3D-CRT plan and 0.4±0.3 Sv for the IMRT plan. Two characteristic features of the neutron energy spectrum were observed; the low energy continous distibution from neutron evaporation processes and a rather distinct peak from direct neutron knock-out processes.

The sensitivity of the detectors to neutron energies, and potentially to photons, should be further investigated with respect to the correspondence between the response to fluence and dose. To obtain further information of the neutron energy spectrum, the use of TLDs with moderators of different sizes can be an alternative method.

Contents

Chapter 1

Introduction

Cancer is today one of the main causes of death worldwide. The current cancer treatment methods include surgical removal, chemotherapy, radiation therapy, or combinations of these. About 50% of all cancer patients receive radiation therapy. During radiotherapy, the overall objective is to deliver a treatment dose to the target volume, and at the same time spare the surrounding healthy tissue as much as possible.

The most common form of radiation therapy is the use of photon beams produced by medical linear accelerators (linacs). In order to limit the photon beam to the target volume, collimators of tungsten and lead are used to shape the beam. As photon energies exceed the photonuclear threshold of the collimator material, production of undesirable neutrons will take place [1]. Neutrons are a significant secondary particle due to their long range and relatively high biological effect in tissue [2]. Therefore neutrons will contribute to the dose depositions at photon energies exceeding 7-8 MeV. The exposure to low doses of ionizing radiation deposited outside the target volume is associated with an elevated risk of irradiation induced secondary cancer, even many years after the initial exposure [3].

In this thesis, the secondary neutron yield from a Varian medical linac, used for cancer treatment at HUS, has been investigated. The detectors have been positioned in solid state plastic phantoms situated in photon beams of energies up to 15 MeV, and measurements have been performed applying different field configurations. In order to investigate the spatial distribution of thermal neutrons outside the treatment volume, Thermoluminescence Detector (TLD) measurements were performed in multiple in-phantom positions outside the target volume. To compare the neutron fluences and doses emerging from the two treatment configurations Three-Dimensional Conformal Radiotherapy (3D-CRT) and Intensity Modulated Radio Therapy (IMRT), treatment plans were constructed in a dose plan system, and the treatments were executed during neutron measurements.

Depending on the treatment technique applied during the radiation therapy, different dose contributions from neutrons will result. The 3D-CRT method employs Multi Leaf Collimators (MLCs) in a static manner during the treatment, of which the dose is delivered from multiple angles to distribute the unavoidable entrance dose to the tissue surrounding the treatment volume. IMRT is another beam delivery technique that has been implemented within radiotherapy during the last two decades. In IMRT, the beam intensity can be varied across the treatment field utilizing dynamic MLCs. In this way the radiation dose can be delivered to the target volume whilst maintaining quite sharp dose gradients with respect to the nearby healthy tissue or critical organs close to the target volume. However, the extended use of collimators during IMRT requires several times higher radiation output compared to 3D-CRT. With increasing radiation output from the linac, the dose contribution from neutrons is expected to increase [4].

In order to investigate the neutron dose contribution from medical linacs, suitable detectors for such an environment must be obtained. Measurements of the neutron fluences in the surrounding of a medical linac can be a challenge. The high photon background requires the detectors to have good photon discrimination. Due to the pulsed nature of the photon beam, passive detectors are preferred to avoid the dead time losses associated with active devices. The biological effects of neutrons are energy dependent, and a detection method that enables a neutron energy spectrum to be obtained is of great significance.

The aim of this thesis has been two-fold; (1) to examine the properties of the neutron detectors used, in order to gain a better comprehension of their response and manner of operation, and (2) to investigate the neutron contribution from a medical linac by applying different photon field configurations.

The detectors used in this work are i) two types of bubble detectors and ii) pairs of TLDs, both are passive devices. The bubble detectors used are able to discriminate against photons [5], whereas for the TLD pairs applied, the photon component of the signal can be subtracted. Of the bubble detectors, one set was mainly sensitive to thermal neutrons; Bubble Detector Thermal (BDT), and one set was intended for spectrometry; Bubble Detector Spectrometer (BDS). The BDS detectors cover the neutron energy spectrum and consist of subsets of detectors having individual energy thresholds, with the lower threshold set starting at 10 keV. Several measurements were performed in this thesis in order to investigate the detector properties; both in the surroundings of a photon field producing medical linac at Haukeland University Hospital (HUS), Bergen, and in the field of the nuclear reactor Joint Establishment Experimental Pile (JEEP II) at the Institute for Energy Technology (IFE) outside Oslo.

The investigations of detector properties is a continuation of the master thesis work of K. Ytre-Hauge, released May 2009 [6]. This study included tests of durability and temperature dependence of the bubble detectors, and these results have been made use of in this work.

An alternative to radiotherapy with photons is the use of particle beams such as protons and heavier ions. These techniques can offer an improved confinement of the dose to the target volume, resulting in lower doses in the healthy tissue compared to photon beams [7]. A part of the motivation for this work has been to gain knowledge of radiotherapy using particles in contrast to photons. The project have involved visits at the heavy ion research facility, Gesellschaft für Schwerionenforschung (GSI), Darmstadt, Germany and the Heidelberg Ion Therapy (HIT), Heidelberg, Germany. GSI has ten years of experience with radiotherapy using carbon ions.

In **Chapter 2** of this thesis, the basics of radiation physics and relevant terminology in this work are presented. Interactions of charged particles, photons and neutrons with matter will be described. In addition, definitions within radiation dosimetry, such as dose and the biological effects of radiation, are included.

Chapter 3 describes concepts in radiotherapy including details on the photon generating linac and the deposition of the radiation dose. Due to the importance of particle therapy as a motivation for this master thesis project, the last part of this chapter concerns particle therapy. Further, in **Chapter 4**, aspects of the neutron production during radiotherapy with photons are explained.

Chapter 5 starts with general considerations within neutron detection, and finishes with a description of the detector types used in this work. In **Chapter 6**, the experimental set-ups and measurement procedures at HUS and IFE are specified, followed by a presentation of the experimental results in **Chapter 7**. The results have been divided into i) investigations of detector performance, ii) calibration issues and iii) application in radiotherapy. Finally, the conclusion of the results obtained and an outlook on further work is presented in **Chapter 8**.

Chapter 2

Radiation Interactions and Dosimetry

In this chapter the basic interaction mechanisms of photons, charged particles and neutrons with matter are presented. An introduction to dosimetry and biological effects is also given.

2.1 Interactions of Photons With Matter

Photons penetrating matter interact through several processes depending on the photon energy and the matter being traversed. The interactions with matter will result in the photon either being fully absorbed, or a change of the direction and energy of the photon by scattering processes. The principal mechanisms of photon energy deposition in matter are i) the photoelectric effect, ii) Compton scattering and iii) pair production. The result of the primary interactions above is either a total or a partly transfer of photon energy into electron energy. The possible reaction products are; electrons (and positrons), scattered photons and excited atoms. A fourth interaction mechanism, the photonuclear reaction, is important in certain radiation environments, e.g. in the surrounding of a medical linac. The photonuclear processes are possible at energies above several MeVs, resulting in neutrons, protons or heavier nuclear fragments being released from nuclei. Less significant interaction mechanisms are Thompson and Rayleigh (coherent) scattering.

The total photon cross section, σ_{tot}, of the photon interactions in lead is shown in Figure 2.1, and σ_{tot} is the sum of all the individual cross sections for the various processes.

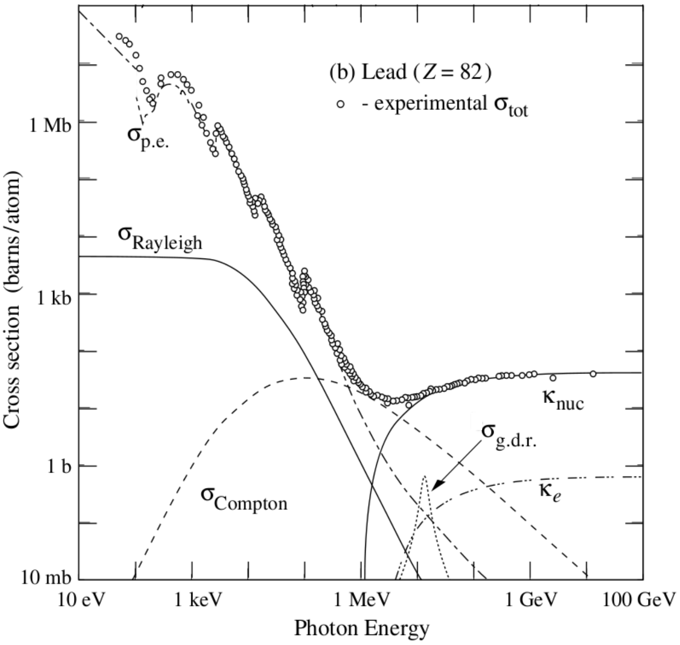

Figure 2.1: Total photon cross section, σ_{tot}, as a function of energy in lead (Pb), showing the contributions of different processes: $\sigma_{p.e.}$ = The photoelectric effect, $\sigma_{Compton}$ = Compton scattering, κ_{nuc} = Pair production, nuclear field, κ_e = Pair production, electron field, $\sigma_{Rayleigh}$ = Rayleigh (coherent) scattering, $\sigma_{g.d.r.}$ = The Giant Dipole Resonance (GDR) of the photonuclear interactions [8].

2.1.1 The Photoelectric Effect

In the process of the photoelectric effect, illustrated in Figure 2.2.a, the incoming photon has an energy on the order of the binding energy of an atomic electron. The photon collides with the electron and will transfer all of its energy to the electron, resulting in the photon being totally absorbed. Subsequent, the electron is emitted as a photoelectron with the energy $E_e = h\nu - E_b$, where $h\nu$ is the photon energy and E_b is the binding energy of the electron in its shell. The atom of the absorber is now left in an ionized state with a vacancy in one of its shells. This vacancy is rapidly filled by electrons of other shells or from the absorber, and the emission of characteristic photons follows.

The photoelectric absorption cross section, $\sigma_{p.e.}$, depends on Z of the absorber and the photon energy. The proportionality of $\sigma_{p.e.}$, is approximately expressed as $Z^5/E_{\gamma}^{3.5}$, and as a consequence the photoelectric effect becomes increasingly important in high-Z materials.

2.1.2 Compton Scattering

The process of Compton scattering is illustrated in Figure 2.2.b. An incoming photon with energy, $h\nu$, is scattered off an electron of the absorber. The result is a recoil electron, which will be absorbed by the material within a few centimetres, and a photon escaping at an angle, θ, from its incident direction, with a reduced energy $h\nu'$. The kinematics of the scattered photon is expressed as

$$h\nu' = \frac{h\nu}{1 + \gamma(1 - cos\,\theta)}. \tag{2.1}$$

Conditioned by the scattering angle, energy transferred to the recoil electron varies continuously from almost zero as $\theta \rightarrow 0$, to a large fraction near the Compton edge as $\theta \rightarrow \pi$. The more energetic photons, the higher is the probability of the photon and the electron being forward directed [9]. The Compton scattering cross section, $\sigma_{Compton}$, depends on the electron density in the absorber and increases linearly with Z.

2.1.3 Pair Production

Pair production occurs as a photon is transformed into an electron-positron pair in the vicinity of a nucleus as illustrated in Figure 2.2.c. Pair production becomes energetically possible at photon energies of more than twice the electron rest mass ($2m_e = 1.022$ MeV), and becomes dominant as the energy increases further. The cross section, κ, is approximately proportional to Z^2 in a media of low atomic number, and the proportionality decreases in denser materials due to atomic screening.

Electromagnetic Showers

Energetic electrons and positrons can emit Bremsstrahlung photons as they penetrate matter. Bremsstrahlung is emitted as charged particles decelerate in the Coulomb field of a nucleus [10]. At sufficiently high energies, photon interactions result in a electromagnetic shower. This is the combined effect of pair production and Bremsstrahlung emission, and the result is a cascade known as electron-photon (electromagnetic) showers.

2.1.4 Photonuclear Interactions

Photons with energies on the order of several MeVs can undergo nuclear reactions leading to the ejection of one or more nucleons. These processes are possible if the photon energy is greater than the binding energy of a given neutron or proton within the nucleus. The nucleon is emitted with energy $E_n = h\nu - E_b$, where $h\nu$ is the energy of the incoming photon and E_b is the binding energy of the nucleon.

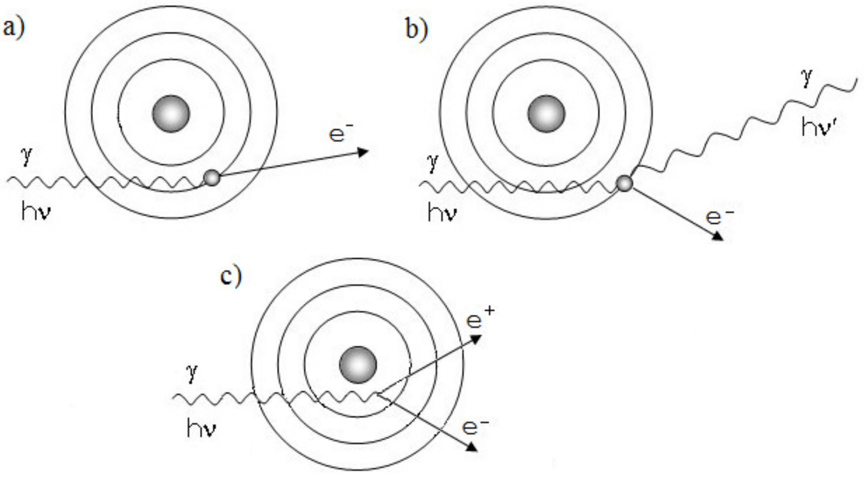

Figure 2.2: Photons interacting with the electrons of a material. a) The photoelectric effect. b) Compton scattering. c) Pair production.

The probability of photonuclear reactions is several orders of magnitude lower than the combined probability of the three primary photon interactions. The photonuclear processes are nevertheless important, due to the possibility of neutrons and radioactive nuclei being produced.

The photonuclear cross section, $\sigma_{g.d.r.}$, can be seen as a small peak just above 10 MeV in Figure 2.1. This is referred to as the Giant Dipole Resonance (GDR), and its properties have influence on the photoneutron production. The area under this peak is known as the strength of the GDR, and is found to approximately equal the dipole sum rule:

$$\int_0^\infty \sigma_{g.d.r}(E)dE = \frac{2\pi^2 e^2 \hbar}{Mc}\frac{NZ}{A} = 0.06\frac{NZ}{A}. \tag{2.2}$$

Here e is the electron charge, $\hbar$ is the Planck constant divided by 2π, M is the nucleon mass, c is the velocity of light, N is the neutron number, Z is the proton number, and $A = N + Z$ is the mass number of the nuclide. The unit of the GDR strength is MeV barns. For the light nuclei having mass numbers of less than 40, the GDR is located between 20 and 25 MeV as can be seen in Figure 2.3. At increasing mass numbers the mean energy of the GDR decays and falls below 15 MeV around mass numbers of 150. The width of the GDR vary by a factor of approximately two, depending on the shell structure of the respective element. The narrowest resonances are for those nuclei with closed shells, whereas the broadest are for the highly deformed nuclei [11].

To escape from the nucleus, a proton has to overcome both the nuclear and the Coulomb potential, whilst the electrically neutral neutron is only required to penetrate the nuclear potential. This feature affects the proba-

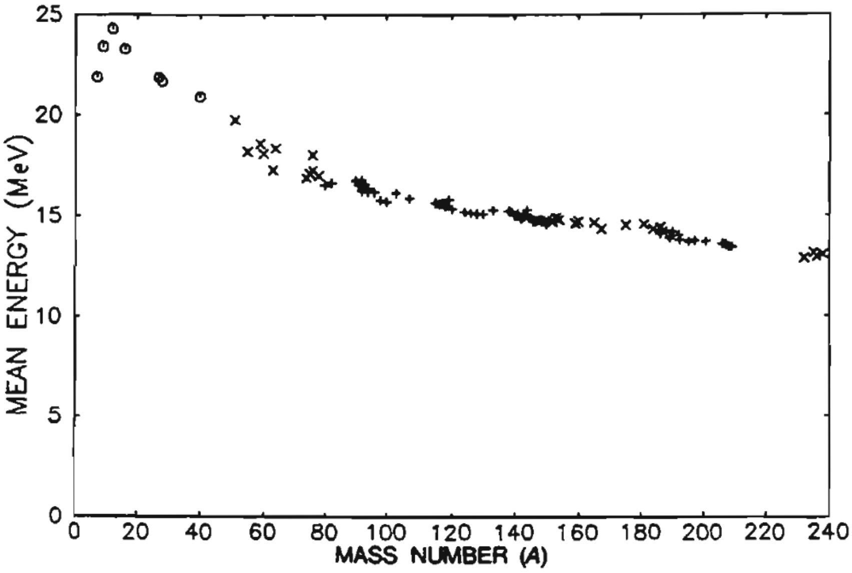

Figure 2.3: Mean giant resonance energies as a function of mass number A, as presented in NCRP report 79 [11]. The different markers are used to distinguish different data origin.

bilities of (γ, n) and (γ, p) reactions. In the lightest elements, the Coulomb barrier is located below the energy of the GDR, and the two reactions have nearly equal probability. However, in the heavy elements, the Coulomb barrier can be located far above the mean energy of the GDR, making the (γ, n) reaction predominant at energies above the Coulomb barrier [12]. The photoneutron production within the GDR can be explained by the two following mechanisms: Evaporation and direct knock-out [13]:

Evaporation

The mechanism of evaporation is the emittance of a neutron as the ground state is reached in a decaying nucleus. As an incoming photon is absorbed by a nucleus as a whole, the nucleus is left in an excited state followed by the emittance of one or several neutrons. The angular distribution of the outgoing neutrons is in this case isotropic.

Direct knock-out

The direct mechanism contributes if the incoming photons are sufficiently energetic to directly interact with a neutron, and thereby kick the neutron out of the nucleus. The angular distribution of the outgoing neutrons is forward peaked: $\sim a + b\, sin^2\theta$, where a and b are semi empirical parameters with angle θ between the flight direction of the incident photon and the emitted neutron.

2.1.5 Attenuation of Photons

The attenuation of photons is governed statistically by the probability of the photon to be absorbed or scattered per unit travelled distance. This probability is given by the linear attenuation coefficient, and it is the sum of the individual contributions from the interactions that may remove the photons from the initial flight direction. The linear attenuation coefficient, μ, is given by the product of the total photon cross section, σ_{tot}, and the number of atoms, N, in a volume:

$$\mu = N\sigma_{tot}. \tag{2.3}$$

The unit is cm^2g^{-1}, and equals the inverse of the average distance the photons travel in matter between interactions; the mean free path. The attenuation of photons has an exponential decrease. After penetrating an absorber of thickness, x, the remaining photon intensity, $I(x)$, is given by:

$$I(x) = I_0 e^{-\mu x}. \tag{2.4}$$

of where I_0 is the initial intensity of the photons as they enter the absorber.

2.2 Interactions of Charged Particles With Matter

Charged particles traversing matter interacts differently depending on the type of particle, the matter being traversed and the energy of the particle. The heavy, charged particles, that being charged particles other than the electron and the positron, will here be the main focus.

2.2.1 Heavy, Charged Particles

For heavy, charged particles at velocities on the order of several MeV, the energy loss is dominated by excitation and ionization of the atoms in a material [12]. As the projectile is heavy compared to the electrons of the material, only a small fraction of the energy is passed on in each collision. The heavy, charged particle will loose its energy continuously in tens of thousands of collisions, and the matter will be traversed in almost a straight line.

Occasionally, the charged particle will interact with a nucleus of the target material. The interaction can lead to the projectile being deflected (elastic scattering), or a nuclear fragmentation can occur (inelastic scattering). The resulting secondary fragments can be neutrons, protons or other heavier particles, depending on the energy of the projectile and material traversed.

2.2.2 Stopping Power and LET

The stopping power is the quantity expressing the energy loss for a charged particle traversing a medium. The stopping power is defined as the average linear energy loss, dE, as a distance, dx, of a medium traversed. Its functional dependencies are described by the Bethe Bloch formula below, and varies with the type of charged particle, its energy and the medium traversed. A common notation is $-dE/dx$ in units of MeV/cm.

The Bethe Bloch Formula for Stopping Power

Inelastic collisions between a heavy, charged particle and the electrons of an absorber, occurs with a certain probability [14]. For each macroscopic path length the collisions happen in great numbers and thereby the total energy fluctuations are kept minimal. Equation 2.5 is the Bethe-Bloch formula and gives the mean energy loss of charged particles per unit path length of an absorber material. The Bethe-Bloch is generally valid for different types of heavy charged particles with energies ranging from a few MeV up to the GeV region [8]. The energy loss is proportional to z^2M/E, given that $E \ll mc^2$.

$$-\frac{dE}{dx} = 2\pi N_a r_e^2 m_e c^2 \rho \frac{Z}{A}\frac{z^2}{\beta^2}\left[ln\frac{2m_e\gamma^2v^2W_{max}}{I^2} - 2\beta^2 - \delta - 2\frac{C}{N}\right] \tag{2.5}$$

with

Symbol	**Definition**
r_e	Classical electron radius = $2.818fm$
m_e	Electron rest mass = $0.511MeV/c^2$
N_a	Avogadro's number = $6.022 \times 10^{23}/mol$
I	Mean excitation energy (eV)
Z	Atomic number of absorber
A	Atomic weight of absorber (g/mol)
ρ	Density of absorber
z	Charge of incident particle in units of e
β	= v/c of incident particle
γ	$= 1/\sqrt{1-\beta^2}$
W_{max}	Maximum energy transfer in a single collision
δ	Density correction
C	Shell correction

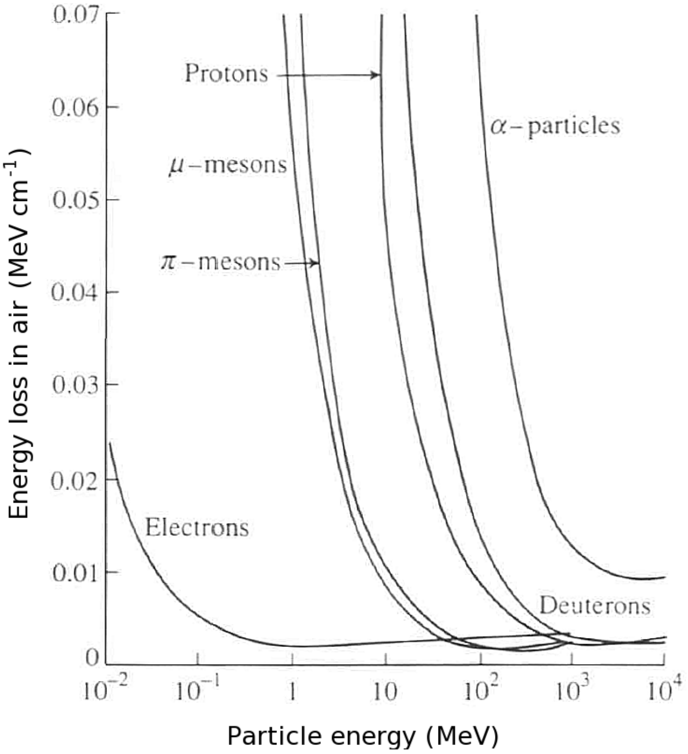

Figure 2.4: Stopping power of different charged particles in air as a function of the particle energy [15].

The energy loss of different charged particles over a wide energy range is shown in Figure 2.4. As can be seen from the curve, the stopping power increases strongly towards lower particle energies. At higher energies, a broad minimum is prominent, reaching from the MeV range to several hundreds MeVs of where relativistic energies are approached.

Linear Energy Transfer

Linear energy transfer, LET, is similar to the stopping power, but is not quite the same quantity. When a particle liberates a considerable portion of its energy at a distance from the particle track, the quantities are different: The stopping power includes the energy deposited both near and far away from the particle track of where the primary interactions occur. In the LET value, the locally imparted energy deposition is included exclusively [9]. For uncharged primary radiation, like photons, LET refers to the energy imparted in the local medium by the secondary charged particles produced.

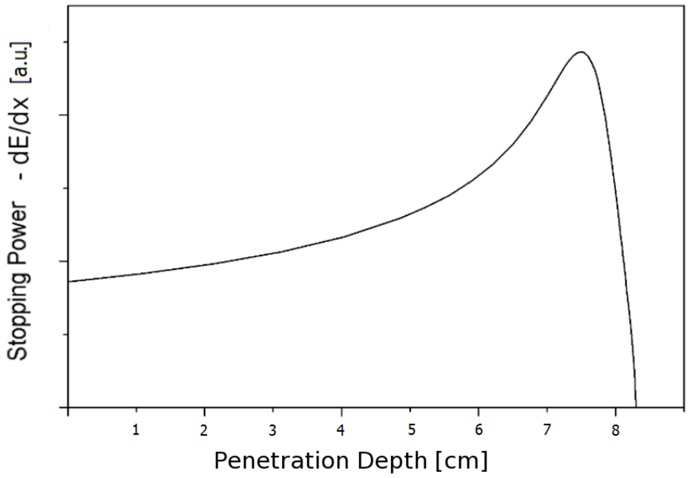

Figure 2.5: Schematic Bragg curve. Stopping power of a heavy charged particle in arbitrary units as function of penetration depth. Towards the end of its track is the characteristic Bragg peak.

2.2.3 Range and Bragg Curve

After having lost its energy continuously in a material, a charged particle will come to a stop at the end of its track, referred to as the range of the particle. For identical monoenergetic heavy charged particles of a few MeV or more, the ranges only vary by a few percent or less. This leads to a beam of monoenergetic heavy charged particles having a well defined range, with only a minor statistical variation of the path lengths, called range straggling [14].

As the charged particle is substantially slowed down close to its range in a material, the interaction rate and probability of high energy transfer in each collision increase. The charged particle is now given more time to interact with the surrounding matter, and the binding energy of the electrons will have more impact. The result of the increased energy loss is a maximum energy deposition towards the end of the path. The Bragg curve illustrates the increase in energy deposition by a charged particle as it traverses matter (Figure 2.5). The peak of where a charged particle reaches a maximum in energy loss is referred to as the Bragg peak. After the Bragg peak, energy loss falls off sharply as the particle charge is reduced by picking up electrons from the material.

2.2.4 Electrons and Positrons

As any charged particle reaches sufficiently high energies, energy loss by Bremsstrahlung becomes an important interaction mechanism, and this will totally dominate at relativistic energies. For heavy charged particles, Bremsstrahlung will not be of significance until energies of several hundred MeVs are reached. However, the lighter charged particles like electrons and positrons becomes relativistic at much lower energies than the heavy charged particles. The stopping power for electrons and positrons consists of two terms: a radiative term, $(\frac{dE}{dx})_{rad}$ representing the emittance of Bremsstrahlung, and a collision term, $(\frac{dE}{dx})_{coll}$. The latter term is a modified version of Equation 2.5, taking into account the low mass of the projectile, and the effects of indistinguishable particles for the case of the electron. The total energy loss of the electrons and positrons is therefore:

$$\left(\frac{dE}{dx}\right)_{tot} = \left(\frac{dE}{dx}\right)_{rad} + \left(\frac{dE}{dx}\right)_{coll}. \tag{2.6}$$

The track characteristics of the electrons and positrons differs from that of the heavy charged particles. For a light charged projectile, the target electrons are of comparable masses, and each single energy transfer is more significant. The light charged particle thus experiences relatively large energy losses and deflections in each collision, which lead them to have a tortuous path through an absorber.

Bremsstrahlung Spectrum

The radiative term of the energy loss is not only increasing as an effect of increasing energies, but also as an effect of the density of an absorber. The Bremsstrahlung photons are strongly dependent on the strength of the Coulomb field, or screening, that the incident electron experiences in dense materials. As the electrons decelerate through the Coulomb field in the vicinity of a nucleus, photons of a broad energy spectrum are emitted up to the kinetic energy of the incident electron. The most energetic photons are peaking in the forward direction, whilst the less energetic photons can emerge from a (thin) target having an angle with respect to the direction of the incident electrons. The average energy of the photons of the Bremsstrahlung spectrum is roughly 1/3 of the maximum energy.

2.3 Interactions of Neutrons With Matter

The neutrons exist in stable form only within the nucleus of a stable element. The mass of the neutron is 940 MeV/c, just above the mass of a its fellow nucleon; the proton. A free neutron is unstable and will decay into a proton with a mean lifetime of just under 15 minutes. As described in the previous sections, neutrons can eventuate both from photonuclear interactions and from nuclear fragmentation processes as a result of charged particles. In general, a nucleus can decay by neutron emission if it is created with an

Table 2.1: Neutron characterization by kinetic energy according to Turner [12].

Neutron characterisation	**Kinetic energy, *T***
Thermal	T $\approx$ 0.025 eV
Slow	T $\lesssim$ 0.5 eV
Intermediate	0.5 eV $\lesssim$ T $\lesssim$ 0.1 Mev
Fast	T $\gtrsim$ 0.1 MeV

excitation energy above that of the neutron binding energy. The potential sources of residual radioactivity are any places where neutrons are produced or absorbed, leading to neutrons often being served special attention from a radiation protection perspective.

2.3.1 Neutron Energy

The interactions of the neutrons with matter are strongly energy restricted and will also depend on the characteristics of the material traversed. The kinetic energy can be used in dividing the neutrons into categories. Thermal neutrons refer to the neutrons having kinetic energies of 1/40 eV. This is the most probable energy in the energy distribution of neutrons in thermal equilibrium with the environment at typical room temperatures. Next follows slow, intermediate, and fast neutron energies as listed in Table 2.1. At approximately 0.5 eV, is a border line called the cadmium cut-off energy. Above this energy an abrupt drop in the absorption cross section in cadmium is observed, and this property can be utilized in separating slow neutrons from those of higher energies during neutron detection.

2.3.2 Interaction Mechanisms

The neutron lacks electromagnetic charge and consequently do not interact via the Coulomb force. Its principal interaction is through the short ranged strong force, which requires the neutron to come very close to the nuclei before being able to interact. In normal dense matter, nuclei are separated by great distances and the neutron is therefore a very penetrating particle. The total neutron cross section, σ_t, expresses the total probability of all the various types of neutron interactions listed in Figure 2.6. The interaction mechanisms of neutrons with matter can be divided into scattering and absorption. If a neutron is scattered off a nucleus, the energy and direction can be considerably changed. If it is absorbed, the neutron is captured by the nuclei and replaced by radiation in form of secondary particles, e.g. photons, charged particles, additional neutrons or fission fragments. A fast neutron will mainly loose its energy by a series of elastic scattering events as it traverses through matter, a process known as neutron moderation. Recoiling

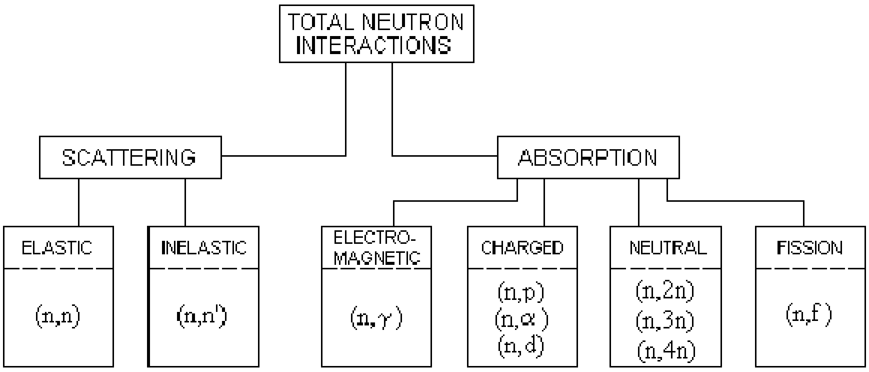

Figure 2.6: Categories of neutron interactions given as incoming and outgoing particles. Each type of interaction has its energy dependent interaction cross section [16].

nuclei of the material penetrated, assures fulfilment of energy conservation as the neutron gradually slows down. As the neutron energy decreases, the interaction modes of absorption becomes increasingly prominent. If the neutron reaches thermal energies, it will scatter inelastically about until absorbed by a nucleus of the material.

2.3.3 Neutron Attenuation and Mean Free Path

As the case with photons, the neutron is also attenuated in a material it traverses. To describe the attenuation of neutrons, the macroscopic cross section, Σ, is often used in analogy with the attenuation coefficient of photons. The macroscopic cross section can thereby be expressed as $\Sigma = N\sigma_t$, where N is the number of nuclei per volume of a material. However, when comparing with photon interactions, the concept of the macroscopic neutron cross section is more complicated due to the importance of neutron scattering processes. The neutron cross section, σ_t, is strongly energy dependent. The attenuation of neutrons, will therefore vary widely as a function of the neutron energy [17]. The neutron mean free path, λ_n, in analogy with photons, equal $1/\Sigma$. In solid materials, λ_n may be in the range of a centimetre or less for slow neutrons. While the case for fast neutrons, λ_n can reach tens of centimetres [16].

2.4 Dosimetry and Biological Effect of Radiation

Radiation dosimetry is the quantification of the biological impact that follows from the exposure to radiation. The dosimetry entities presented here are the sets defined in the 1990 Recommendations of the International Commission on Radiological Protection (ICRP) [18] and in 1993 International Commission of Radiation Units and Measurements (ICRU) [19].

2.4.1 Absorbed Dose

The absorbed dose, D, further on referred to as dose, is a fundamental dosimetic quantity and is the amount of energy, dE, deposited per unit of mass, dm, in a medium:

$$D = \frac{dE}{dm}. \tag{2.7}$$

Its unit is Gray (Gy), which in SI-units is Joule/kg.

2.4.2 Biological Effects of Ionizing Radiation

On a microscopic scale, ionizing radiation changes the atoms in living tissue and as a consequence the molecules that the atoms are a part of. In molecules that are part of a living cell, the chemical bonds can be damaged by ionizing radiation. If the DNA structure of a cell is affected by ionizing radiation, the survival or the reproduction of the cell is at risk. Assuming that a sufficient amount of cells in an organ is damaged, loss of organ function occurs. This predictable effect of high dose radiation is defined as a deterministic effect [18]. In cases of low dose exposures where only partial damage is imposed, the cell can repair itself. The result may be a healthy repaired cell, or the result can be a modification that can increase the risk of cancer in the individual or in its descendants through the genetic material. These somatic and heredity effects are known as stochastic effects.

Relative Biological Effectiveness (RBE)

Different types of radiation have different capabilities in producing effects in biological systems. The pattern of energy deposition in a biological system, is a characteristic of the specific radiation quality involved. The energy deposition by radiation in biological materials depends on the rate of ionization along the radiation tracks; - the ionization density. A dense energy deposition along the tracks results in a high LET, whereas a more sparse ionization track results in a lower LET. Photon radiation have a relatively low ionization density, while neutrons, protons or heavier nuclei have a denser energy deposition. These differences in energy deposition results in that neutrons, protons and heavier nuclei produce more severe biological effects per unit of absorbed radiation dose, than what the effects of photons produce. To quantify these variations, the biological impact of different types of radiation are contrasted in terms of their Relative Biological Effectiveness, RBE. The RBE values are based on experimental studies of the biological impact of a

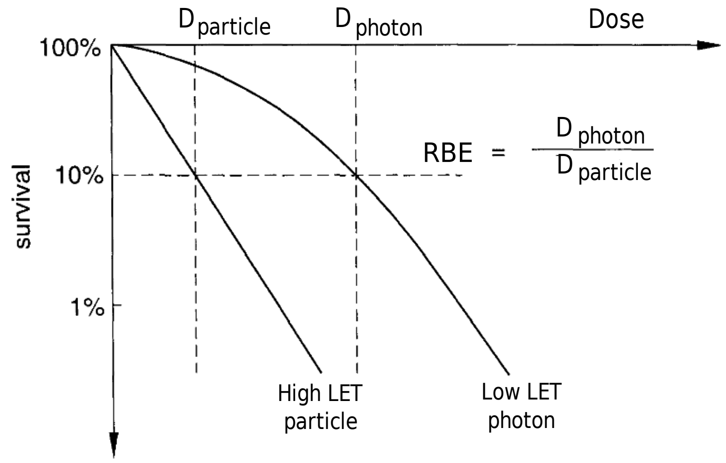

Figure 2.7: Dose versus cell survival curves for particles and photons [21]. Relative biological effectiveness, RBE, is the dose required for inactivation of 90% of the irradiated cells in same biological material.

given radiation type in contrast to the impact of a test dose of a reference radiation, usually photon radiation.

Other factors that contribute to differences in RBE comprise the energy of the radiation applied, the total dose received, the temporal pattern in which the dose was deposited and the repair capacity of the of the biological tissue irradiated [20]. According to cell survival curves for particles and photons (Figure 2.7), RBE is defined as the dose rate required for inactivation of 90% of the irradiated cells in the same biological material. The high LET radiation is more biological efficient than the low LET as illustrated. The RBE is a highly useful quantity in describing the relative efficiency of dose depositions in radiotherapy.

2.4.3 Equivalent and Effective Dose

For radiation protection purposes, the quantities equivalent dose and effective dose are commonly used. These entities relate biological effects to the type of radiation applied and the tissue in which the radiaiton deposites dose. Typical area of application is those involving low dose levels as in the recommendations of dose limits.

Table 2.2: Radiation Weighting Factors from ICRP [18].

Radiation type and energy	**Radiation weighting factor, w_R**
Photons, all energies	1
Electrons, muons, all energies	1
Neutrons	
< 10 keV	5
10 keV to 100 keV	10
> 100 keV to 2 MeV	20
> 2 MeV to 20 MeV	10
> 20 MeV	5
Protons > 2 MeV	5
Alpha particles, fission fragments, heavy nuclei	20

Equivalent Dose

The radiation weighting factor, w_r can be used as a simplified measure of the RBE. The equivalent dose, H_T, is the radiation weighted dose:

$$H_T = \sum_R w_R D_{T,R} \tag{2.8}$$

where, $D_{T,R}$, is the average physical dose received by a specific organ or tissue, T, delivered by a radiation of quality, R. Values of w_r are listed in Table 2.2. The unit is Sievert (Sv) which have the same SI unit as Gy. The Sv is normalized such that 1 Sv of any radiation will have the same effect as 1 Gy of photon radiation.

Effective dose

To account for the different radiation sensitivities in various organs, the unit effective dose is used. The individual organ dose values are multiplied by the normalized tissue weighting factor, w_T. The effective dose, E, is the tissue weighted measure of the stochastic risks in relation to a uniform irradiation of the whole body.

$$E = \sum_T w_T H_T, \tag{2.9}$$

where H_T is the equivalent dose in the tissue or organ, T. The unit is Sv.

2.4.4 Quality Factor and Dose Equivalent

The quality factor, Q, also is intended to relate the biological effectiveness of a radiation to the absorbed dose in tissue. The quality factor is similar to

Table 2.3: Quality factors, Q, for different energies. [18]

LET, in water (keV/μm)	**Q**
<10	1
10-100	0.32xLET - 2.2
>100	$300/\sqrt{LET}$

RBE, but the Q is defined directly as a function of the LET. The related unit of dose equivalent, H, is defined as the amount of any type of radiation, that when absorbed in a biological system, results in the same biological effect as one unit of absorbed dose delivered in the form of low LET radiation [9]. For the low LET photon, Q is unity in analogy to the RBE definition. The dose equivalent is expressed as:

$$H = DQ, \tag{2.10}$$

where D is the absorbed dose. The units are also in Sv.

Table 2.3 shows how the quality factor increases with LET. For electrons and photons Q is unity and is approximately 20 for protons [9].

2.4.5 Fluence-to-Dose Conversion

Fluence is generally defined as $\Phi = dN/da$ where dN is the differential number of photons or neutrons incident on a sphere (detector) with differential cross sectional area da [9]. For conversion to dose, energy ambient conversion factors, h_E, in units of $Sv\,cm^2$ is multiplied with the fluence to obtain the dose equivalent. Neutron fluence-to-dose conversion factors are listed in Appendix C.

2.4.6 Dose Response Relationship

The biological effects of ionizing radiation on the human body can be quantitatively described in terms of dose-response relationships, that is, the incidence or severity of a given effect, expressed as a function of dose [12]. Response to radiation depends on age, gender and cell type, as well as the amount of dose deposited. Although the potential cancer risk as a result of dose exposure is acknowledged [3], the functional relationship contains many uncertainties. The ICRP has defined acceptable dose limits as a guideline for annual dose exposure: Annual effective doses are not to exceed 1 mSv and 20 mSv for the general public and for the occupationally exposed personnel respectively, unless there is some justifying reason for surpassing this guideline. The limits are occasionally revised, and have been gradually reduced over the years. The general advice is to sustain the radiation exposure to humans as low as possible [18].

Chapter 3

Radiotherapy

Radiotherapy has been applied as cancer treatment for more than a hundred years, with its earliest roots traced back to Wilhelm Röntgen's discovery of X-rays in 1895. In the early 1900s, a growth in the field of radiation therapy came about thanks to the the work of Nobel Prize winning scientist Marie Curie, who opened a new era in medical research and treatment through the discovery of the radioactive elements polonium and radium. Since the late 1940s, linacs have been applied as radiation sources of photons, and is the most widespread modality within radiotherapy today.

In 1946, Robert R. Wilson suggested radiotherapy using charged particles in his publication 'Radiological Use of Fast Protons' [22]. The advantages of treating tumours with charged particle beams are acknowledged, and is an important part of radiotherapy of both today and will probably evolve in the future [23].

Cancer evolves when cell division occurs outside the control mechanisms of the human body. An accumulation of such cells is called a tumour, and tumours can be of malignant or benignant nature. In either case, the tumour, referred to as the target volume, can be treated with the use of external radiation therapy. The overall objective in radiotherapy is to inactivate all cancer cells, while at the same time spare healthy tissue around the tumour(s). In order to achieve this goal during radiotherapy, sharp dose gradients between the target volume and the healthy tissue will be of help wherever these can be applied in the field set-up during the planning stage.

3.1 Photon Therapy

The most common form of radiotherapy, as of 2010, utilizes linac produced photon beams with energies in the MeV range. In a medical linac, the therapeutic photon beam is generated by colliding accelerated electrons into a heavy metal target producing Bremsstrahlung photons. The emerging photon field is modified by a system of filters and collimators, arranged in

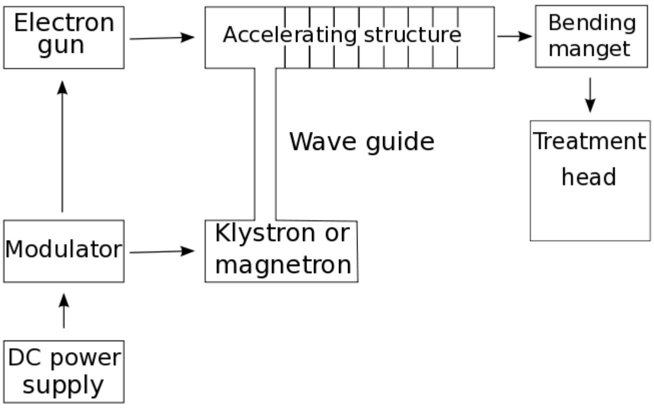

Figure 3.1: A block diagram of a medical linear accelerator [24].

such a way that the radiation is delivered to the target volume in the most beneficial way for the patient.

3.1.1 The Linear Accelerator and Photon Beam Production

The medical linacs use high frequency alternating voltage to accelerate the electrons up to energies in the MeV range. The block diagram in Figure 3.1, shows the major components of a medical linear accelerator [24]: A power supply provides a modulator with DC power. In the modulator, high voltage pulses in intervals of a few microseconds are produced. These pulses are further simultaneously delivered to the electron gun and the microwave-producing klystron or magnetron. From the klystron or magnetron, the pulsed microwaves are transported to the accelerating structure through a wave guide system. Electrons, produced by the electron gun, are injected into the accelerating structure synchronized with the arrival of the pulsed microwaves. The electrons enters the accelerating structure with an energy of about 50 keV, and are accelerated in bunches by the electromagnetic microwave field. Emerging from the accelerating structure is an electron beam, that is steered and focused an angle of 270° between the accelerating structure and the treatment head. The electron beam reaching the treatment head are now in place for modifications prior to final use as a treatment field.

Figure 3.2 illustrates the process of creating bremsstrahlung photons and the shaping of the radiation field in order to obtain a flat homogeneous treatment area. To produce the actual photons, the electrons arriving from the bending magnet are absorbed in a suitable target, such as gold plated tungsten. As the electrons decelerates in the target, they emit bremsstrahlung, thus emit deeply penetrating photons in a forward lobe [25]. Next, the pho-

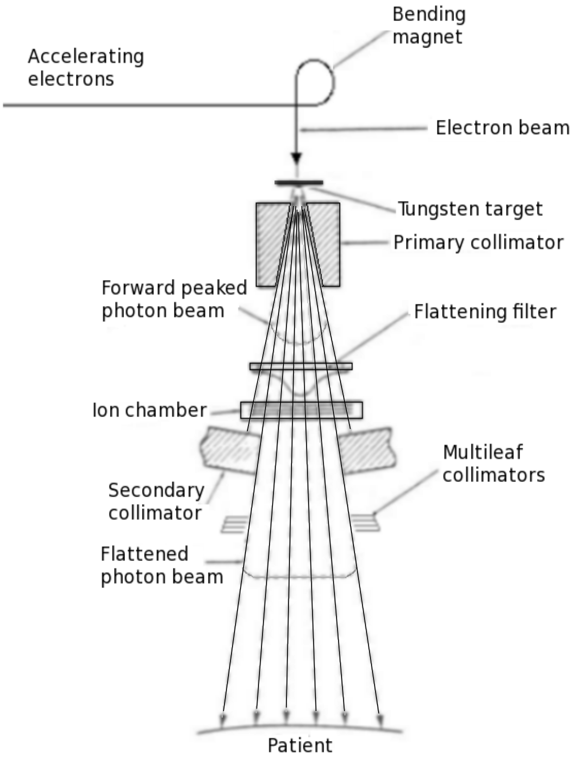

Figure 3.2: Production and shaping of a therapeutic photon field in the treatment head of a linac. See text for full description. [24] modified.

tons reach the primary collimators which absorbs all but the photons travelling in the required directions. Given the, energy dependent, directional distribution of bremsstrahlung photons, where the photons produced in the target have momentum mainly in the forward (0°) direction, the transversal beam intensisty has to be modified in order to create a flat "therapeutic" field of any given size. This modification of the transverse intensity distibution is done by inserting a so called flattening filter into the beamline subsequently after the target. This conically shaped flattening filter will dampen the beam in the central, forward direction. By finetuning the thickness and shape of the flattening filter in order for it to match the spatial distribution of photons, the linac designers obtain an optimally flat field for all available treatment field sizes.

The beam further proceeds through an ion chamber to enable monitoring of the beam. In order to modify the radiation field, the secondary collimators are applied. Final collimation of the beam is accomplished by the use of the MLCs. The MLCs are a set of collimator leaves that can narrow down the edge of the radiation field to fit any geometrically shaped area. The MLCs are also applied in a dynamic mode in one of today's most conformal photon treatment techniques, the IMRT. Some of these techniques are described in Section 3.1.6.

3.1.2 Photon Beam Energy

The pulsed photon beams produced by the linac, are in most cases of energies up to 6 or 15 MeV. Such beams are not monoenergetic, but they contain an energy spectrum reaching from zero to the maximum that corresponds to the energy of the electrons used for producing the photon beam. Photon beam energies, or beam qualities, are in radiation treatment linacs described by the depth dose curve that the given photon beam will produce in water. In order to distinguish the therapeutic photon energy from a monoenergetic beam, the photon beam energy is quantified in units of megavoltage, MV [25]. The photon beam settings of the linac will therefore further be given in units of MV.

3.1.3 Dose Deposition

As the effective atomic number in the human body ranges from approximately 5 to 14, this results in Compton scattering being the dominant interaction mechanism of photons in the therapeutic energy range. Compton electrons have a forward directed range limited to a few centimetres in tissue, and leads to an increase in the energy deposition in the first centimetres of the entrance channel of the beam (Figure 3.3). This is called the build-up region of where the dose deposition increases until a maximum, D_{max}, is achieved in the tissue. After the D_{max}, a slowly exponential decrease follows as greater depths are reached inside a patient. Higher photon energies reach greater depths in human tissue such that the position of D_{max} can be varied a few centimetres in depth from around 1.5 cm (6 MV) to 3 cm (15 MV). The target volume is almost always located at greater depths than the D_{max}, resulting in the healthy tissue in the entrance channel of the beam receiving a higher dose than the target volume. To enable a safe delivery of a sufficiently high dose to the target volume without placing a severe dose to the exterior layers of tissue at the same time, the beam is usually delivered through multiple entrance channels. In this way, a lower dose to the healthy tissue in the entrance channel is obtained by redistributing the dose over a greater volume.

3.1.4 Photon Beam Delivery

To enable delivery of a prescribed dose to the target volume from multiple beam angles, the general arrangement of the linac is such that the therapeutic photon beam can be oriented around the patient as can be seen in

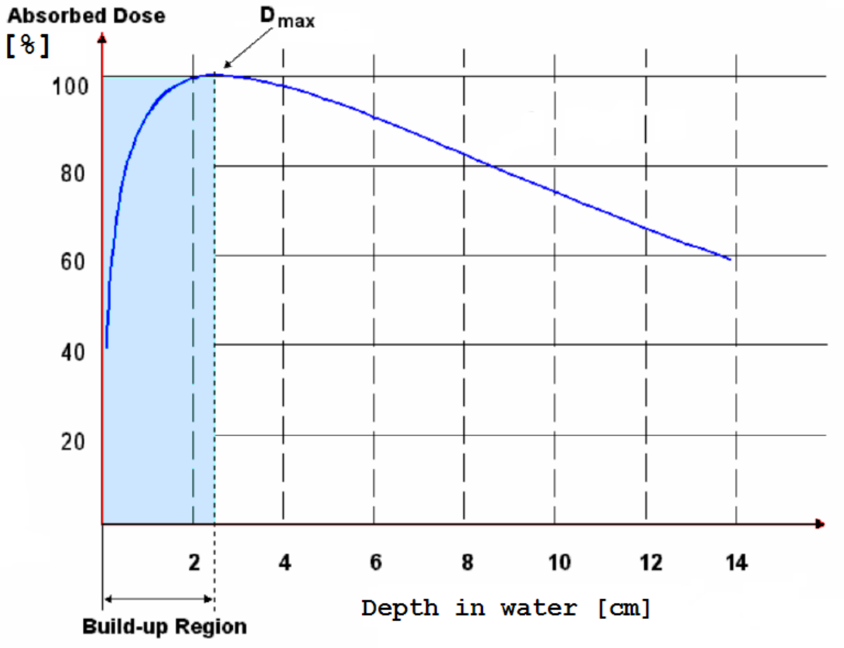

Figure 3.3: Photon depth-dose curve in water. The photon field entering the water or tissue, generates a dose build up in the first couple of centimetres of the medium traversed until reaching a maximum dose, D_{max}. A slowly exponential decrease follows as greater depths are reached [26].

Figure 3.4. The linacs are bolted with a stationary structure and a rotating machine head, or gantry, mounted to this. Inside the gantry the accelerating structure and all the components for producing and collimating the beam are located. The orientation of the patient table can be altered in the lateral, horizontal or longitudinal directions with respect to the gantry head. Linacs are oriented around a common center, the isocenter. The isocenter is the point around which i) the gantry head, ii) the collimators in the gantry head and iii) the patient table are rotated. This reference position is thus the point in space around which the central axis of beams from different gantry angles intersects. It is common to calibrate the dose output from the linear accelerator with respect to dose to the isocenter, which for linacs is located 1 m below the photon producing target in the gantry head. This point is the basis for the dose calculations, and the patients are ideally positioned with the isocenter in the target volume during treatments.

The radiation output of the linac is quantified in Monitor Units (MUs). The linacs at HUS are calibrated such that 130 MUs correspond to a dose of 1 Gy in the isocenter at 10 cm depth in water, applying a 10x10 cm^2 photon field. The output of the linac is measured by the ionization chambers in the beam line, positioned below the target. This output is applied when

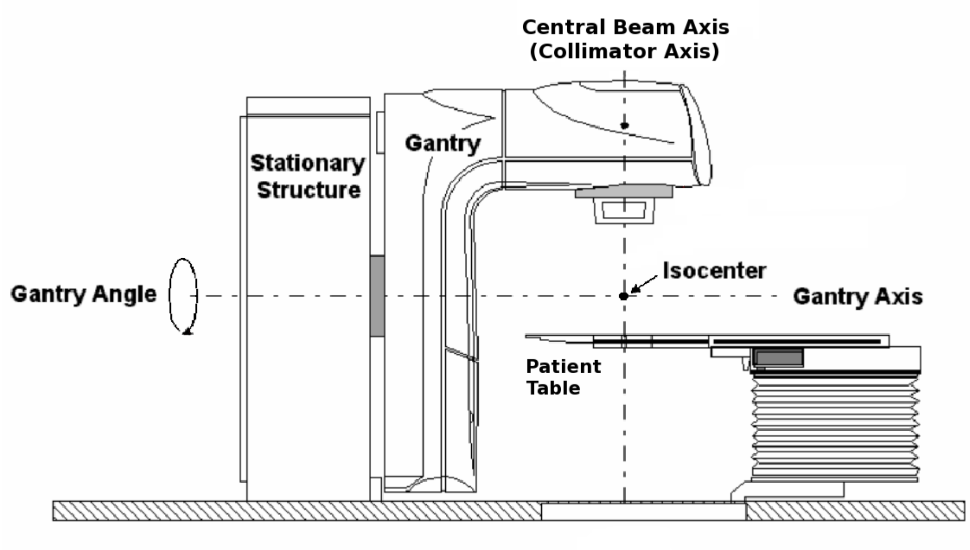

Figure 3.4: The linear accelerator is mounted on a gantry which allows the therapeutic beam to be rotated around the patient. The isocenter is the intersection point of the rotating central beam axis and the three axes of rotation; the gantry, the collimators and the patient table, located 1 m from the photon producing target [26].

adjusting the MU calibration in order to maintain the relation between the MUs of the machine, and the dose in Gy, measured by an external ionization chamber in the isocenter position. To deliver a dose to other depths and when using other field sizes, tables for conversion factors are applied. Increasing the photon field will increase the dose, and requires less MUs. Vice versa, with a decreasing photon field, more MUs are required in order to obtain the same dose at a point in the beam center.

3.1.5 Radiation Treatment Planning

To calculate dose distributions inside the patients (or a phantom patient), a treatment planning software is utilized. A 3D image of the anatomy of the patient is obtained using different imaging scanning techniques. Computed Tomography (CT), Magnetic Resonance (MR) and Positron Emission Tomography (PET), all provide different complementary information. During a CT scan, photons traverses through the patient, and the attenuation coefficients are obtained for the different organs or tissues in the patient. These CT images are imported into a dose plan system, generating a 3D volume of the relevant region of the patient. Each voxel, or volume pixel, in the image has assigned CT-numbers, related to the attenuation coefficients in the tissue imaged. The dose planning software can further be of assistance in designing the treatment in an optimal way within conditions described by the user. A typical treatment plan have a total dose of 30 to 70 Gy prescribed to the treatment volume, which is delivered in daily fractions of 1 to 2 Gy over a period of several weeks.

3.1.6 Radiation Treatment Techniques

An important objective in radiotherapy is often to make the dose fall rapidly at the edge of the treatment volume; i.e. steepen the field gradient. Treatment techniques using external photon beams are steadily evolving, aiming at sparing the surrounding healthy tissue without having to compromise on the dose to the target volume. Two advanced modalities are 3D-CRT and IMRT.

During 3D-CRT, the beam is delivered to the patient from multiple angle, typically from 4 to 6, while fixing the MLCs with the size and shape of the tumour volume as well as avoiding the surrounding organs and tissues. Because the radiation beams are very precisely directed, nearby normal tissue receives less radiation.

One of the most advanced treatment techniques used today; IMRT, is a specialized form of 3D-CRT that utilizes inverse dose planning. In this type of planning procedure, the dose distribution is calculated first, based on a set of criterias of dose to the target volume and the organs at risk, and thereafter the beam delivery is calculated based on the optimized dose distribution. IMRT dose plans can be delivered using dynamic treatment fields by moving the MLC leaves during the irradiation. Not only is the geometric beam conformed, but also the fluence across the beam is varied. With IMRT, the radiation dose will be delivered from several fields divided into many beamlets. The intensity of each beamlet can be individually adapted for the geometry of the tumour. IMRT makes it possible to further limit the amount of radiation received by the healthy tissue, in particularly near the target volume. In some situations, the sharp field gradients that can be accomplished in an IMRT treatment, safely allow a higher dose of radiation to be delivered to a tumour located near a sensitive organ.

3.2 Particle Therapy

Particle therapy is the application of charged particle beams in radiotherapy. Different particles have been tested in therapy during the last 70 years: protons, helium ions, pions and carbon ions are among them [27]. There are promising aspects in choosing particles over photons for radiotherapy. The application of protons and ions offers physical, and in the case of carbon ions, biological advantages compared to that of photon radiotherapy [28,29]. The energy deposition of carbon ions makes them suitable for treatments of deep seated and radio-resistant tumours. The dose deposition is low in the entrance channel of the beam, and increases towards the carbon ion's range. A characteristic feature of particle therapy, is the sharp dose gradients subsequently after the end of the particle track, resulting in a very low dose exit dose behind the target volume. Proton beams are the most common form of particle therapy applied today, exceeding 60 000 patients treated on world basis. Number of patients treated with carbon ions are just above 5000, in 2009.

One of the most important disadvantages of radiotherapy using charged particle beams is the high cost in obtaining a delivery system for this. To accelerate the particles to the required energies, synchrotrons and cyclotrons are utilized. From 1954 to 1990, the patients treated with particle therapy were treated using accelerators originally designed for nuclear physics research. In 1990, Loma Linda University Medical Center built the first proton therapy facility designed to treat patients with protons in a hospital setting. Today, there are several operating proton therapy facilities in hospitals, mainly located in Japan, USA and Europe. See Appendix G for a overview of particle therapy facilities in operation and at the planning stage. Carbon therapy are currently performed at three heavy ion facilities; two are located in Japan and one in Heidelberg, Germany [30]. The latter facility is the dedicated particle treatment clinic HIT, which opened November 2nd, 2009.

In the following, the main features of particle therapy and some of the technical aspects are described. The particle therapy facility HIT and its developments from research at GSI, will be served special attention.

3.2.1 Physical Aspects of Charged Particles

The energy deposition of charged particle beams, differs from the energy deposition of photons. As illustrated by the depth-dose curves in Figure 3.5.a, the dose deposition is lower in the entrance channel for particle beams in comparison to that of photon beams. Towards the end of the charged particle's track, the dose increases drastically into a peak; the so-called Bragg peak. After this peak, the dose falls off sharply, forming a low dose tail. The less lateral scattering of the particle beam results in a high precision of the dose delivered at the target volume [31]. In Figure 3.5.b, the lateral scattering of photons, protons and carbons are shown. As can be seen, carbon beams have less lateral scattering than photons and protons. This contributes to a lower dose deposition in the entrance channel of the carbon beam [32].

Determined by the initial energy, protons and ions have a well defined range in tissue compared to photons and electrons. Figure 3.6 shows the range energy dependence for protons; e.g would a proton beam of 150 MeV, reach about 14 cm into water before the Bragg peak reaches a maximum value. A carbon beam would require energies of 270 MeV/u, in order to reach

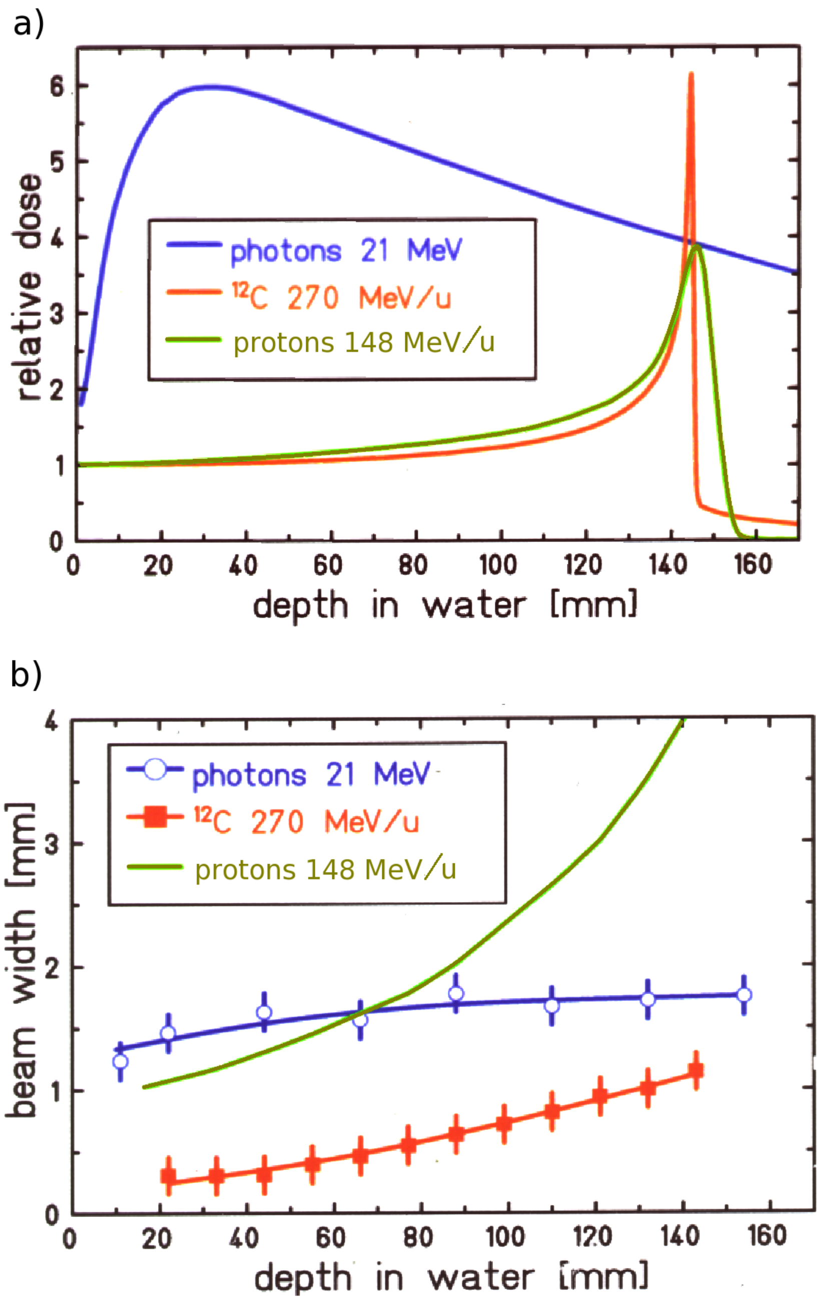

Figure 3.5: a) Depth-dose curves of photons, protons and carbon ions in water. b) Lateral beam profiles of photons, protons and carbon ions. The beam width is plotted as as function of the depth in water [33].

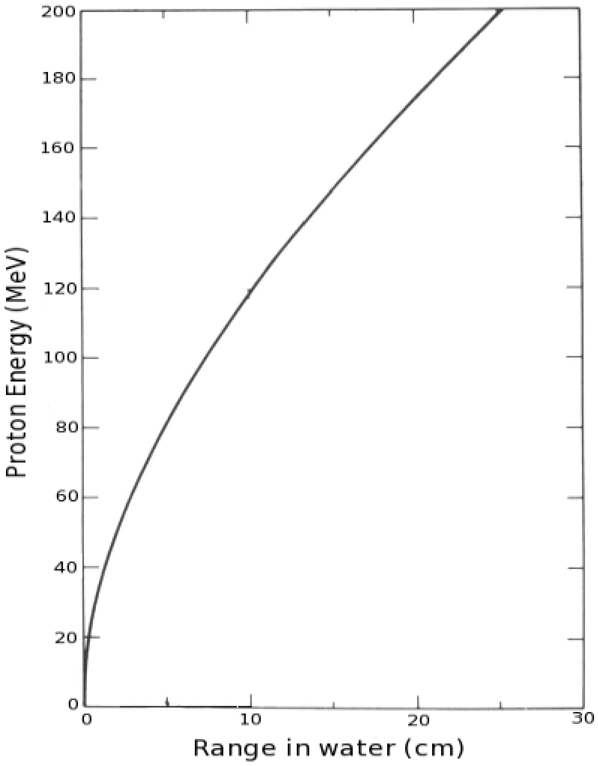

Figure 3.6: Range energy relationship for protons [24].

the same depth. By varying the energy of the beam, the depth position of the Bragg peak can be modulated. Utilizing a wide range of specific beam energies during a treatment, makes it possible to spread out the position of the Bragg peak such that a quite homogeneous treatment dose is delivered to the entire depth of a target volume. The sum of the overlapping Bragg peaks is known as the Spread Out Bragg Peak (SOBP).

3.2.2 Biological Aspects of Charged Particles

The rate of locally deposited energy from charged particle beams can be quantified as LET, as introduced in Section 2.2.2. The LET is a measure of the local ionization density along the particle track, and depends on the type of particle as well as the energy of the particle. Both protons and carbon ions have a higher LET compared to that of photons. As energy of the charged particle decreases towards the end of its range, the LET increases additionally in the case of the carbon ion. The result is that the carbon ions have an increased relative biological effectiveness (RBE) at the Bragg peak as shown in Figure 3.7. In clinical applications, the absorbed dose in the Bragg peak is multiplied by a RBE factor of 1.1 for protons, and can for

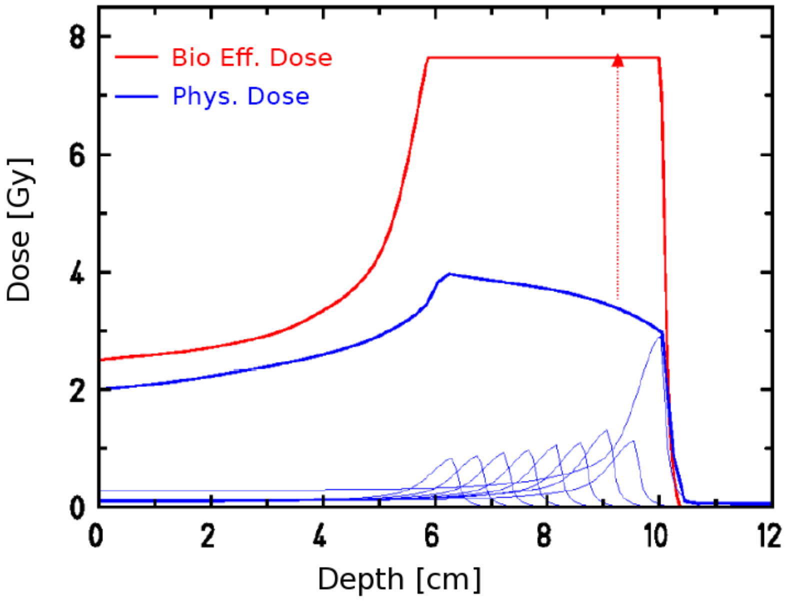

Figure 3.7: Depth dose curves shown with SOBPs, illustrating the physical advantages of protons and carbons (blue). Carbon ions have an elevated biological effectiveness in the Bragg peak (red) [34].

carbon ions be as high as 4 [7].

The combined physical and biological advantages make radiotherapy with carbon ions well suited for treatment of deep-seated tumours, also for target volumes located near critical organs. In some cases involving radio-resistant tumours that require particularly high doses, a sufficiently high treatment dose can be delivered without compromising the surrounding healthy tissues or organs. This can in some cases not be accomplished using other conventional treatment techniques available today.

Dose Deposition On A Microscopic Level

From studying the track structure of high LET carbon ions and the more sparsely ionizing photons on a micrometer scale, the elevated RBE can be explained. In Figure 3.8, the dose distributions in the frame of a cell is displayed. Photons distribute the dose homogeneously across the cell. For the high LET carbon ions, a large fraction of the cell is not hit, and the dose is concentrated in a few sharp spikes of heavy impact [35]. This latter way of depositing the dose is proven more efficient in breaking both strands of the DNA helix of a cell. A double strand break is the most severe DNA damage that can be implemented, and the cell repair system is likely to fail at attempts of rebuilding the cell. This makes the DNA structures the

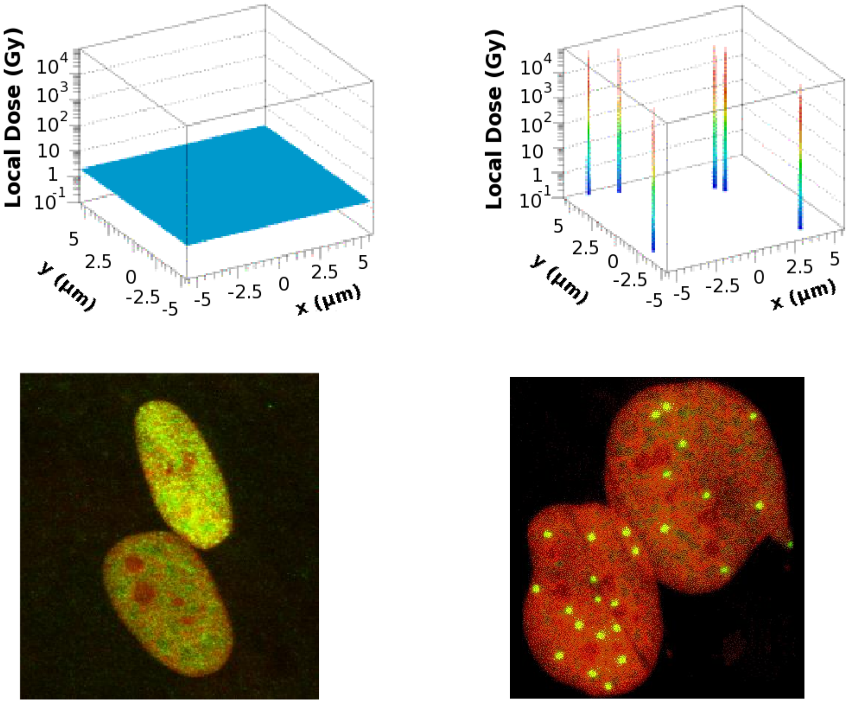

Photons **1 MeV/u carbon ions**

Figure 3.8: Comparison of the energy deposition of sparsely ionizing photons (left), and of high LET carbon ions (right) on the scale of the a cell. For photons, the dose is homogeneously distributed across the cell. For carbon ions, the dose is concentrated in a few sharp spikes. The distribution of damage to the cell nucleus is shown in the lower row. Experiments have shown areas of high local damage, as for carbons, is more effective in causing fatal damage (yellow) to the DNA [31].

principal target in inactivating a cancer cell [18], which in order is more effectively achieved by the a high local dose deposition as of a carbon ion.

3.2.3 Technical Solutions

In order to accelerate heavy, charged particles towards therapeutic energies of 200-300 MeV, cyclotrons or synchrotrons are utilized. A proton beam requires a cyclotron of 6-7 m diameter (or synchrotrons), while currently only synchrotrons of about 20 m diameter are suitable for reaching sufficiently high energies as needed for accelerating carbon ion beams. As the range of the particles depends on the beam energy, the energy has to be varied during the radiation treatment in order to cover the entire depth of the tumour volume. This depth modulation can be obtained in a passive or an active manner. Due to the cyclotrons capabilities of only producing fixed energies, the beam must be moderated physically by an appropriate moderator in front of the beam; thus passive moderation. As for synchrotrons, the extracted beam energy can easily be changed, and no absorbing material in front of the beam is demanded.

The lateral dose distribution of the beam can also be achieved by a passive or an active method. Passive spreading utilizes sophisticated scattering foils followed by sets of collimators in front of the beam to obtain depth modulation. The passive beam delivery techniques are the most common methods applied and have the advantage of simple treatment planning and technical solutions [36]. A disadvantage of the passive systems, is that the collimation in front of the beam is a source of secondary particles like protons, neutrons and nuclear fragments contributing to dose outside the treatment volume. To enable optimal conformity of the delivered dose, active techniques are preferable. The active technique can be attained by exploiting the electromagnetic charge of the particles. By applying magnetic fields, the charged particles can be deflected and thereby magnetically guided across the transverse treatment plane [31]. With the appliance of active scanning techniques, the dose deposited outside the treatment volume is limited to the unavoidable contribution in the entrance channel of the primary particle beam, and a smaller contribution from beam fragmentation [37]. The low dose tail right after the Bragg peak is due to this fragmentation of the primary beam.

3.2.4 Heavy Ion Therapy at GSI and in Heidelberg

At GSI, the German Heavy Ion Research Center, advanced treatment techniques using carbon ions (^{12}C) have been performed for ten years. The research and experience gained from results at GSI have lead to the construction of HIT in Heidelberg; a dedicated medical center for proton, helium and carbon ion therapy. The opening ceremony of HIT was held November 2nd, 2009 [38]. At HIT, treatments are carried out using active techniques where the beam is laterally deflected by magnets, while modulated in depth by varying the energy of the synchrotron. This method of intensity modulated particle therapy, is known as the rasterscan technique, and is a result of the joint effort at GSI and HIT. In Figure 3.9, the principles of the rasterscan technique is sketched. During rasterscan, the target volume is dissected into millimetre thick slices of iosenergetic levels and each slice is covered by a grid of pixels. The intensity controlled ion beam scans this grid precisely, remaining at one beam position until the prescribed dose as the calculated number of carbon ions has been reached. After one whole slice is completed, the beam is moved on to the next layer by changing the beam energy.

At HIT, the first carbon ion gantry in the world is introduced, offering a high level precision by allowing the therapeutic beam to be oriented around

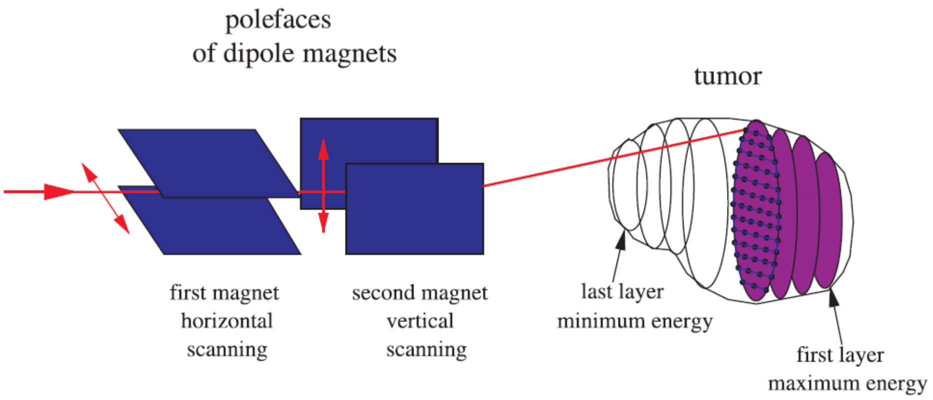

Figure 3.9: Intensity modulated particle therapy using the raster scan technique. During irradiation the beam is guided by the magnetic system in a row-by-row pattern through each slice that requires the same energy. [31].

the patient. In Figure 3.10, the dose distribution from a carbon therapy treatment using the beam scanning technique is shown together with the dose distribution from an IMRT photon treatment. The results illustrate the conformity that carbon ion beams can offer in comparison with advanced techniques of photon beam irradiation. These well conformed dose distributions are achieved with the dose being delivered from two beam angles for the carbon ion treatment, in contrast to ten beam angles during the IMRT photon treatment.

An additional advantage of the ^{12}C beam, is that some of the beam fragments produced during therapy are unstable isotopes of ^{10}C and ^{11}C. These isotopes are natural positron emitters and can be detected from outside the patient using a camera for PET. By recording the positrons emitted throughout the course of therapy, an on-line monitoring of the beam delivery is enabled. The PET imaging allows for an accessory quality assurance of the beam positioning.

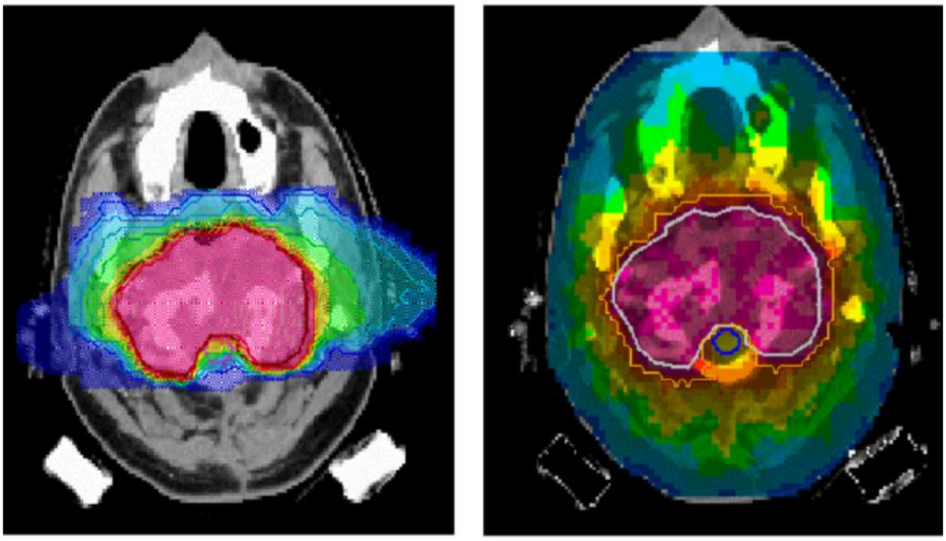

Heavy Ions (2 Fields) IMRT (9 Fields)

Figure 3.10: Comparison of treatment plans using carbon ions from two field angles (left) and a photon IMRT treatment of nine fields with photons (right). In both cases the conformity to the target volume is good, but for the treatment using carbon ions, the dose to normal tissue is less than what it is in the IMRT photon plan [35].

Chapter 4

Neutron Contribution in Photon Therapy

Unwanted dose contribution outside the target volume during photon therapy have different origins. From considering the depth dose curves of photons, it is evident that a large fraction of the photon dose is deposited outside the target volume, both in front of the target volume and as exit dose at greater depths. Laterally, the collimators conforms the beam considerably. However, photons scattered from the field inside the patient will deposit a substantial dose outside the treatment volume to the sides. Lower levels of unwanted doses are associated with more peripheral areas of the tissue. Photons contributing to peripheral doses are scattered photons and the photons leaking from the treatment head. In addition, there will be a dose contribution from neutrons, mainly produced in the high-Z compounds of the collimators.

The greater part of the dose outside the treatment volume during photon treatments is by far the dose deposited in the entrance and exit channel of the photon beam. As treatment techniques develops and are able to conform the prescribed dose in a better way than the conventional techniques, patients today have better prospects after therapy. However, with the increased patient survival rate, the long-term health effects associated with low dose levels to healthy tissue, have become a significant health issue [39]. Specific patient data have shown that the exposure to ionizing radiation above 50-100 mSv increases the risk of irradiation induced secondary cancer up to 30 years after the initial treatment [3].

Photoneutron production in matter was explained in Section 2.1.4. In the following the production of neutrons during radiotherapy with photons are described.

Table 4.1: Relative dose contributions from photons and neutrons outside the target volume using different treatment energies. Results from Kry et al [41].

	Peripheral Dose Contribution	
Linac setting [MV]	**Photons** [%]	**Neutrons** [%]
6	100	0
10	98	2
15	70	30
18	45	55

4.1 Neutron Production

Medical linacs operating above the (γ,n) threshold of the collimator materials (7 to 8 MeV for tungsten and lead), will produce neutrons [40]. Besides the dominant production in the linac constituents, photoneutrons can be produced in the patient and in the bunker walls, floor and ceiling. As the treatment energy increases, the neutron contribution escalates. Relative contributions of peripheral dose from photons and neutrons at various treatment fields are shown in Table 4.1. In a 15 MV photon field, the neutrons represent 30% of the peripheral dose contribution during the treatment. Above linac settings of 18 MV, the neutron component becomes dominant.

The photoneutron production is governed by the GDR of a given material as was described in Section 2.1.4. The constituents of the human body are of typically low mass numbers and have mean GDR energies located between 20 and 25 MeV. Accordingly, photoneutron production in the patient body is not of significance unless linac settings above 20 MV are applied. The heavier composites of the linac head have primarily been chosen for their photon shielding properties. In Table 4.2, the photoneutron energy thresholds for typical collimator constituents are listed. For tungsten and lead, the photoneutron production is well within reach for photon beams of 15 MV. The GDR for (^{208}Pb) is shown in Figure 4.1. As can be seen, the cross section of the (γ, n) reaction has its peak just below 14 MeV.

The various configurations of the collimators, filters and other structures in the treatment head, can result in substantial differences in neutron production. An example of percentage neutron production in the components for one linac configuration is given in table 4.3. As can be seen, the main neutron contribution comes from the primary and secondary collimators.

According to literature [42], the neutron production in the treatment head results in a total produced neutron fluence on the order of 10^{11} n.cm^2 per Gy photon dose. The photoneutron energy spectrum produced in the compounds of the linac have been calculated by several groups, e.g. Vega-Carrillo et al [2]: The photoneutrons produced by 8 and 10 MV photon

Table 4.2: Energy thresholds for (γ, n) reactions in various nuclei typically found in the linac head [40]. Tungsten (W) and lead (Pb).

Isotope	**(γ, n) threshold energy [MeV]**
^{182}W	8.07
^{184}W	7.41
^{186}W	7.19
^{206}Pb	8.09
^{207}Pb	6.74
^{208}Pb	7.37

Table 4.3: Monte Carlo calculations by Howell et al [4]. Example of relative neutron yield in each of the major components in the accelerator head using 18 MV photons, having secondary collimators and MLCs fixed at 10x10 cm^2 and 5x5 cm^2 field sizes, respectively.

Gantry head component	**Neutron production per Gray photon dose**
Target	14%
Primary collimators	51%
Flattening filter	8%
Secondary Collimators	18%
MLC	7%
Other	2%
Total	100%

beams are from the evaporation process only. As linac field settings reach 15 MV, additional knock-on photoneutrons of higher energies are produced. The photoneutron energy spectrum produced in the treatment head using 15 MV photon beams, have consequently two contributors; the evaporation component in the lower part of the spectrum, and a direct knock-out component at energies above the (γ,n) threshold. In 15 MV photon beams, the contributions are 90% and 10%, respectively. This results in the majority of the neutrons having an isotropic angular distribution, and a fraction of one out of ten will be forward peaked with a higher energy than the residual neutrons.

4.2 Moderation of Neutrons in the Treatment Head

Both tungsten and lead are accomplices in photoneutron production, however, they do also have a somewhat moderating effect on neutrons. Figure 4.2 shows how the neutrons, by inelastic scattering, decrease in energy as they traverse tungsten and lead. The result is neutrons emerging from the

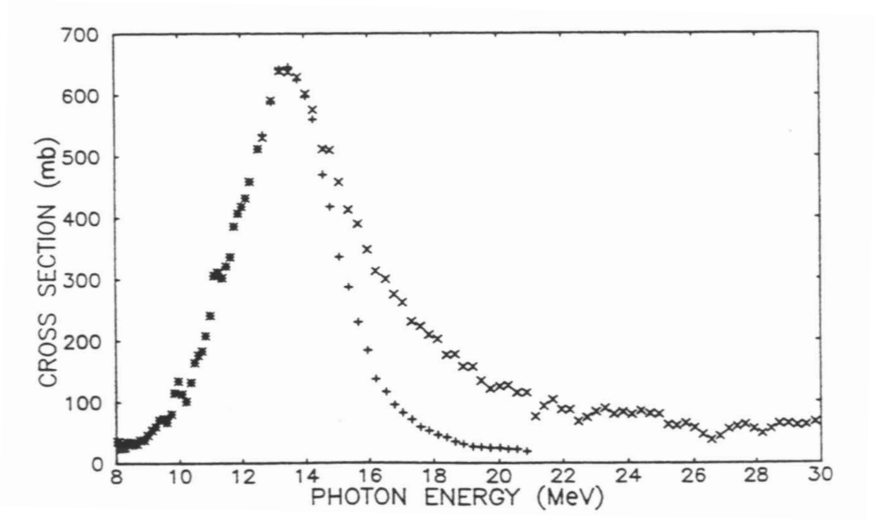

Figure 4.1: The GDR in lead (^{208}Pb). The (γ,xn) and (γ,1n) cross sections are represented by cross and plus signs, respectively [11].

treatment head with approximately the same fluence as initially produced, but with a significantly lower energy. This is beneficial from a radiation protection point of view, due to the lower RBE of the moderated neutrons.

The cross sections for neutron absorption in heavy materials are very small except at thermal energies, and little attenuation of neutron fluence will occur in the treatment head. If the shielding in a machine consist entirely of tungsten, as much as 15% of the fluence can be absorbed [11]. If solely lead shielding is used, close to zero neutron attenuation would result. In fact, a small build-up of neutron fluence can result due to (n, 2n) reactions.

4.3 Neutrons in the Patient Plane

The spectrum of neutrons reaching the patient is a result of the production, the angular distribution, and the moderation as the neutrons traverses the linac head. Further, the individual designs of machines and linac rooms as well as the various treatment modalities applied based upon the individual considerations for each patient, results in differences in dose contributions from neutrons. The IMRT treatment technique is a demanding modality with respect to the output of the machine and requires approximately 3-4 times more MUs than the 3D-CRT technique [4,43]. The low doses received

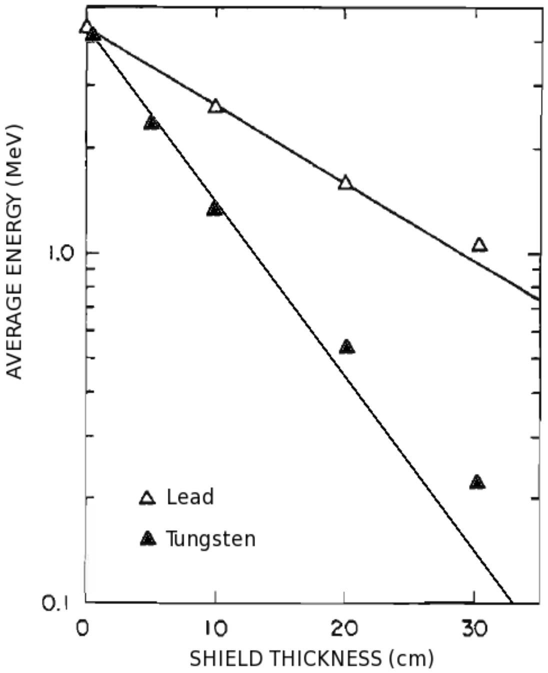

Figure 4.2: Neutron energy moderation in lead and tungsten. The average energy of the spectra measured from a neutron source (Pu-Be) as a function of the thickness of spherical shell shields surrounding the source. Tungsten has a superior moderating effect [11].

outside the target volume can be related to the number of MUs, and can during IMRT lead to an increased area of low dose in the patient [44,45].

According to literature, the measured fluence in the isocenter plane of a 15 MV linac is in the order of $10^6 - 10^7 \, n.cm^{-2}/Gy$ with mean neutron energies reaching from 0.2 to 0.4 MeV, depending on the distance from the central beam axis [46]. Figure 4.3 shows a Monte Carlo calculation of photoneutron energy spectra in the isocenter plane, 8 cm from the central beam axis [47]. Three different configurations of the secondary collimators and the MLCs have been applied. Mutual for all three spectra are the two characteristic features corresponding to evaporation and knock-out neutrons; the evaporation component peaking in the range 200 to 700 keV, and the direct component above 2 MeV.

The neutron dose contributions are in the literature reported to be on the order of mSv per Gy. (Ranging from 0.5 - 4 mSv) [4,47–49]. Another

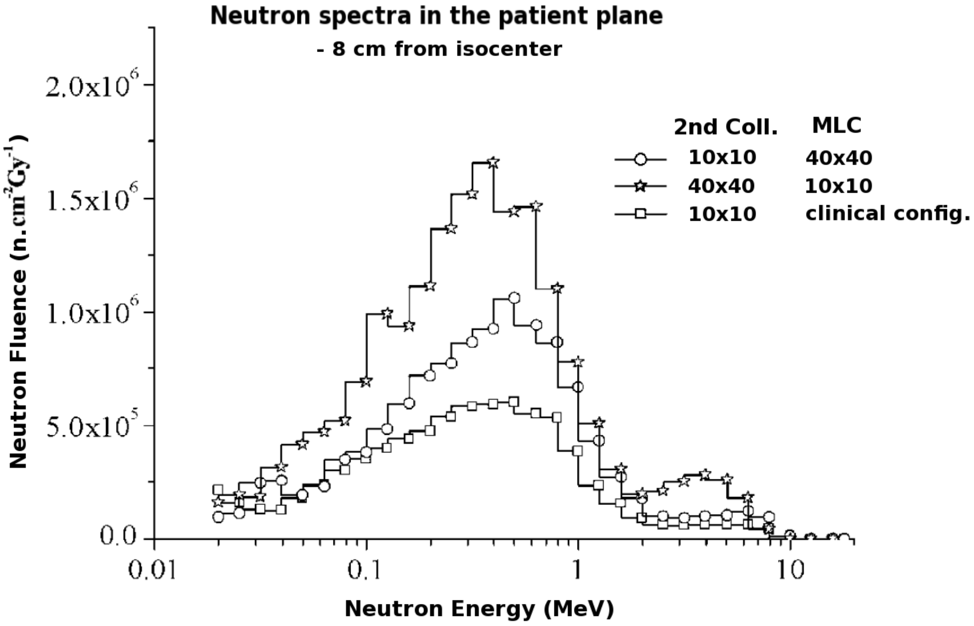

Figure 4.3: Monte Carlo neutron energy spectra in the isocenter plane, 8 cm from the central beam axis calculated by Zanini et al [47]. The neutron fluence for three different combinations of secondary collimators and MLCs are presented.

circumstance that affects the neutron contribution from the linacs besides the treatment energy, is the type of treatment technique employed.

Chapter 5

Neutron Detection

Neutrons are detected via the charged particles they produce in both inelastic and elastic nuclear reactions. Neutrons are only capable of ionizing indirectly due to their lack of electromagnetic charge, and detection therefore relies on appropriate absorber materials. The detection depends on the neutron energy, the sensitivity required, the radiation field of where the detection is to be performed and whether the aim is to unfold an energy spectrum (spectrometry) or to establish a presence of neutrons [12]. Due to the distinct difference in detection mechanisms from the; (1) slow, to the (2) fast and the intermediate neutrons, a division line is set between these two categories.

5.1 Slow Neutrons

When detecting slow neutrons, the elastic recoil energy of the absorber is negligible and the inelastic scattering will be the dominating process. All the common reactions used to detect slow neutrons result in heavy charged particles. Possible reaction modes are listed below [9]:

$$neutron \ + \ target \ nucleus \ \longrightarrow \left\{ \begin{matrix} recoil\,nucleus \\ proton \\ alpha\,particle \\ fission\,fragment \end{matrix} \right\}$$

In choosing a proper detector material, several considerations must be taken into account. In case of application in a mixed radiation field, the choice of material depends on the reaction mode to provide a sufficient discrimination against the competing processes of the other particles in the field. For this purpose, the Q-value, or the energy transferred from the neutron to the reaction products should preferably be high. If an improved sensitivity is a

Table 5.1: Nuclear reactions used for detection of slow neutrons. Q-values of the reaction products and the cross sections for absorbing a thermal neutron [9, 12].

	Reaction	**Q value (MeV)**	**Cross Section (barns)**
I	${}^{10}_{5}B + {}^{1}_{0}n \rightarrow {}^{7}_{3}Li^{+}\ {}^{4}_{2}He$	2.79 (2.31*)	3840
II	${}^{6}_{3}Li + {}^{1}_{0}n \rightarrow {}^{3}_{1}H +\ {}^{4}_{2}He$	4.78	940
III	${}^{235}U + {}^{1}_{0}n \rightarrow fission\ fragment$	~200	~2000

priority, a high cross section is required.

The three most important nuclear reactions for slow neutron detection are listed in Table 5.1, along with the kinetic energies of the reaction products and the cross sections for absorbing a thermal neutron. With the incident kinetic energy of a thermal neutron being negligible, the sum of the reaction products are equal to the Q-value itself.

The ${}^{6}Li$-reaction listed secondly is utilized in the thermal neutron detectors used in this work. The reaction is commonly applied in scintillation detectors which will be further described in section 5.5. For slow neutron detection in general, various other detection techniques exist. Some of the detectors commonly applied are briefly described in the following:

Proportional gas counters

A frequently applied neutron detector is the proportional counter using BF_3 (boron trifluoride) gas [15]. This is an active detector producing pulses of heights at the Q-values of the ${}^{10}B$ reaction described in Table 5.1. The counter is capable of pulse discrimination in mixed fields, except in intense photon fields where discrimination can be difficult.

Fission counters

Slow neutron induced fission of ${}^{233}U$, ${}^{235}U$ or ${}^{239}Pu$ is employed in fission counters [12]. The Q-value of each fission reaction is in the order of 200 MeV, resulting in large fission pulses from the fragments. This feature enables slow neutron counting at low flux levels, even in high background radiation environments.

Activation foils

Activation foils are passive detectors and exist in a variety of materials, e.g. Mn, Ag, and Au. When exposed to slow neutron radiation, the neutrons are absorbed and thereby they induce radioactivity in the foil that subsequently can be measured by a suitable counter.

5.2 Intermediate and Fast Neutrons

Nuclear reactions can also be used in detection of neutrons of intermediate and fast energies. In addition, neutrons of such energies, can transfer a detectable kinetic energy to nuclei by elastic scattering. The detection methods of fast and intermediate neutrons are divided into four groups: neutron moderated detection, nuclear reactions, elastic scattering alone and foil activation.

Neutron moderated detection

Detection of intermediate and fast neutrons can be obtained by covering detectors used for detection of slow neutrons with a moderating material. Suitable materials for this purpose are of low atomic numbers, where the mass of the atoms are close to the neutron mass. Bonner spheres are an example of such a system, where moderating polyethylene spheres of different diameters surrounds lithium scintillators. Neutron spectral information can be inferred from these devices that are widely used in dose measurements. The BF_3 counter is also frequently used in combination with a moderating material.

Nuclear reaction detection

Neutron spectrometry can also be achieved by utilizing the nuclear reactions ^6Li or ^3He. The cross sections of these reactions are several orders of magnitudes lower than the cross sections for the slow and intermediate neutrons, and are therefore less common. To retrieve the energy spectrum information, the pulse spectrum of the reactions must be analysed.

Elastic scattering

High energy neutrons can produce proton and hydrogen recoils in solid and liquid materials. The entire recoil energy can be detected providing a neutron energy spectrum. The elastic scattering process is utilized in the bubble detector spectrometry detectors used in this work, as described in Section 5.4.4.

Threshold foil activation

The threshold activation foils detect amounts of induced radioactivity, as in the slow neutron activation foils. By utilizing various foils of different nuclear reaction energy thresholds, a neutron spectrum can be obtained [12].

Fission counters

Fission counters can also be applied in the detection of fast and intermediate neutrons. ^{238}U can be utilized for this purpose and have the capability of discriminating against light ionizing particles and photon radiation [50].

5.3 Detectors In a Mixed Photon Neutron Field

The required properties of a neutron detector depends on the type of radiation environment the detector is to be applied in and which quantities that is to be obtained. In the surroundings of a 15 MV medical linac, the radiation environment consists of pulsed photon beams and bursts of neutrons induced by the photons. In order to obtain the neutron fluence and dose under such circumstances, important detector characteristics are:

1) Discrimination against photon radiation.
2) Passive readout is preferred due to the pulsed beam that would make an active device suffer from dead time losses.
3) Devices that enables a neutron spectrum to be attained, due to the energy dependent biological effects of neutrons.
4) High sensitivity, near tissue equivalent dose response.

The bubble detectors applied in this work exhibit all these four requirements listed above. As for the TLD detectors used, they likewise are able to meet the conditions stated above. However, during the measurements in this thesis, TLDs were only applied for thermal neutron detection. To perform spectrometry with TLDs, proper moderating materials must be utilized.

Other benefits of bubble detectors and TLDs are that both detectors are small in size, they consist of a material near tissue equivalent, and none of them are in demand of any electronics during exposure.

Bubble detectors have been applied in neutron detection around medical linacs by several groups [1, 48, 51, 52]. Moderators are commonly used with thermoluminescence detectors [2, 45, 53] or surrounding activation foils [40, 54]. Monte Carlo simulations on the subject are also performed [42, 51].

5.4 Bubble Detectors

Superheated Drop Detectors (SDD) and Bubble (damage) Detectors have in the past two decades been utilized in personal neutron dosimetry. The International Commission on Radiation Units (ICRU) and Organization for Standardization (ISO) currently recognise them under the collective classification superheated emulsions, comprising the two types mentioned and all other similar detectors manufactured [55]. This miniature relative of the bubble chamber was first suggested by Apfel in 1979 [56], and have found its application in nuclear science, safety, and medicine. The passive versions for personal dosimetry offer high sensitivity and dose equivalent responses accompanied by photon discrimination [57], as well as discrimination against any possible protons [58]. Still, reservations on reliability and durability have somewhat hindered a widespread adoption in dosimetry services [59].

Two laboratories have been the primary developers of the superheated emulsion technology and has promoted the creation of two commercial companies; SDDs at Yale University[1] and bubble detectors at Bubble Technology Industries (BTI)[2]. The general detection principles of the SDD and bubble detector are similar, but have two important distinctions: 1) The host media in the SDD is an aqueous gel and the host media in the bubble detectors is a stiffer polyacrylamide. 2) The SDD is mostly used as an active detector together with an acoustic sensor, whereas the bubble detector is used as a passive device. The BDs are utilized in this work and will in the following be explained.

5.4.1 General Principles

Bubble detectors utilize thousands of microscopic superheated droplets suspended in an elastic polymer medium. A substance is considered as superheated if its liquid state is maintained above the normal boiling point of the substance. These droplets of freon-based compounds, have a radius of less than a 100 micrometers, and maintains pressure and temperature adjusted such that the superheated droplets become metastable. Neutrons can interact with the atoms of the superheated liquid droplets, resulting in the formation of energetic, recoil ions. The recoil ions can further trigger the droplets to undergo a phase transitions into visible bubbles [60]. The number of bubbles in a detector is proportional to the initial neutron exposure. Figure 5.1 shows bubble detectors, both exposed and unexposed to

---

[1] Apfel Enterprises Inc.,25 Science Park, New Haven, USA.

[2] Chalk River and BTI Chalk River, Ontario, Canada.

Figure 5.1: Bubble detectors. Left image shows a bubble detector after exposure to neutrons. Right image shows two unexposed types of bubble detectors.

neutrons.

5.4.2 Physics of Bubble Formation

The physics of the bubble formation taking place in a superheated liquid is known as the 'thermal spike theory' or the 'Seitz theory' [61]. This theory postulates that the formation of a visible bubble requires the neutron produced recoil ion to deposit a minimum energy, E_{min}, inside a liquid droplet. The process involves two critical steps: 1) Formation of a critical size vapour bubble inside the superheated liquid medium. 2) The growth of this vapour bubble into a macroscopic, visible bubble:

Step 1

A bubble of critical size has a radius on the order of nanometres, and is calculated using classical macroscopic concepts of pressure and surface tension. Figure 5.2 illustrates a static vapour bubble inside the superheated liquid droplet. The vapour bubble is exposed to an external pressure, p_e, along with the pressure from the surface tension from the liquid, σ, aspiring to compress the bubble. From the inner surface of the bubble, an internal vapour pressure, p_i, is working outwards, attempting to expand the bubble. The conditions of a critical size bubble formation of radius r_c, are achieved

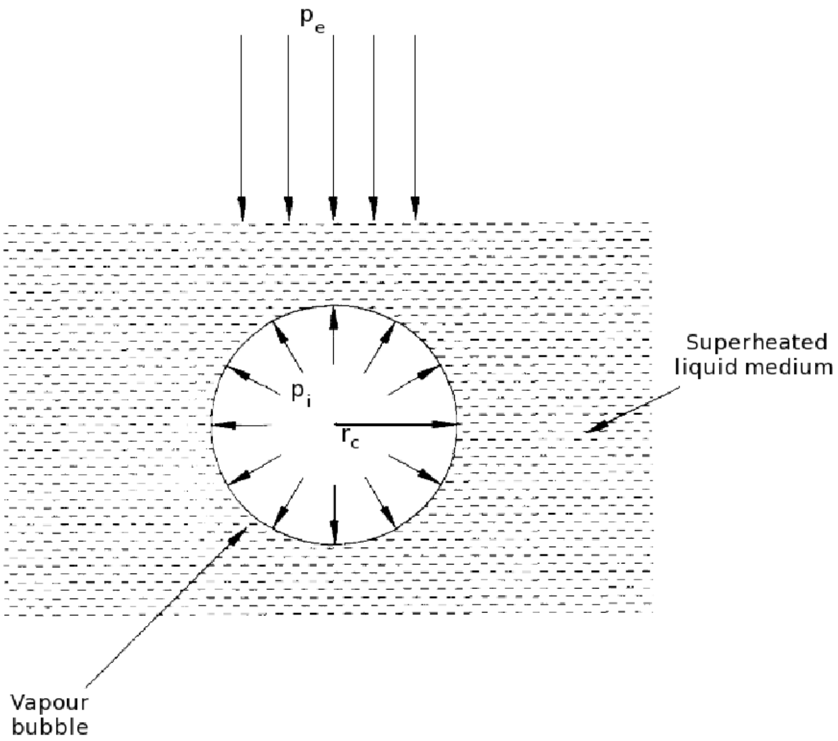

Figure 5.2: A vapour bubble of radius, r_c, inside a superheated liquid droplet. The external pressure, p_e, along with the surface tension, σ, make up the external pressure working to compress the bubble. The internal vapour pressure, p_i, attempts to expand the bubble [58].

when the inward pressure are balanced by the outward pressure:

$$p_e + \frac{2\sigma}{r_c} = p_i. \tag{5.1}$$

The second term represents the effective surface tension from the liquid.

Step 2

A vapour bubble of a critical size is thermodynamically unstable, and is sensitive to slight perturbation. If the vapour bubble radius becomes smaller than r_c, the cavity collapses under the effects of the external pressure. On the other hand, if the vapour bubble radius exceeds r_c, it will expand into a macroscopic, visible bubble.

The minimum energy, E_{min}, required for visible bubble formation is a combination of the two steps, and expressed by Seitz as

$$E_{min} = 4\pi\sigma r_c^2 + \frac{4}{3}\pi r_c^3 \rho_\nu \frac{H}{M}, \tag{5.2}$$

where ρ_ν is the vapour density, whilst H and M represent the molar heat of vaporization and molecular weight respectively. The first part of equation 5.2 correspond to the energy required to form a critical size bubble (step 1), whereas the second term represents the energy demanded for expansion into a bubble of a visible dimension (step 2).

The bubble detectors are highly sensitive to changes in temperature and pressure. With rising temperature, the compressing surface tension, vapour density and the heat of vaporization will decrease, whilst the difference between external and internal pressure is increased. Rearrangement of Equation 5.1 yields

$$r_c = \frac{2\sigma}{p_i - p_e} = \frac{2\sigma}{\Delta p}. \tag{5.3}$$

The effect of a decrease in surface tension and an increased pressure difference, Δp, results in a lower critical radius. This further leads to, considering term 1 in Equation 5.2, a lower threshold energy required to form an initial critical bubble.

It is possible to connect the minimum energy required for bubble formation, E_{min}, to the stopping power of the recoil ion [62]. By defining an effective interaction length, L, over which the energetic recoil particle transfers its energy in the liquid droplets, a relation to the dimensions of the critical bubble, r_c, is postulated. By assuming that the stopping power is constant, L is linearly related to the critical radius, r_c, such that $L = kr_c$, where k is a dimensionless coefficient. Knowing the relationship between L and r_c enables one to predict the stopping power needed to create a bubble. If L is assumed to be much shorter than the total length travelled by the recoil particle, the energy deposited over the length, L, is given as:

$$E = L\left(\frac{dE}{dx}\right)_{avr} = kr_c\left(\frac{dE}{dx}\right)_{avr}, \tag{5.4}$$

where $\left(\frac{dE}{dx}\right)_{avr}$ is the average stopping power. A lower threshold value of $\left(\frac{dE}{dx}\right)_{avr}$ can be found. No nucleation can occur under this value, $\left(\frac{dE}{dx}\right)_{min}$, given that the other parameters are fixed. The minimum average stopping power required for bubble formation is retrieved from Equations 5.2 and 5.4 expressed as:

$$\left(\frac{dE}{dx}\right)_{min} = \frac{E_{min}}{kr_c}. \tag{5.5}$$

The right hand side of equation 5.5, depends strictly on the thermophysical properties (temperature and pressure) of the superheated liquid. It is therefore possible to determine the exact stopping power of a recoil ion needed in order to form a bubble, given that the temperature and pressure are fixed. This property is exploited in making bubble detectors with unique energy thresholds, and forms the basis of using bubble detectors within neutron spectrometry.

5.4.3 Detector Response

From the previous sections it is evident that the bubble formation depends on the neutron energy, as well as the temperature. The response rate, R (bubbles per second), for neutrons of an incident energy, E_n, with temperature, T, of the superheated liquid drop is given as [60]:

$$R(E_n, T) = \phi(E_n) V \sum^{n} N_i \sum^{m} \sigma_{ij}(E_n) F_{ij}(E_n, T)\,, \tag{5.6}$$

with

Symbol	Definition
$\phi(E_n)$	is the incident neutron flux ($n/(cm^2 s)$)
V	is the total volume of superheated liquid (cm^2)
N_i	is the atomic density of the i^{th} species in the liquid ($atoms/cm^3$)
$\sigma_{ij}(E_n)$	is the microscopic cross section for a j-type reaction in the i^{th} species, at neutron energy E_n (b)
$F_{ij}(E_n, T)$	is the efficiency factor for a j-type reaction in the i^{th} species for a particular liquid temperature T and incident neutron energy E_n (dimensionless)
i	is one of the atomic constituents of the compound
j	is the type of neutron interaction

The visible bubbles will be of slightly different sizes. The size of the visible bubble formed depends on the initial droplet in which the visible bubble was created from, and does not reflect any property of the incoming neutron.

From Equation 5.6 it can be established that the number, size and chemical composition of the liquid droplets, as well as the holding polymer, can be varied to adjust the detection efficiency and the sensitivity of the detector to specific energies. In order to attain information about the neutron energy spectrum, a combination of such detectors having individual energy thresholds can be utilized.

As the energy deposition is caused by energetic recoils produced from elastic scattering neutrons, a satisfactory energy deposition is easily attainable within the fast and the intermediate neutron energies. For neutrons of thermal energy levels, elastic scattering processes are not able to create sufficiently energetic recoils. To make neutron detection at these energies possible in bubble detectors, a substance that creates energetic recoils by neutron absorption is incorporated in the polymer.

5.4.4 Bubble Detector Spectrometer - BDS

The BDS set is used for neutron spectrometry at energies covering 10 keV to 20 MeV.

Description of the BDS system

A complete package of spectrum detectors consists of 36 bubble detectors; six sets of six different detectors formulated such that the lower neutron energy thresholds equals 10, 100, 600, 1000, 2500 and 10 000 keV. The predominant reaction for bubble creation is elastic scattering recoil nuclei of carbon and fluoride [63].

The multitude of detectors is to ensure sufficient number of bubbles required to achieve adequate counting statistics, as the number of bubbles in each detector is limited. A normalized response of each detector can be seen in Figure 5.3. The response increases sharply above each detector threshold, and is more or less constant as the energy further increases. The indicative detector responses are around 0.1-0.2 bubbles/μSv. The detectors are calibrated at 20 ± 5°C, and have to be thermalized and wrapped in an isolating material if to be used at other temperatures [64]. In order to reset a BDS after exposure, the detectors are re-compressed in a hydraulic compression chamber, where over 400 psi are applied and recondences the bubbles back into a liquid state.

Spectrum deconvolution

To unfold the neutron energy spectrum, a method known as spectral striping is performed. This method assumes that the neutron spectral fluence can be represented by means of step functions with six energy bins. The lower edges of the bins are the energy threshold of a given detector, whereas the highest energy is assumed to be 20 MeV. The fluence distribution is determined by starting from the highest energy bin, and progressively the fluence of the lower energy bins are unfolded by weighting each detector response with values taken from a provided response matrix of the detectors. The conversion procedure is further described in Appendix A. Spectral striping results in relatively high uncertainties in the fluence distributions, especially in the lower energy bins. Alternatively, if the aim is to obtain integral quantities such as dose equivalent, the uncertainties are smaller due to negative correlations in the adjacent energy groups [59]. Other more

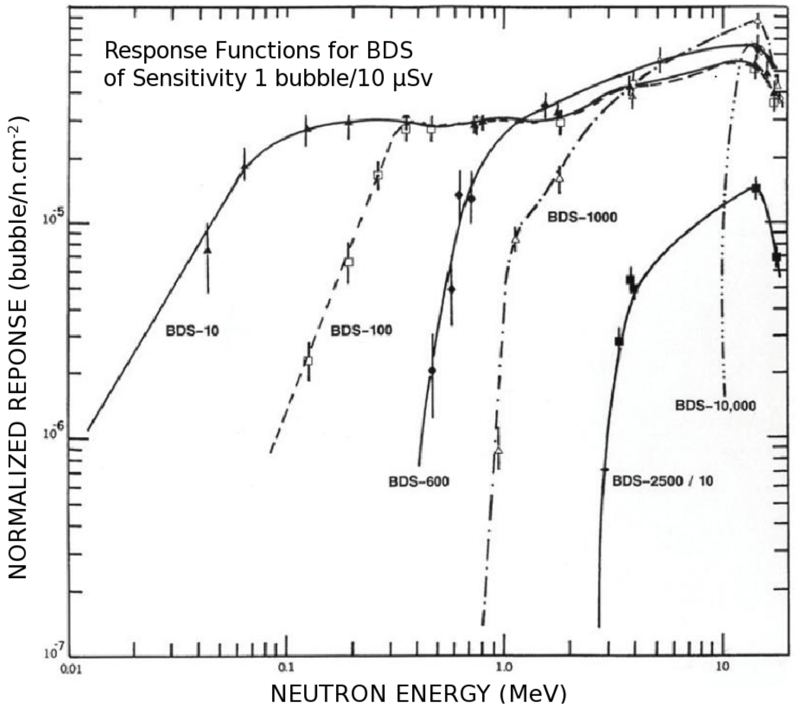

Figure 5.3: Response curves of the BDS detectors used for detecting neutrons of energies in thresholds between 10 keV and 20 MeV [64].

complex algorithms for obtaining the bubble detector neutron spectrum has also been developed, such as the unfolding code BUNTO [13].

5.4.5 Bubble Detector Thermal - BDT

The BDT bubble detectors are intended for thermal neutron monitoring. A ^{6}Li compound is dispersed within the elastic polymer, specifically formulated to detect preferentially the α particle from the reaction $^{6}\mathrm{Li}(\mathrm{n},\alpha)^{3}\mathrm{H}$. The response is proportional with the ^{6}Li cross section, having increasing responses as the neutron energies decrease [65]. The sensitivity of the BDTs is approximately 2.7 bubbles/μSv, and have a response to fast neutrons a factor of ten times lower than the response to thermal neutron energies [66]. To reduce the temperature dependence of the detector, a compensating material is added on top of the polymer in the tube. When the temperature increases, the compensating material will inflict an extra pressure on the polymer that corrects for the higher degree of superheat in the droplets. The BDTs are calibrated by the manufacturer and are supplied with response to dose equivalent conversion factors. The conversion factors are the mean response results of a calibration performed at five different temperatures ranging from 20-37 °C. The BDTs are supplied with an integrated compression system, that enables compression with a piston screw on top of the closed vial.

5.4.6 Limitations

Several limitations exist in neutron detection with bubble detectors. Some of the constraints are briefly reviewed in the following:

Durability

One of the weaknesses of the bubble detectors is their limited life time. The BDS detectors are initially sealed with a volatile liquid keeping them pressurized. In order to make them sensitive to neutron radiation, they must be activated by removing the seal and let the liquid vaporize. After activation, the manufacturer guarantees an optimum detector performance for three months, or alternatively reuse of ten cycles. As the detectors age, water will diffuse from the polymer out of the detector tube or into the detector droplets, inflicting a swelling effect on the polymer. The effects of ageing will usually cause the sensitivity of the detector to change, both in altering the properties of the detector fluid and in degrading the detector volume from visible signs of ageing [6]. The image in Figure 5.4 shows bubble detectors with signs of ageing.

The BDTs are closed detectors, and the diffusion of water out of the detector is less dominant. If stored under the proper temperature and humidity conditions, the BDTs have a potential lifetime of one or two years [65]. The manufacturers guarantee limit is nevertheless 3 months, and the sensitivity should be tested regularly as visible damages are not present in the BDT detector. Prior to activation, the detectors should have a shelf life of at least six months, depending on the temperature, the humidity and the time they are out of their storage tube.

Temperature dependence

Ambient temperature variations in the bubble detectors will modify both the energy threshold and the overall sensitivity which strongly affects the response, as was explained in the previous sections. If the detectors are used at temperatures above that of the calibration, the result is a downward shift in the neutron energy thresholds [67]. In measurements performed by Ytre-Hauge [6], it was seen that an increase of 2°C can result in a 50% rise in the detector response, depending on detector type. The BDS detectors are calibrated by the vendor at 20 ± 5°C, and must, in order to correctly employ the calibration factor supplied, be operated in a temperature controlled environment or wrapped in an isolating material after being kept in a 20°C water reservoir.

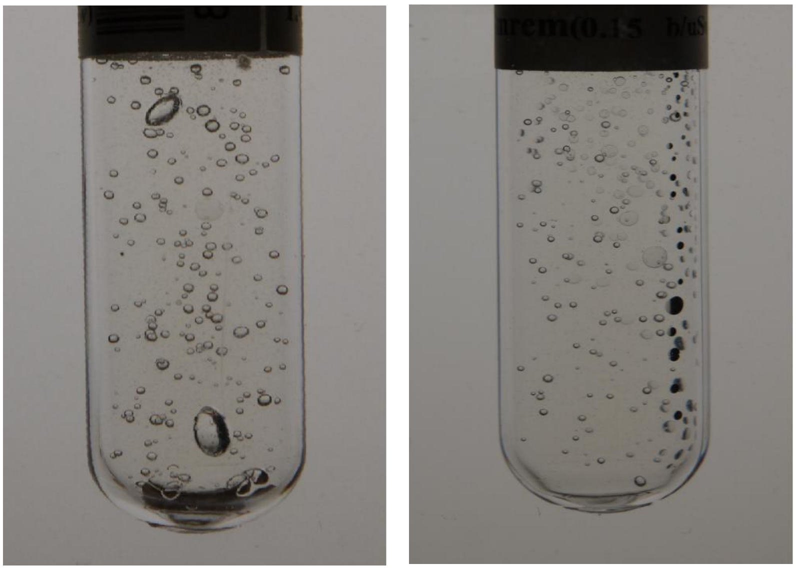

Figure 5.4: Bubble detectors with signs of ageing. The detector on left hand side has two large bubbles which are no longer possible to re-compress into droplets. On the right hand side, several small surface bubbles are trapped against the detector wall. These effects tend to complicate the process of bubble counting [6].

Range limitations

A weakness of the bubble detectors is their limited range of usage [68]. As the number of bubbles become numerous, there is an increasing probability that the bubbles will overlap and cause a decrease in accuracy of the bubble count.

5.5 Thermoluminescence Detectors - TLD

TLDs are small lithium crystals that serves as a passive, integrating detectors when exposed to a field of radiation to which the TLD is sensitive. The crystal material is chosen such that the detectors are able to store the effect of irradiation at normal room temperatures. After exposure, information about the radiation can be extracted by heating the detectors while reading out the light yield. The principles and the physical mechanisms of the TLD is described in the following.

5.5.1 Band Structure and Electron Migration

The outer atomic shell level of a crystalline material, can be described by means of an energy band structure. This energy band model assumes that there exists a lower energy valence band which contains the electrons considered as bound at their lattice sights. In a higher energy conduction band, the electrons with sufficient energy to freely migrate within the lattice structure is situated. The upper and the lower band are separated by a forbidden band gap with no available energy levels for an electron to be situated. Depending on the width of the band gap, electrons can migrate from the valence band and up into the conduction band. The positively charged vacancy left in the valence band is called a hole, which together with the electron is referred to as an electron-hole pair. How attainable the creation of an electron-hole pair is, determines the level of conductivity of the material. Accordingly, the materials are classified as insulators, semiconductors and conductors. For insulators, the forbidden band gap is typically 6 eV, which is too wide for permitting elevation of electrons into the conduction band at normal temperatures. In a semiconductor, the width of the band gap is approximately 1 eV, and ionizing radiation or a thermal disturbance can cause an electron to migrate. For conductors, a typical metal, there is nearly no separation between the upper and the lower band, and electron-hole pairs are easily created.

5.5.2 Scintillation Mechanism

After the creation of an electron-hole pair, the electron will eventually de-excite back into the valence band and recombine with a hole by the emission of a photon. In a pure crystal, the band gap is usually to wide for allowing a visible photon to be emitted. To enhance the efficiency of the process, and adjust the energy level of the emitted photon, impurities, or activator sites, are added to the crystal lattice. The additionally available energy levels permits de-excitations in smaller steps, such that the electron-hole recombination is accompanied by the emission of visible light. The emitted visible photons can further be detected by a photomultiplier.

5.5.3 Thermoluminescence

The inorganic scintillation materials described above are used in active detection methods, and are constructed to emit light in the form of prompt fluorescence. TLDs are made from a different class of inorganic crystals that permits storage of the effect of the radiation at normal room temperatures. After irradiation, the crystal is heated to stimulate the emission of light that further on can be detected. The physical distinction of the passive TLDs, are the particularly impurities chosen for the creation of deep activator sites, referred to as trapping centres. This is illustrated in Figure 5.5.a. Incident radiation promotes electrons across the band gap in the usual way, leaving the positive hole in the valence band. The electron is further trapped in an electron trapping center; an available energy level situated below the con-

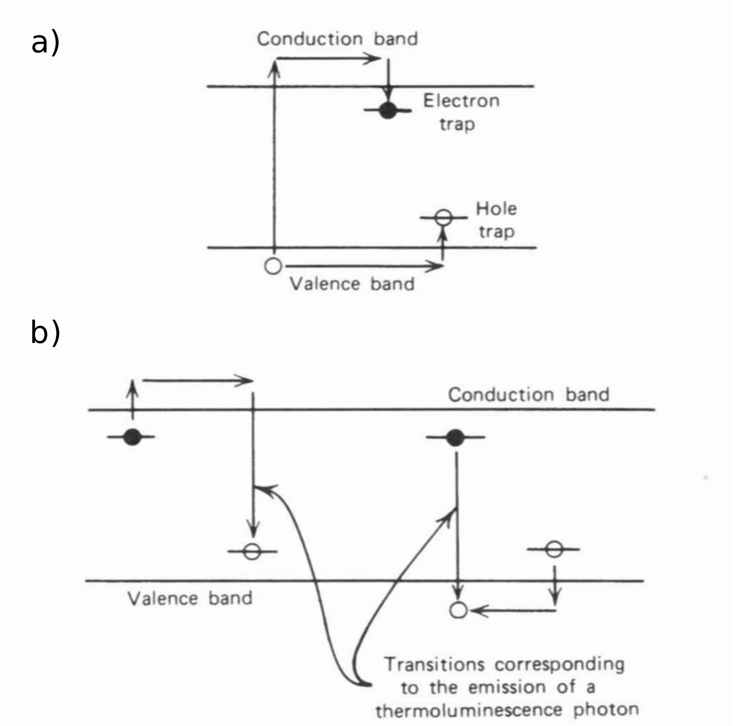

Figure 5.5: The mechanism of thermoluminescence. a) Incident radiation elevates electrons into the conduction band, leaving a positive hole in the valence band. The mobile electrons and holes, will further be captured at one of the trapping centers. b) At a temperature determined by the energy level of the trap, electrons and holes are released back into the conduction and valence band. The liberated electron can further migrate to a nearby hole and recombine with the emission of a photon (left in image). A similar process occurs for the hole (right in image) [9].

duction band. If the energy level of the trap is sufficiently deep, as is the case with the TLDs, a captured electron will have a very low probability of escaping at normal room temperatures. The holes will migrate to a hole trap situated right above the valence band, and will be held fixed in this position. Consequently, the number of trapped electrons and holes are a measure of the amounts of created electron-hole pairs by irradiation.

To liberate the trapped electrons and holes, the TLD material is heated. At a temperature determined by the energy level of the trapping centers, the electrons are excited back into the conduction band, as illustrated in Figure 5.5.b. Assuming the trapped hole needs a higher temperature to escape than the trapped electron, the now free electron may migrate to a nearby trapped hole and recombine. Alternatively, a trapped hole can escape at a temperature below the most probable temperature of release, and recombine

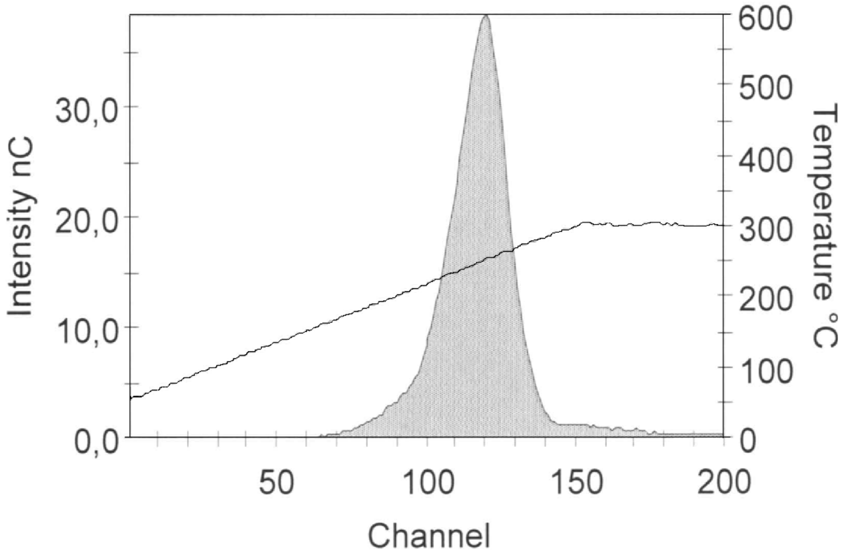

Figure 5.6: Example of a glow curve. The TLD material is heated gradually, and photons are emitted as the trapped electrons and holes gain enough energy to escape their respective traps and recombine. The photon yield is read out by a photomultiplier and registered as a function of the temperature. The integrated signal is a measure of the number of electron-hole pairs created during the exposure to radiation.

with a trapped electron. The two possible modes of recombination will both result in the emission of a photon in the visible light region, and is referred to as thermoluminescence [69].

The TLD read out system records the response of the TLDs after use. This system reads out each dosimeter by gradually heating them to typical temperatures of 300 °C, while recording the light yield with a photomultiplier. The signal is recorded as a function of temperature in a glow curve, as exemplified in Figure 5.6. The thermoluminescence response is then the integrated charge in nC. After read out the TLDs are annealed; exposed to elevated temperatures for a period of several hours which depletes all remnants of the trapped electrons and holes, and makes the dosimeters ready for reuse.

5.5.4 TLD Neutron Detection

For neutron detection in a mixed photon-neutron field, two types of TLDs have to be applied. The TLD-600 is both photon and neutron sensitive, whereas the TLD-700 is sensitive to photons [70]. With the application of both, the photon contribution can be subtracted. These small crystals are available commercially from several manufacturers, usually as Lithium Fluoride (LiF) supplied with additional activator materials. Natural lithium contains 7.4% ^{6}Li and is therefore primarily sensitive to thermal neutrons via the $^6\mathrm{Li}(\mathrm{n}, \alpha)^3\mathrm{H}$ reaction. By using lithium enriched with ^{6}Li (TLD-600), sensitivity to thermal neutrons is enhanced. In crystals containing nearly pure ^{7}Li (TLD-700), the sensitivity to thermal neutrons is suppressed [71]. The thermal neutron cross sections are 945 and 0.033 barns for TLD-600 and TLD-700, respectively [72].

The thermoluminescence response as a function of neutron energy of the two types of TLDs is shown in Figure 5.7. For TLD-600 in 5.7.a, the neutron response is increasing as energy decrease, and is significantly higher than the negligible neutron response of TLD-700 in Figure 5.7.b.

a) Total thermoluminescence from ^{6}Li

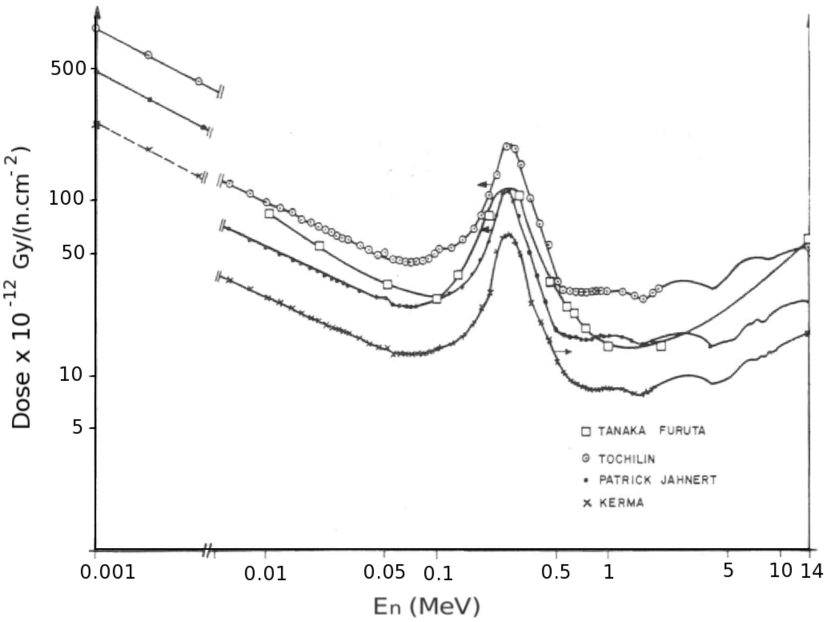

b) Total thermoluminescence from ^{7}Li

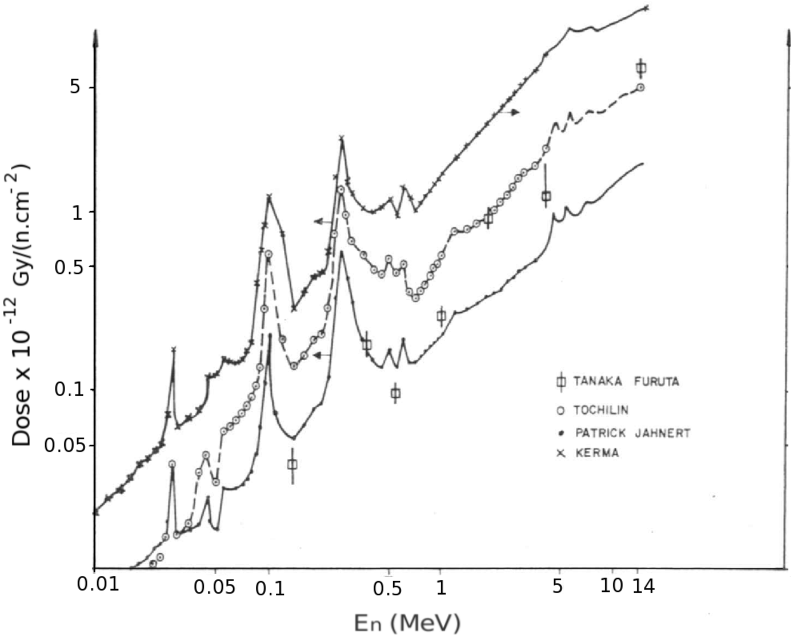

Figure 5.7: Thermoluminescence response of a) TLD-600 and b) TLD-700 as a function of neutron energy from 1 keV to 14 MeV. The y-axis is given in dose 10^{-12} Gy/(n.cm^{-2}). The curves are the results of individual experiments and calculations. Modified from Horowitz and Freeman [71].

Chapter 6

Experimental Set-up and Procedures

The measurements were mainly carried out with a 15 MV linac beam at HUS in Bergen. The experiments included detector characteristics and in-phantom neutron detection in various treatment field configurations. In addition to the measurements at HUS; further tests of the detectors were executed in the radiation field of the nuclear reactor at IFE.

The set-ups can be summarized in five variations of constant radiation fields:
(1) Photon field - 6 MV at HUS.
(2) Moderated photon field - 6 MV at HUS.
(3) Photon neutron field - 15 MV at HUS.
(4) Moderated photon neutron field - 15 MV at HUS.
(5) Photon thermal-neutron field - IFE.

In the following the measurement set-ups at HUS and IFE are described. A brief description is also given of the measurement procedures of the detectors and the dose plan system used for generating the treatment plans:

6.1 Set-up at Haukeland University Hospital

The neutron measurements were performed using a Varian 23 iX medical linear accelerator, being one of five linacs used for radiotherapy cancer treatment at HUS. Figure 6.1 displays the measurement set-up of the linac, there shown with a plastic phantom in the isocenter position on the patient table. The gantry is in a 90° angle, such that the photon beam is applied from the side. The measurements were performed in the isocenter plane, principally outside the actual treatment field. The tests without any moderation material were performed with the linac in an upright position at a 0° angle, whereas the linac head was rotated to 90° angle during the in-phantom

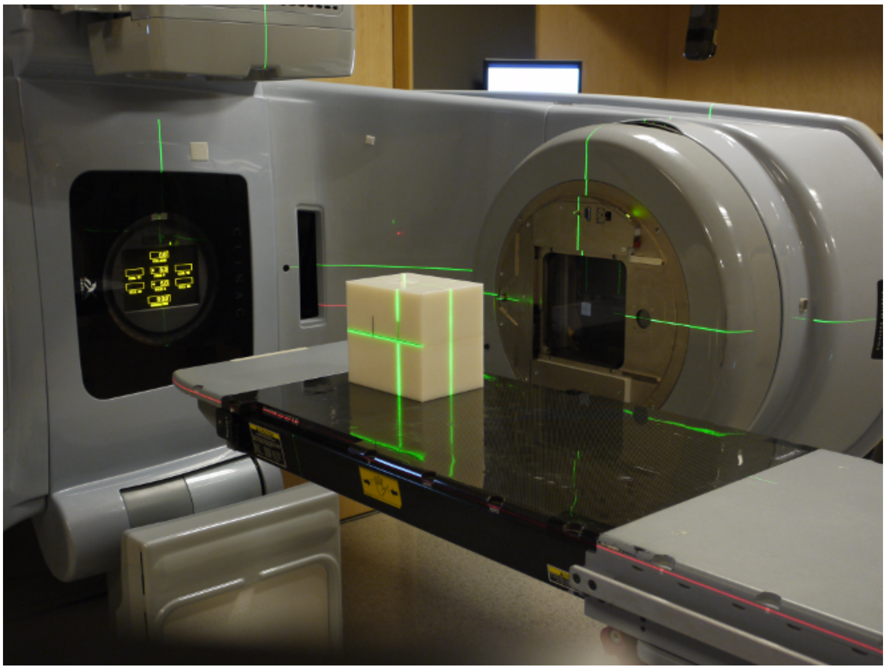

Figure 6.1: Example of a set-up with a phantom at HUS, with the gantry head in a 90° position. The laser lines are used for positioning with respect to the isocenter. The measurements were performed in the isocenter plane, both with and without the employment of the phantoms.

measurements. During those experiments at HUS that did not involve dose planning, the photon field was defined by the secondary collimators in a 5x5 cm^2 fixed position and having the MLCs extracted to their outher position.

The majority of the measurements were performed applying linac photon beams of 15 MV, resulting in a mixed photon neutron field. In order to perform photon calibration in a field without neutrons, the 6 MV photon beam was used under the assumption that the neutron production in this mode is negligible.

The number of MUs applied to achieve the requested dose during the measurements, were all estimated based on the specific photon energy and isocenter depth employed for each measurement. These calculations were performed manually with standard conversion tables for the manual fields shaped by the secondary collimators. As for the complex treatment configurations involving the MLCs, the dose plan system Eclipse was used to design the dose plans.

The phantoms and the dose plan system applied at HUS are described in the following:

6.1.1 Phantom Specifications

Two different phantoms have been designed for the neutron measurements at HUS. Both phantoms consist of water equivalent solid state plastic material, originally applied for moderation purposes in the radiation environment surrounding the medical linacs.

Phantom A

In Figure 6.2.a, Phantom A is shown. Phantom A was constructed with particular consideration for controlling the temperature of the BDS detectors. A cavity enabling insertion of insulating Styrofoam is fitted and positioned in such a way that the detector center is surrounded by at least 7 cm of material; 5 cm of the water equivalent phantom material, and 2 cm of insulating Styrofoam in all directions. As shown in Figure 6.2.b, the measurements in this phantom were performed 7 cm outside the isocenter. Both the BDS detectors and the TLDs were applied in these measurements in Phantom A.

Phantom B

In Figure 6.3.a, Phantom B is shown, in which both BDT and TLD measurements were performed. The phantom comprises 36 holes for insertion of detectors. Plastic rods are applied as filling material in the cavities when a position is left empty of detectors. As sketced in Figure 6.3.b, this phantom allows for measurements in multiple positions outside the field; here applied is a 5x5 cm^2 photon beam with isocenter depth at 8.6 cm.

6.1.2 The Dose Plan System Eclipse

The dose plan system Eclipse (Varian Inc. Palo Alto, Ca, USA) was used to calculate the dose distributions for the chosen field set-ups applied during the measurements. Eclipse was employed in creating a 3D-CRT dose plan and an IMRT dose plan to enable a comparison of the two treatment delivery techniques. The phantoms were scanned at the CT scanner used for acquiring CT images for radiation treatment dose planning. A CT volume of the phantom was reconstructed from the CT images and subsequently loaded into Eclipse for processing. The program Eclipse, calculates the optimal way of accomplishing a treatment within the conditions requested by the user. In Phantom A, a cylinder shaped volume has been contoured and defined as a target, as described in Figure 6.4. 2 cm behind the (red) target volume is a (yellow) cylinder shaped volume defined as an organ at risk, having assigned a restriction in dose level to this volume. In order to make comparable treatment plans of the two treatment techniques; 3D-CRT and IMRT, three fixed field angles have been applied as a common basis.

a) Phantom A

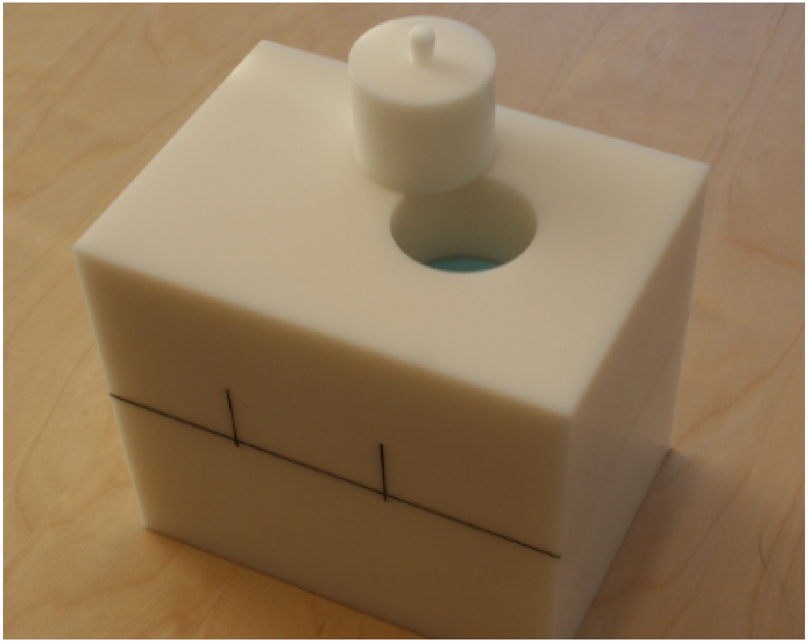

b) Phantom A top view

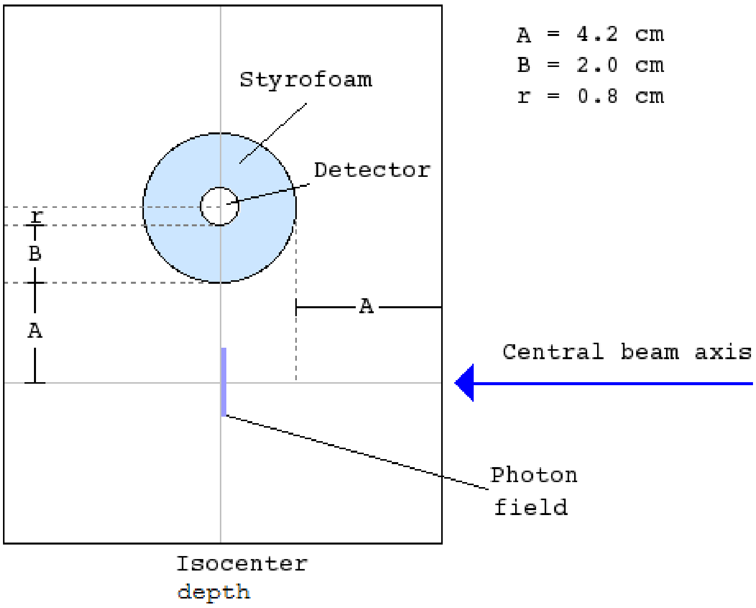

Figure 6.2: a) Phantom A has a cavity which has been filled with Styrofoam in order to insulate the bubble detectors. When the detectors are in position a lid of phantom material covers the top of the detector. b) Top view of Phantom A. The measurements were performed in the isocenter plane; 7 cm outside the central beam axis of the photon field at 7 cm depth.

a) Phantom B side view

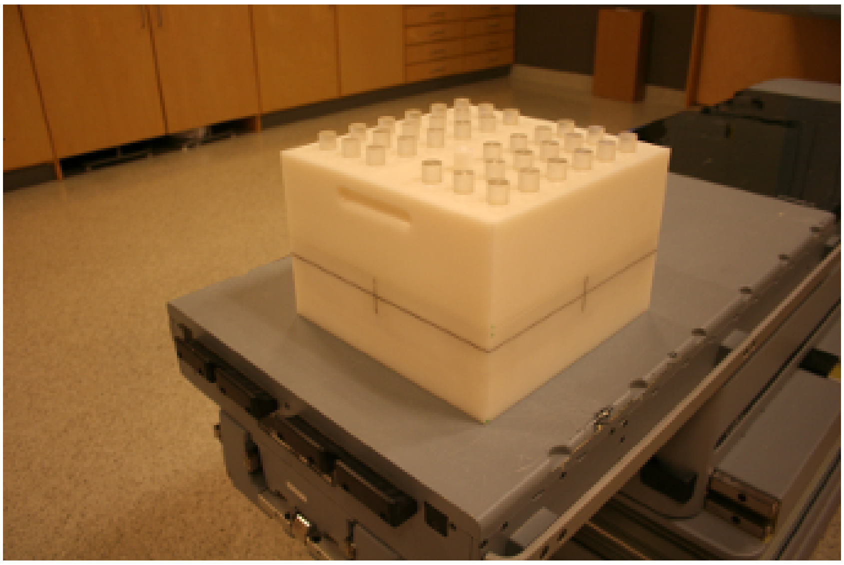

b) Phantom B top view

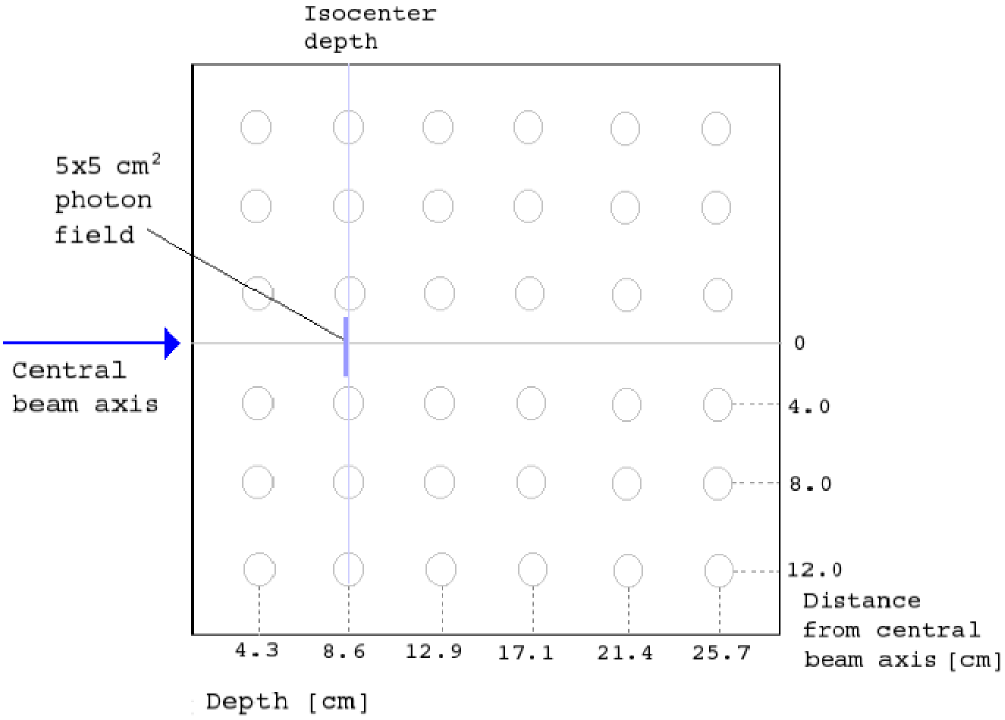

Figure 6.3: a) Phantom B side view. b) Sketch of the top view of Phantom B. The 36 holes allows for in-phantom measurements with BDs and TLDs in various positions.

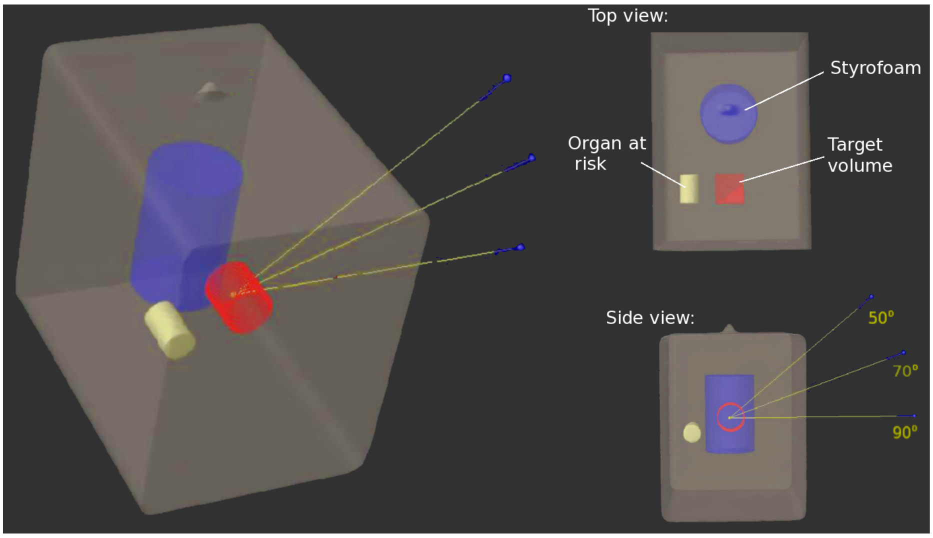

Figure 6.4: Following a CT-scan, a 3D image of Phantom A was generated in the dose plan system Eclipse. Volumes of particular interest have been defined; a red target volume and a yellow organ at risk. The blue volume is the Styrofoam insulating the detectors during the measurements.

For the Phantom B, no advanced treatment plan was created. Nevertheless, it was scanned into the treatment system in order to simulate the dose distribution from the field configuration that was applied.

The dose distributions calculated by Eclipse, does not include dose from neutrons or from photons leaking from the linac head.

6.2 Set-up at the Institute for Energy Technology

The detectors were tested in the mixed photon thermal-neutron field of the nuclear reactor JEEP II at IFE. IFE operates the only two existing nuclear reactors in Norway, and has its main office at Kjeller.

The JEEP II is mainly a research reactor which uses heavy water for both cooling and moderation. The reactor uses low enriched Uranium-235 as fuel (3.5% U-235) in the form of uranium dioxide, and the reactor has a thermal output of 2 MW [73]. During the fission reactions, an incident thermal neutron enters the nucleus of U-235 and splits it into two large fragments accompanied by an average of 2.5 prompt neutrons and more than 10 photons [74]. The neutrons resulting from the reaction are moderated in heavy water in order to further induce fission. To sustain the necessary chain reaction, one thermal neutron is required. The residual neutrons will either be captured by cadmium rods in the reactor core or they will contribute to the radiation environment outside the core. An example of one of the many reactions in the fission process of U-235 is:

$$^{1}_{0}n +^{235}_{92} U \rightarrow (^{236}_{92}U)^{*} \rightarrow^{140}_{55} Cs +^{93}_{37} Rb + 3(^{1}_{0}n). \tag{6.1}$$

The average total energy released by neutron induced fission in U-235 is around 200 MeV, where the majority of the kinetic energy is carried off by the large fragments. The rest of the energy is carried by neutrons, photons, electrons and neutrinos, emitted either promptly, or as delayed radiation of the decaying fission products. In each fission, the photons will take an average total energy of 7 MeV and 6.3 MeV for the prompt and delayed photons, respectively [75]. The average energy of each photon emitted is 0.97 MeV [76].

The fission processes that occurs within the reactor core results in the radiation field outside the core thus being dominated by thermal neutrons and photons. Just outside the reactor core, the flux of thermal neutrons is 10^7 times higher than the flux of neutrons of 10 keV. The neutron energy spectrum at various distances from the fuel elements can be seen in Appendix F.

In Figure 6.5, the top area of the JEEP II reactor and the pool in which the measurements were performed, can be seen. The external moderating water pool is located several meters on the side of the reactor, and assures that all the neutrons reaching the water pool are being thermalized. To obtain a sufficiently high thermal neutron flux, the detectors had to be lowered down to the level of the reactor core inside an aluminium container. In order to calibrate the response of the detectors in a known thermal neutron flux, the flux was measured with gold activation by the IFE personnel in a common position with the bubble detectors and the TLDs. The gold activation measurements showed a thermal neutron flux of 7230 n.cm$^{-2}s^{-1}$ [77].

6.3 Measurement Procedures

A thorough description of the physics of the detectors and their general mode of operation was made in Chapter 5. This section provides a brief description of the actual detectors used in this work and the measurement routines employed.

6.3.1 Bubble Detectors

The two types of bubble detectors used in this work are the bubble detectors commercially available from BTI, Chalk River, Canada: (1) the spectrometer set used to detect neutrons in several energy intervals; BDS, and (2) the set for detecting thermal neutrons; BDT.

As we have seen, the BDS spectrometer set consists of 36 bubble detectors of six different types with lower neutron energy thresholds of 10, 100,

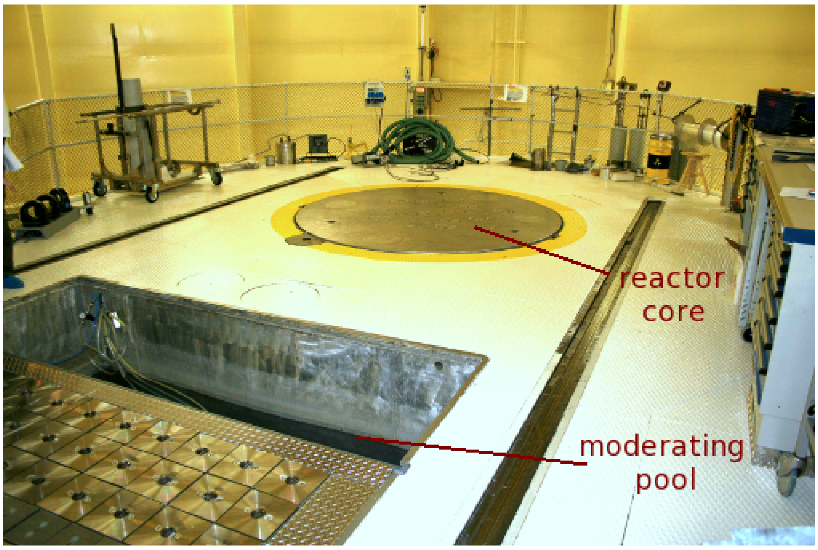

Figure 6.5: The working area is located on top of the research reactor JEEP II. Between the working area and the reactor core are several meters of concrete shielding. On the side of the reactor core is a pool of moderating water. The radiation environment in the pool is dominated by photons and thermal neutrons.

600, 1000, 2500 and 10 000 keV. As suggested by the manufacturer, the spectrometry has been performed using all 6 detectors within one threshold, in order to achieve good statistics in each measurement sequence. With the detectors, follows an unfolding algorithm from BTI, converting the responses into a fluence spectrum with six energy bins. The unfolding procedure is described in Appendix A. To further obtain the neutron dose from the fluence, fluence-to-dose factors listed in Appendix C have been applied.

To stay within the calibration temperature of the detectors during the measurements, all BDS detectors were consistently thermalized in a 20 ± 0.5℃ water bath prior to usage, and further wrapped in insulating Styrofoam. All measurements have been performed within the limited guaranteed optimal time of use (within 3 months after initial usage), and the number of measurements have not exceeded the maximum, recommended number of cycles (10-15 cycles). Detector storage have been according to the recommendation at 4 ℃ in a cooler.

For the thermal neutron measurements, the BDT set of 5 pieces were all utilized. The BDTs have an integrated temperature compensation mechanism, therefore no insulating material were required during these measurements. The BDTs are calibrated and supplied with factors for their response to dose. To obtain the thermal neutron fluence, the fluence-to-dose conversion factors were used.

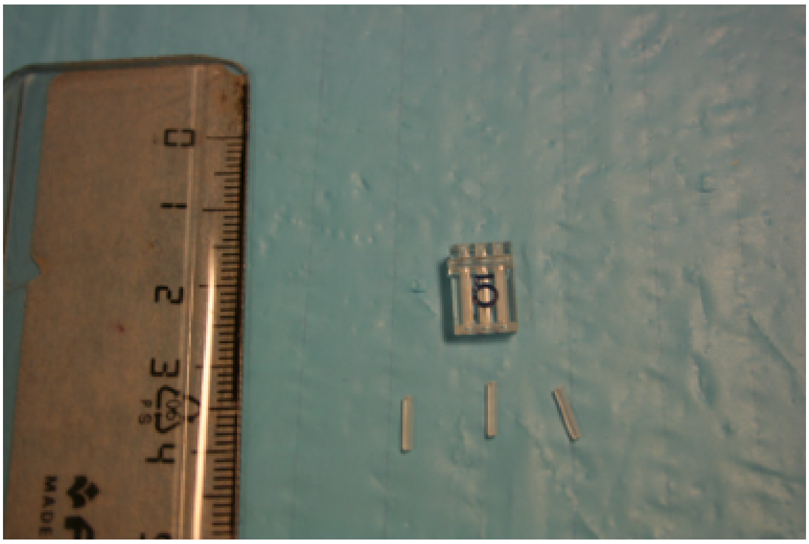

Figure 6.6: Rods of TLD 600 and TLD 700 are placed inside plastic containers for easier handling and for enabling positioning of TLDs in a fixed position during measurements.

The counting of bubbles was performed by the automatic optical scanner; Bubble Detector Reader. According to the manufacturer, the amount of bubbles should not exceed 200-300 bubbles per measurement. This corresponds to equivalent doses on the order of mSv for the BDS detectors and on the order of μSv for the BDT detectors. After each measurement, a re-compression of the bubbles was performed.

6.3.2 Thermoluminescence Detectors

The two types of TLDs used in this work are the LiF:Mg:Ti (Lithium Fluoride with added Magnesium and Titanium) from Harshaw:
(1) TLD-600, enriched with ^{6}Li, is both neutron and photon sensitive, and (2) TLD-700, consists primarily of ^{7}Li, is photon sensitive. Figure 6.6 displays three TLDs along with a plastic container applied for easier handling. Each TLD rod is 1 mm in diameter and 6 mm in length. To gain sufficient statistics and thus reduce the uncertainty, six TLD rods of each type were used during each measurement.

The TLD readout set-up is shown in Figure 6.7. After exposure, the TLDs were read out by the TLD readout unit, in which a photomultiplier records the light yield as each individual TLD is heated gradually up to 300℃. The response is the integrated charge of the glow curve, obtained by using the TLD readout software Winrems. After usage, the TLDs were annealed for 4 hours at 400℃.

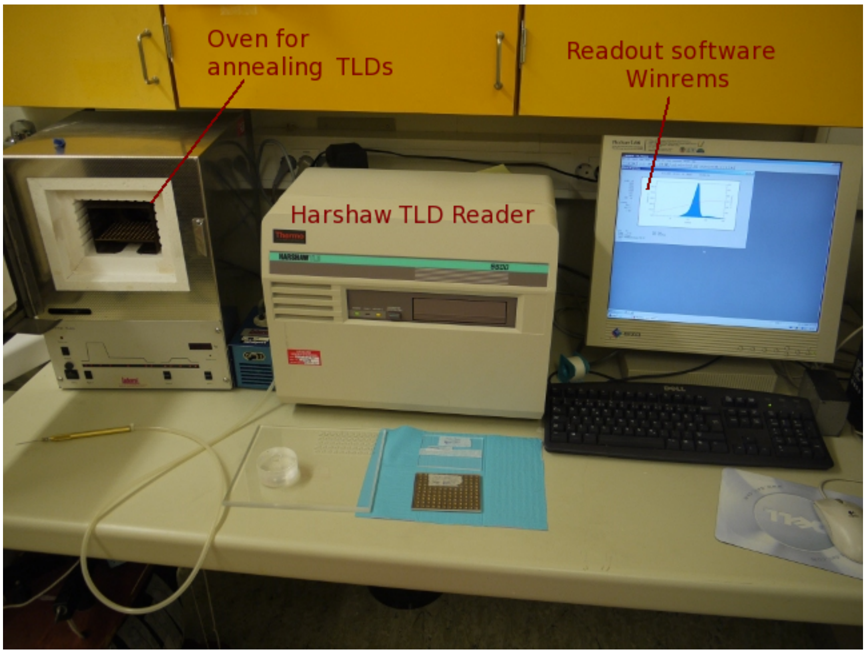

Figure 6.7: TLD readout system: The oven is used for annealing the TLDs. The TLD Reader is connected to a computer with the software Winrems displaying the integrated charge.

Chapter 7

Results and Discussion

The results from the various experiments performed are presented in this chapter. They have been divided into i) investigations of detector performance, ii) calibration issues and iii) the application of the detectors in neutron measurements during radiotherapy.

These experiments were conducted in the field from the medical linac at HUS and in the field of the nuclear reactor at IFE.

7.1 Characteristics of Detectors

The investigations of the detector properties included information on the reproducibility and the linearity of the detectors. In order to obtain a basis for the uncertainty calculations in the measurement data, reproducibility tests were performed. The linearity tests provide information on the detectors' response to different amounts of dose, thus revealing possible limitations with respect to the valid range for dose measurements with the detectors.

7.1.1 Reproducibility

The reproducibility tests of the detectors were performed by exposing the detectors repeatedly under the same conditions in the mixed photon neutron field by using the 15 MV photon beam at HUS. The bubble detectors were positioned 4 cm outside the isocenter of the linac, without any neutron moderating material. The BDS 10 000 was not applied in the experiments, as test measurements with these detectors at HUS did not result in bubble formation.

Due to the limitations in repeated measurements without exhausting the bubble detectors, the measurement sequence was performed three times for each of the six individual detectors within a threshold. The results are presented in Table 7.1. The uncertainties are estimated from the rms values of the response in number of bubbles and varies from 5% to 20%.

Table 7.1: Summary of the reproducibility tests of the bubble detectors.

Detector type	Uncertainty [rms/mean]
BDT	12%
BDS 10	10%
BDS 100	18%
BDS 600	21%
BDS 1000	5%
BDS 2500	10%

The reproducibility tests for the two types of TLDs were performed in-phantom with the TLDs situated 4 cm from the isocenter of the linac. Figure 7.1 displays the results of the reproducibility tests performed with the TLD-600 and the TLD-700, along with Gaussian fits applied. In Table 7.2, the estimated uncertainties of the TLDs are displayed, and range from 2.5% to 5.5%.

Table 7.2: Summary of the reproducibility tests of TLDs.

Detector type	Uncertainty [rms/mean]
TLD-600	2.5%
TLD-700	5.5%

7.1.2 Linearity

According to the manufacturers, the response of each bubble detector is linear within a narrow interval of μSv or mSv, corresponding to a maximum of 200-300 bubbles in each detector. The TLDs are stated to have a quite wide linear range, reaching from 10 μGy - 10 Gy.

Assuming that the restrictions in the valid range of a bubble detector mainly depend on the number of generated bubbles, one type of bubble detector was assumed to be representative for all the bubble detectors. The response to neutron exposures in ten steps yielding amounts up to 350 bubbles is shown in Figure 7.2. The distribution has a non-linear behaviour, indicating a decreasing detector response as the number of bubbles in the detector increase. The calibration factors supplied by the vendor, are obtained during a detector response of approximately 150 bubbles. To enable correct interpretation of the measurement data of the detectors, the number of bubbles generated in each measurement should not exceed the number, i.e. the dose, that the detector was exposed to during the factory calibration, or alternatively the non-linearity must be corrected for. Hence, in the following measurements, the number of bubbles obtained was as far as achievable sustained at 150 bubbles.

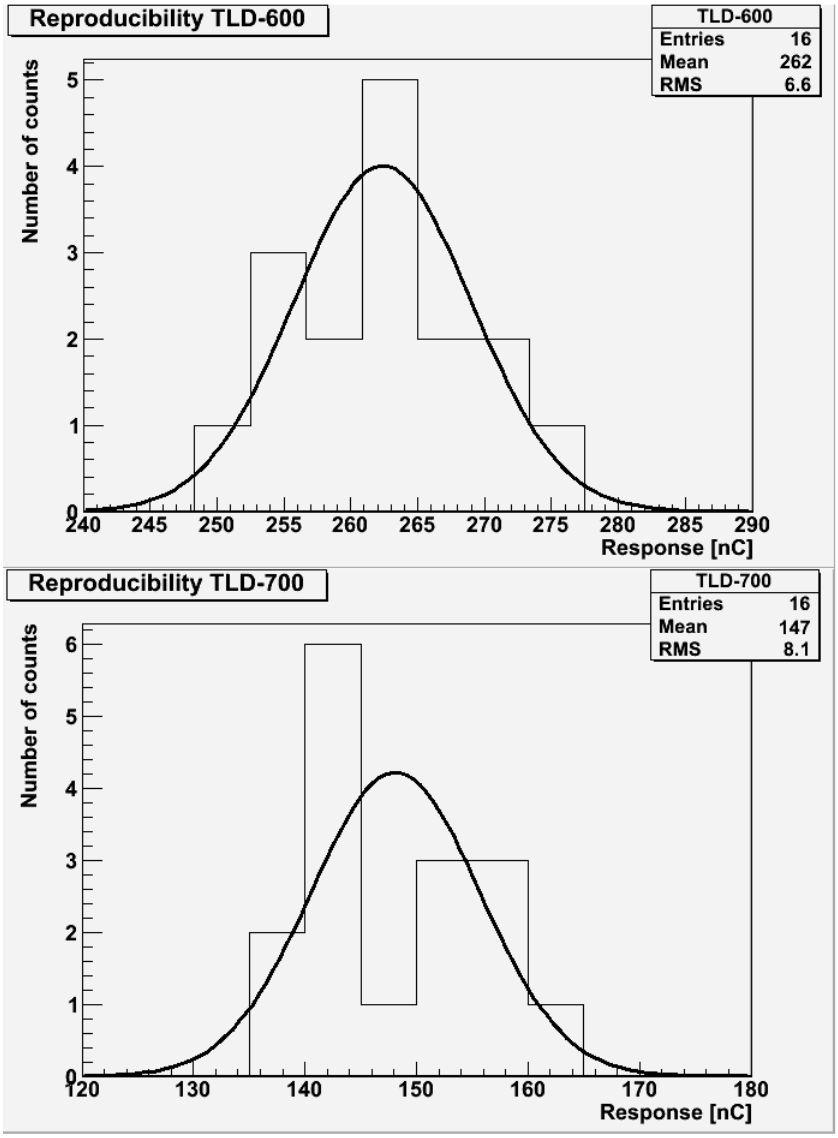

Figure 7.1: Results of the reproducibility tests of the TLD-600 and the TLD-700. Gaussian distributions has been fitted.

Regarding the TLDs, there were two aspects to consider; the relative photon sensitivity of the two types of TLDs and the neutron sensitivity of the TLD-600. The linearity of the photon response was tested with the use of the 6 MV photon beam at HUS, whereas the joint neutron and photon response was examined by using the 15 MV photon beam. Both measurements were performed in-phantom, outside the isocenter of the linac.

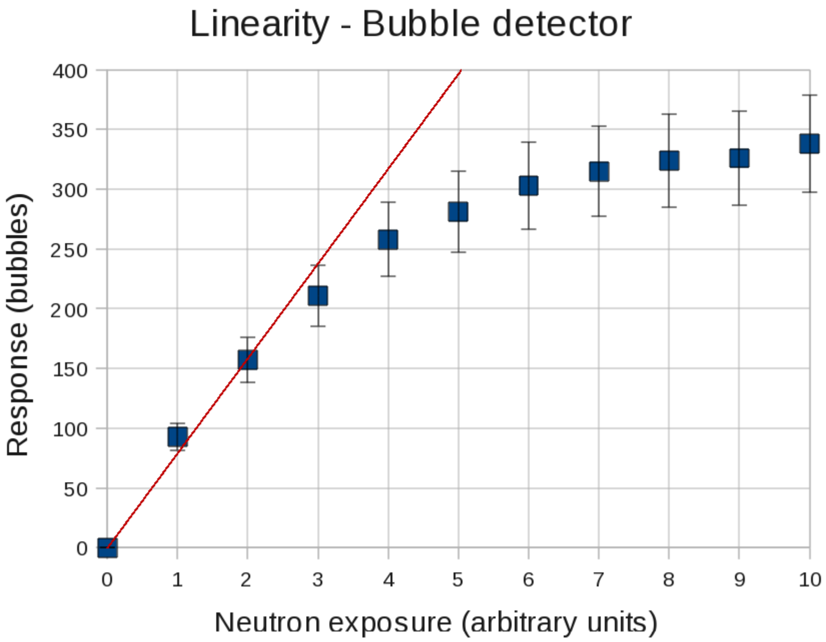

Figure 7.2: Result of the linearity test of the bubble detectors. The solid line shows a linear response approximation based on a calibration of the detector performed at 157 bubbles.

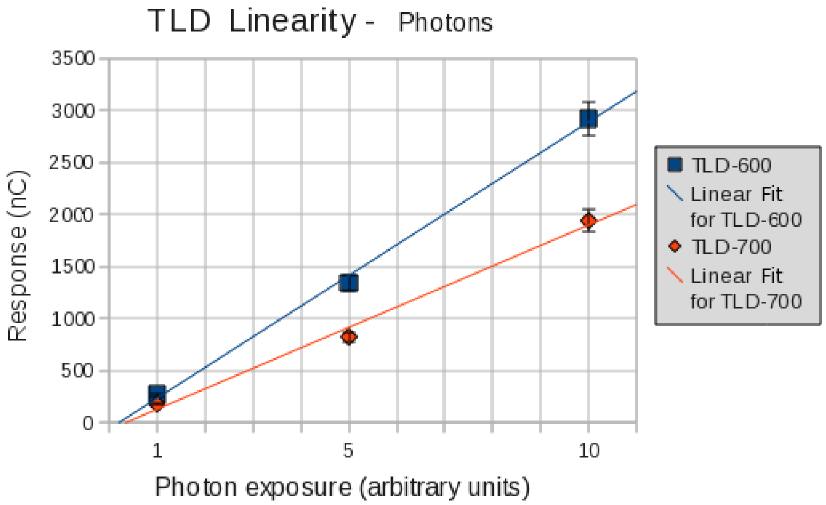

Figure 7.3: Response of the TLDs exposed outside the isocenter of the linac using a 6 MV photon beam. Linear fits have been applied.

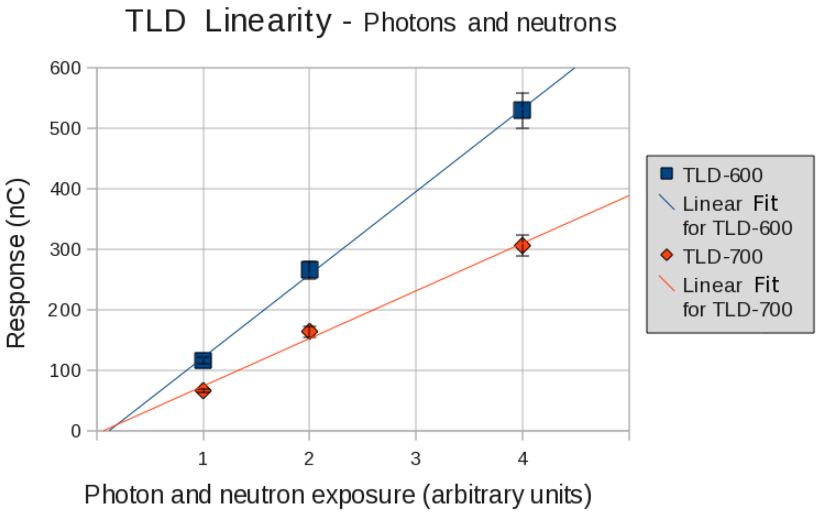

Figure 7.4: Response of the TLDs exposed outside the isocenter of the linac using a 15 MV photon beam. Linear fits have been applied.

The results of the photon exposure, assuming that the neutron production during the 6 MV mode is negligible, are shown in Figure 7.3. The deviations from the linearity in these measurements are less than 5% and 8% for the TLD-600 and TLD-700, respectively. The results of the TLDs exposed to photons and neutrons are shown in Figure 7.4. The deviations from the linearity are in these measurements less than 9% for the TLD-600 and less than 12% for the TLD-700.

7.2 Detector Calibration

In order to calibrate the detectors in a known thermal neutron flux, the detectors were exposed in the mixed photon thermal-neutron field of the nuclear reactor at IFE. The thermal neutron flux in the position of where the measurements were performed was 7230 n.cm$^{-2}s^{-1}$, verified by gold activation measurements carried out by the IFE personnel. All the results from IFE are based on three minutes of exposure in the reactor field. The fluence and dose correspondance is displayed in Table 7.3. For the TLDs; a photon calibration and a neutron cross-calibration were also perfoemed at HUS.

7.2.1 TLD Sensitivity

The TLD neutron calibration is performed in two steps in order to enable unfolding of the neutron response in a mixed photon neutron field.

Table 7.3: Gold activation data.

Fluence [n.cm^{-2}/3min]	Converted equivalent dose [μSv/3min]
1.3×10^{6}	15

(1) The difference in photon response between TLD-600 and TLD-700 was obtained by using the 6 MV photon beam at HUS.
(2) The TLDs were then exposed to the mixed radiation field at IFE, where the thermal neutron flux is known. Based on the measurements in 1), the photon component can be subtracted from the total TLD response.

(1) Difference in photon response

The difference in the photon response of the TLDs was obtained by using the 6 MV photon beam with the detectors situated in the Phantom B. The measurements were performed in several depths of the phantom, at 4, 8 and 12 cm outside the central beam axis. The ratio of photon response obtained was; k=0.66±0.04, where TLD-600 is more sensitive to photons than TLD-700.

(2) Neutron response

The TLDs were exposed for 3, 6, 9 and 12 minutes in the measurements at IFE. The results are presented in Figure 7.5. The charge response in nC is quite high in this field, reaching from 10^3 to 10^4 nC. This is 2-3 times the typical response during the measurements performed at HUS. The TLD-700 measurements indicate a strong photon background. By dividing the TLD-700 response by the correction factor k, the corrected response of TLD-700 is almost on top of the TLD-600 yields. The neutron response is on the order of a couple of percent of the total response, illustrating that the unfolded neutron response is the difference between two large numbers. This makes the photon discrimination in the neutron unfolding process a challenge. The mean of the unfolded neutron responses is 190±200 nC/3min, which corresponds to sensitivities; $(1.5\pm1.5) \times 10^{-4}$ nC/(n.cm^{-2}) and 13±13 nC/μSv. Considering the large theoretical uncertainties obtained in this measurement, these data was not used as a measure of the neutron sensitivity in the following experiments. It is probably a better option to perform a TLD neutron calibration in beam lines with neutrons not exhibiting a large presence of photons resulting from the fission processes. IFE has such neutron beam lines, and these might be well suited for TLD neutron calibration.

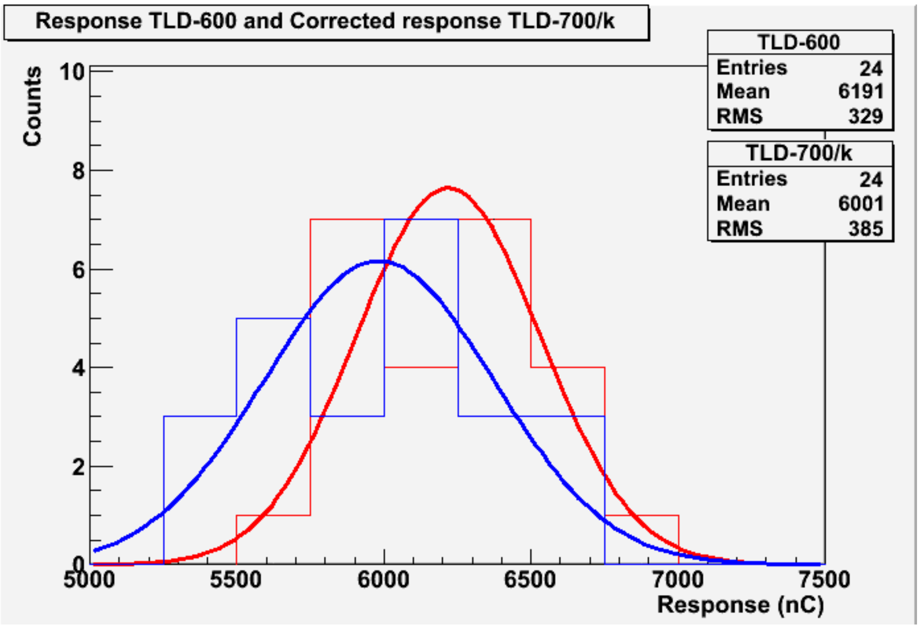

Figure 7.5: Response of the TLD-600 (red) and the corrected response TLD-700/k (blue) in the field of the nuclear reactor at IFE. Gaussian distributions have been fitted.

7.2.2 BDT Sensitivity

The measurements with the full set of BDT detectors were carried out in the same thermal neutron flux as with the residual detectors. The response of the BDTs, in number of bubbles, was converted into dose and fluence as explained in the set-up chapter. The results of the BDT measurements are displayed in Table 7.4, along with the fluence reported by IFE. As for the fluence obtained from the BDT measurements, this is four times higher than the fluence measured by gold activation. The sensitivity of the BDTs are according to these measurements four times higher than reported by the vendor.

Table 7.4: Fluence obtained from measurements with BDTs and by gold activation at IFE. *Converted fluence assuming the calibration factor given by the vendor.

BDT response	BDT fluence*	IFE fluence
150±20 bubbles	$(5.2\pm0.6)\times10^6$ n.cm^{-2}	1.3×10^6 n.cm^{-2}

The measurements at the reactor have revealed a strong photon component: the TLD-700 reading indicates a photon dose rate of 1.2±0.1 Gy/3min based on a calibration in the 6 MV setting at HUS (see Appendix D.1). Measurements at HUS have also revealed that the BDTs are slightly sensitive to intense photon fields. In the 6 MV photon beam the BDT photon sensitivity were found to be 10±1 bubbles/Gy. This rate results in a photon response in the reactor field of the BDTs of 12±2 bubbles/3min. However, this background accounts for less than 10 percent of the total response in the bubble detectors and cannot explain the discrepancy factor of four between the neutron sensitivity retrieved from the calibration at IFE and the sensitivity factors supplied by the vendor. Other possible explanations for this difference can be due to the procedure of obtaining the calibration factors; the manufacturer have calibrated the detectors to neutrons from an Am-Be source.

BDT calibration factor

Considering the deviations obtained in the calibration at IFE, new bubbles to fluence and dose conversion factors were established and are displayed in Table 7.5. These calibration factors will be used in further calculations of BDT fluence and dose.

Table 7.5: BDT fluence and dose sensitivity factors obtained from the IFE calibration.

Fluence Sensitivity [bubbles/n.cm^{-2}]	Equivalent Dose Sensitivity [bubbles/μSv]
$(1.2\pm0.1)\times10^{-4}$	10±1

7.2.3 BDS Sensitivity

Single insulated BDS detectors were exposed for a period of 3 minutes in the reactor field. The BDS detectors have lower neutron energy thresholds above thermal energies. Nevertheless, bubbles were formed. The number of bubbles produced in the detectors corresponds to neutron doses on the order of mSv (Table D.1). The results imply that the BDS detectors are sensitive either to neutrons of energies below the energy thresholds given by the vendor or to the photon component of the field. Measurements performed in the 6 MV photon beam at HUS have reveiled that the BDS detectors are sensitive to intense photon fields. However, equivalent to the BDT detectors, the photon background cannot account for the total amount of bubbles formed in the BDT detectors.

7.2.4 Cross-Calibration Between the TLD and the BDT

A measure of the thermal neutron fluence and the equivalent dose correspondence to the TLD charge response was performed by a cross-calibration with the BDTs at HUS. Both detectors were situated in-phantom, 4 cm from the central beam axis of the 15 MV photon beam. The obtained sensitivity of the TLD-600 to neutrons is shown in Table 7.6. These TLD calibration factors will be used later in the radiotherapy measurements.

Table 7.6: The neutron sensitivity for the TLD-600 obtained by cross calibration with the BDT detectors.

Fluence Sensitivity [nC/(n.cm^{-2})]	Equivalent Dose Sensitivity [nC/μSv]
$(1.1\pm0.5)\times10^{-5}$	1.0 ± 0.4

7.3 Neutron Measurements in Radiotherapy

The results of the in-phantom neutron measurements while applying a 15 MV photon beam are presented in this section. The spatial distribution of the neutrons has been investigated, and a comparison has been made of the neutron yield during the treatment techniques 3D-CRT and IMRT. The results of the detector characteristics and calibrations presented in the two previous sections was taken into account during the following measurements:

The neutron sensitivity of the detectors, or the corresponding fluence and dose are not well defined at this present stage. The main focus of the results introduced here is therefore on relative quantities, preferentially by the use of raw-data. The detectors have here been used within the linear regions presented in the tests of the detector characteristics, and the relative response is therefore expected to be a good measure of the relative neutron contribution.

The measurement data is also presented here as converted into fluence and equivalent dose. The uncertainty estimates obtained for the BDS fluence spectrum reaches from 10-400%, and are mainly due to the error propagation in the spectrum unfolding algorithm.

All the results of the measurements are given in response, fluence or dose per treatment dose in Gy, delivered to the isocenter by the photon beam.

7.3.1 Spatial Neutron Distribution

The spatial distribution of neutrons was measured by applying the TLDs outside the isocenter in the Phantom B. A 5x5 cm^2 fixed photon field configuration was defined by the secondary collimators, and applied from the side in a 90° gantry angle. In the dose plan system Eclipse, the dose distribution was calculated in order to visualize the photon dose on a colour scale.

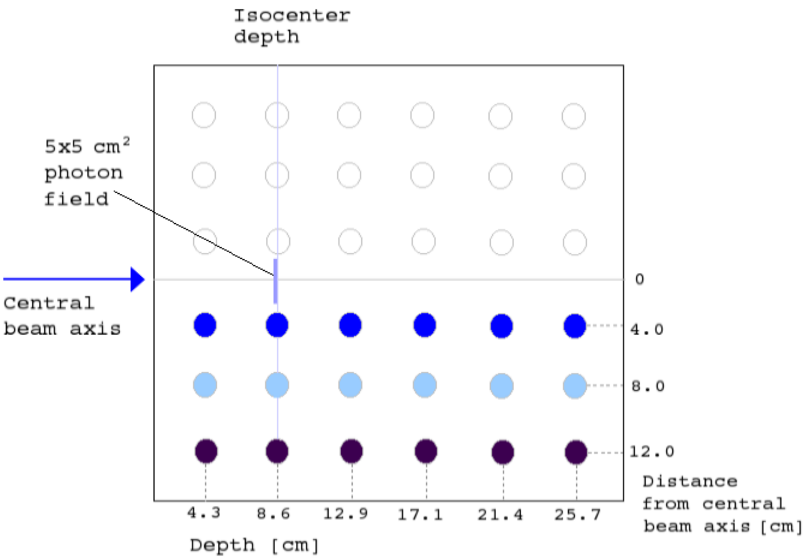

Figure 7.6: Top view of Phantom B. The 18 positions in where TLD measurements were performed are featured. A 5x5 cm^2, 15 MV photon field was applied from a 90° gantry angle.

TLD Measurements

The 18 positions in the phantom where the TLD measurements were performed are featured with colours in Figure 7.6.

Figure 7.7.a displays the unfolded thermal neutron yield from the combined response of the TLD-600 and the TLD-700. The results indicate that the thermal neutrons primarily are distributed in the outer layers of the phantom, located close to the treatment head. These results are in accordance with other similar experiments [1]. Moving into deeper layers, the response have an exponential decrease: From the positions in the outer layer and to the next measurement positions, the response drops off sharply. At the deepest positions measured, the response is approximately ten times lower than in the outer layers.

The spatial distribution of the photons obtained from the TLD-700 measurements are displayed in Figure 7.7.b. As can be seen, the greater part of the dose contribution from photons outside the treatment volume is deposited close outside the photon field. These photons close to the central beam axis are principally scattered photons from the applied photon beam. The response in the positions further away from the central axis of the field, are principally that of photons leaking from the treatment head, and in addition widely scattered photons.

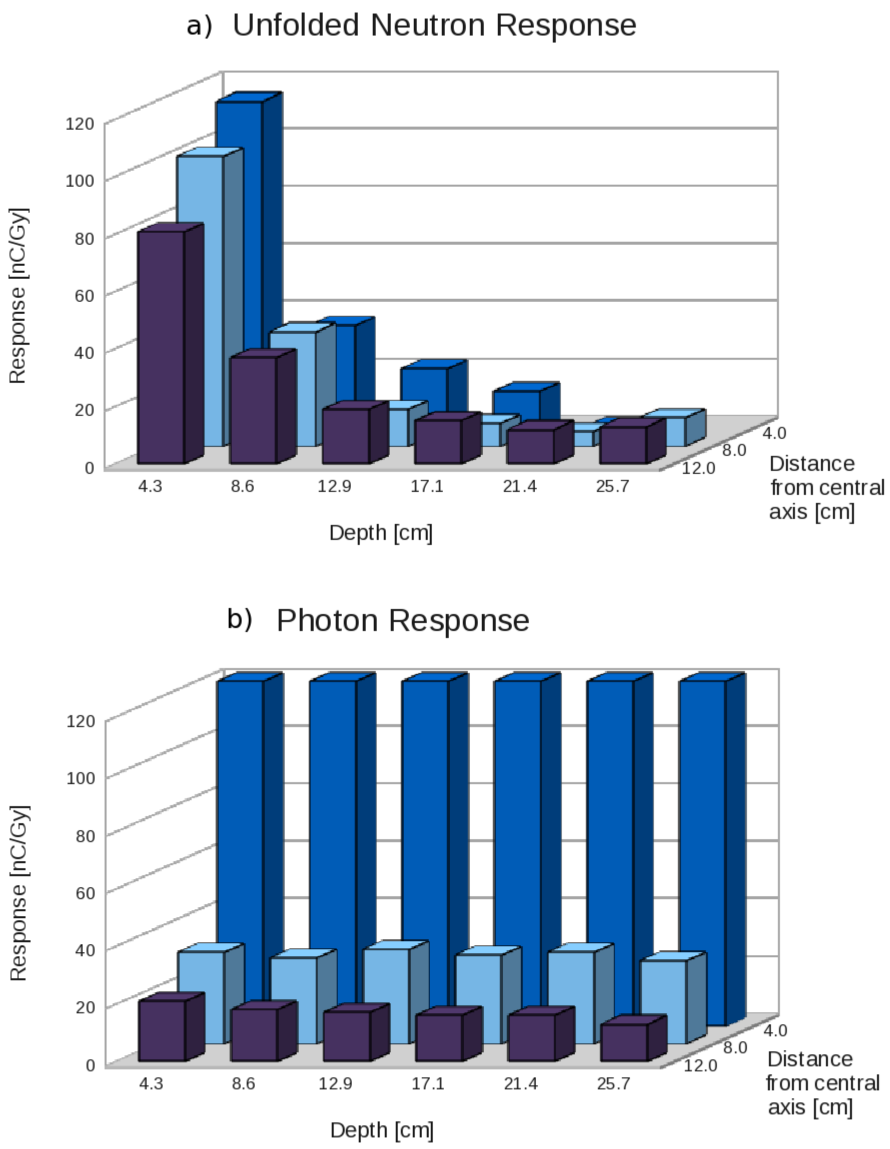

Figure 7.7: Spatial distributions of neutrons and photons in Phantom B measured with TLDs while applying a 5x5 cm^2 15 MV photon beam. The response is given in nC per treatment Gy. a) Thermal neutron response. b) Photon response.

Considering the correlation of the neutron response to the distance from the central beam axis, this is not as significant as for the photon distributions. However, examining the thermal neutron response at 4.3 cm depth in the phantom, the position closest to the central beam axis has a slightly higher neutron response than the positions further off the central beam axis. This feature may be explained by considering the mechanisms of the photoneutron production in the components of the linac head; evaporation and direct knock-out (see Section 2.1.4). The direct knock-out component of the field stands for roughly 10 % of the neutrons produced whilst applying a 15 MV photon field. These neutrons have a forward directed angular distribution and can be a reason for the elevated response closer to the photon beam.

Eclipse Dose Distribution

Figure 7.8 shows the photon dose distribution on a colour scale as calculated in Eclipse. The dose is concentrated along the central beam axis and drops off sharply as the distance from the axis increase. This is in good agreement with the measured TLD-700 distribution.

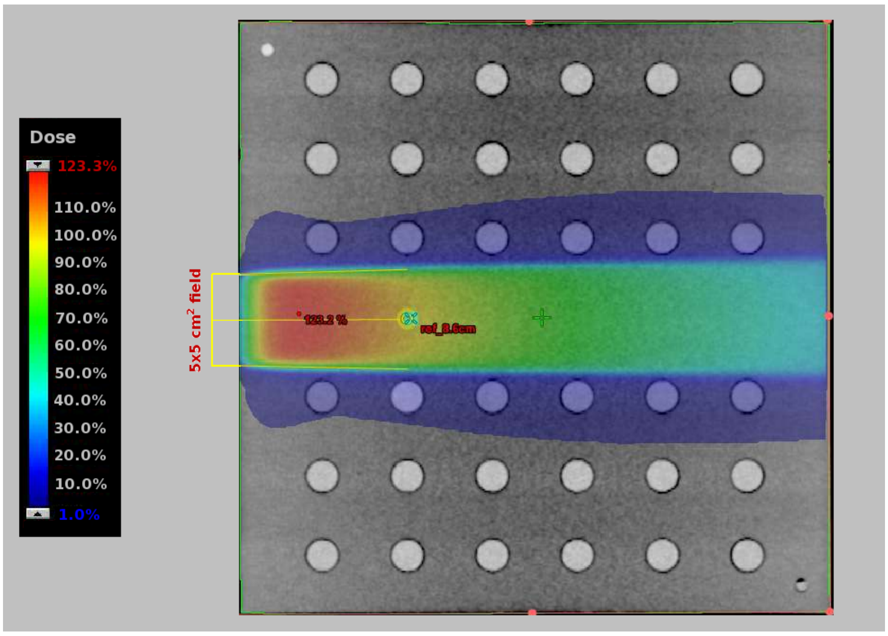

Figure 7.8: Dose distribution in Phantom B from a fixed 5x5 cm^2 15 MV photon beam calculated in Eclipse.

Fluence and dose

According to the cross calibration with the BDTs, the thermal neutron response in the positions measured corresponds to fluences and doses on the order of $10^6 - 10^7$ n.cm^{-2}/Gy and 10-100 μSv/Gy, respectively.

7.3.2 Neutron Yields in Different Treatment Techniques

The target volume and critical organ was defined in the Phantom A, as described in Figure 6.4 in the set-up. In the dose plan system Eclipse, the treatment techniques 3D-CRT and IMRT were applied the same conditions; three beam angles and a realistic total treatment dose of 70 Gy was assigned to the target volume. In the case of the IMRT treatment, the dose plan system calculated the beam delivery based on the optimized dose distribution out from the dose restrictions to the critical organ. To deliver the treatment dose to the target volume under such conditions, a different number of MUs was required for the two treatment modalities.

The dose optimization was performed in both configurations and the results of the two calculated distributions are displayed in Figure 7.9. As can be seen, the neutron measurements have been performed outside the 1% dose level indicated by the colour scale. The IMRT plan was able to restrict the dose exposure to the critical organ to 53% of the dose received by the target volume. During the 3D-CRT plan that was designed, the critical organ receives 72% of the target volume dose as listed in Table 7.7. In this dose calculation, the IMRT plan required 365 MU/Gy; 2.6 times more MUs than the 141 MU/Gy, required in the 3D-CRT plan. However, it is quite common that the IMRT dose plans exceed 3-4 times the MUs required for a 3D-CRT treatment.

Table 7.7: Summary of the 3D-CRT and IMRT dose plans.

	3D-CRT	IMRT
Total dose to target volume	70 Gy	70 Gy
Dose to critical organ	72%	53%
Number of MUs per treatment Gy	141	365

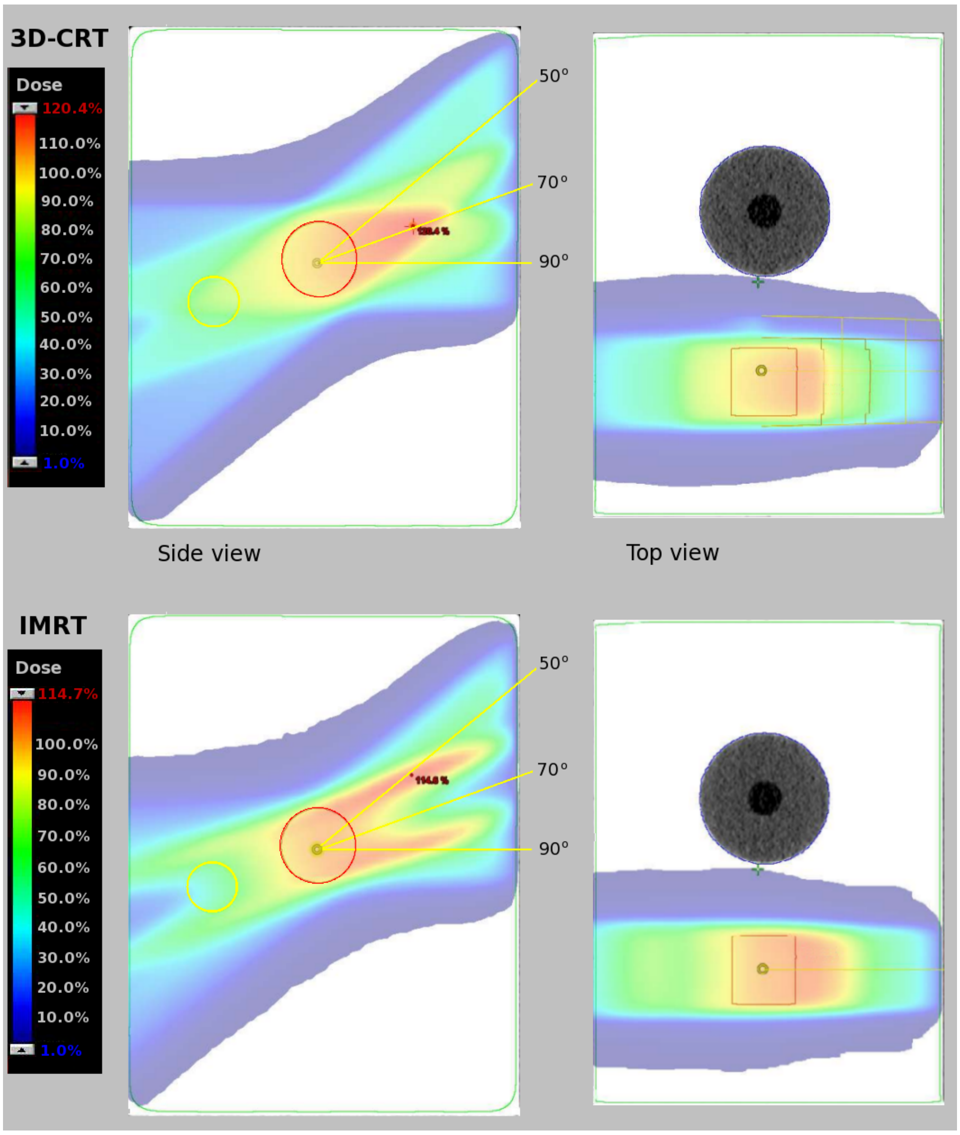

Figure 7.9: Eclipse dose calculation for the 3D-CRT and the IMRT plan. The, yellow, small circle indicates the critical organ. The red, large circle is the target volume. The dose level is indicated by the colour scale, with lower dose level of 1%. In the images on the right hand side, the insulating material in where the detectors are positioned during the measurements are visible outside the 1% dose level.

TLD and BDS Response

The treatment plans were executed while performing in-phantom measurements with both the TLD and the BDS detectors. The treatments were delivered in dose fractions of 2-12 Gy, and the results are displayed as the response in nC/Gy and bubbles/Gy in Tables 7.8 and 7.9, respectively. The IMRT/3D-CRT neutron ratios are applied in the tables to enable a comparison; The TLD neutron response is 2.6 times higher during the IMRT treatment than during the 3D-CRT plan. The BDS responses are 2.3-2.7 times higher in the IMRT measurements. The results obtained indicate that the neutron yield from the linac is correlated to the number of MUs. This is in agreement with previous studies [4, 45].

Table 7.8: Summary of the TLD thermal neutron response during the 3D-CRT and IMRT treatment techniques.

	Response 3D-CRT [nC/Gy]	Response IMRT [nC/Gy]	IMRT/3D-CRT
TLD	180±20	480±40	2.6±0.2

Table 7.9: Summary of the BDS neutron response during the 3D-CRT and IMRT treatment techniques.

	Response 3D-CRT [bubbles/Gy]	Response IMRT [bubbles/Gy]	IMRT/3D-CRT
BDS 10	170±20	390±40	2.3±0.3
BDS 100	110±20	290±30	2.7±0.7
BDS 600	90±20	210±40	2.4±0.7
BDS 1000	26±1	61±3	2.3±0.2
BDS 2500	12±1	30±3	2.5±0.3
Mean	-	-	2.5±0.5

Fluence and Dose

The results of the 3D-CRT and IMRT measurements converted into fluence and dose are displayed in Table 7.10. As can be seen, the fluence of the thermal part of the spectrum is significant in both treatment modalities, considering the TLD fluence contribution. The ratios between the 3D-CRT and IMRT dose plan measurements are roughly the same as the ratio of 2.6 obtained from the raw-data, except for the BDS fluence where the factor is 1.9.

Table 7.10: Fluence and dose during the 3D-CRT and IMRT treatment techniques.

Results per treatment Gy	3D-CRT	IMRT
TLD Fluence [n.cm^{-2}]	$(1.6 \pm 0.6) \times 10^7$	$(4.4 \pm 2.0) \times 10^7$
BDS Fluence [n.cm^{-2}]	$(2.2 \pm 1.4) \times 10^7$	$(4.2 \pm 3.6) \times 10^7$
TLD Equivalent Dose [mSv]	0.18±0.07	0.48±0.20
BDS Equivalent Dose [mSv]	2.3±1.5	5.6±4.8

The results of the unfolded spectrum fluences are displayed in Figure 7.10.a. Due to the error propagation in the unfolding process, the uncertainties are large. Particularly the lower segments of the energy spectrum are affected. The IMRT/3D-CRT ratios in the BDS fluence results, varies from 1.7 to 5.3 for these data.

The BDS results converted into equivalent doses divided into regions of five energy intervals are displayed in Figure 7.10.b. Detailed data on fluence and dose in each energy interval of the spectrum can be retrieved in Appendix D.

In Figure 7.11, the fluence and equivalent dose results are presented in percentage. Considering the fluence in 7.11.a, two energy intervals are prominent. The first and the most dominant is in the lower energy intervals containing thermal neutrons and energies reaching from 10 to 100 keV. These bins comprise together about 85% of the neutron fluence in both the 3D-CRT and the IMRT dose plan. The second interval to be noticed is the energy bin reaching from 600-1000 keV, containing approximately 10% of the neutron fluence. These features have resemblances with spectra observed in similar experiments performed with linacs [2]: Two characteristic features; the low-energy distribution from the neutron evaporation processes and the direct knock-out neutrons at higher energies.

The percentage dose distribution is presented in 7.11.b. The representation illustrates that the main dose contribution is an effect of the neutrons in the higher energy bins, even though the fluence from these bins are not the most prominent. The neutrons in the energy interval reaching from 600 to 1000 keV has a high biological effect and results in being the main contributor to the neutron equivalent dose; around 50%.

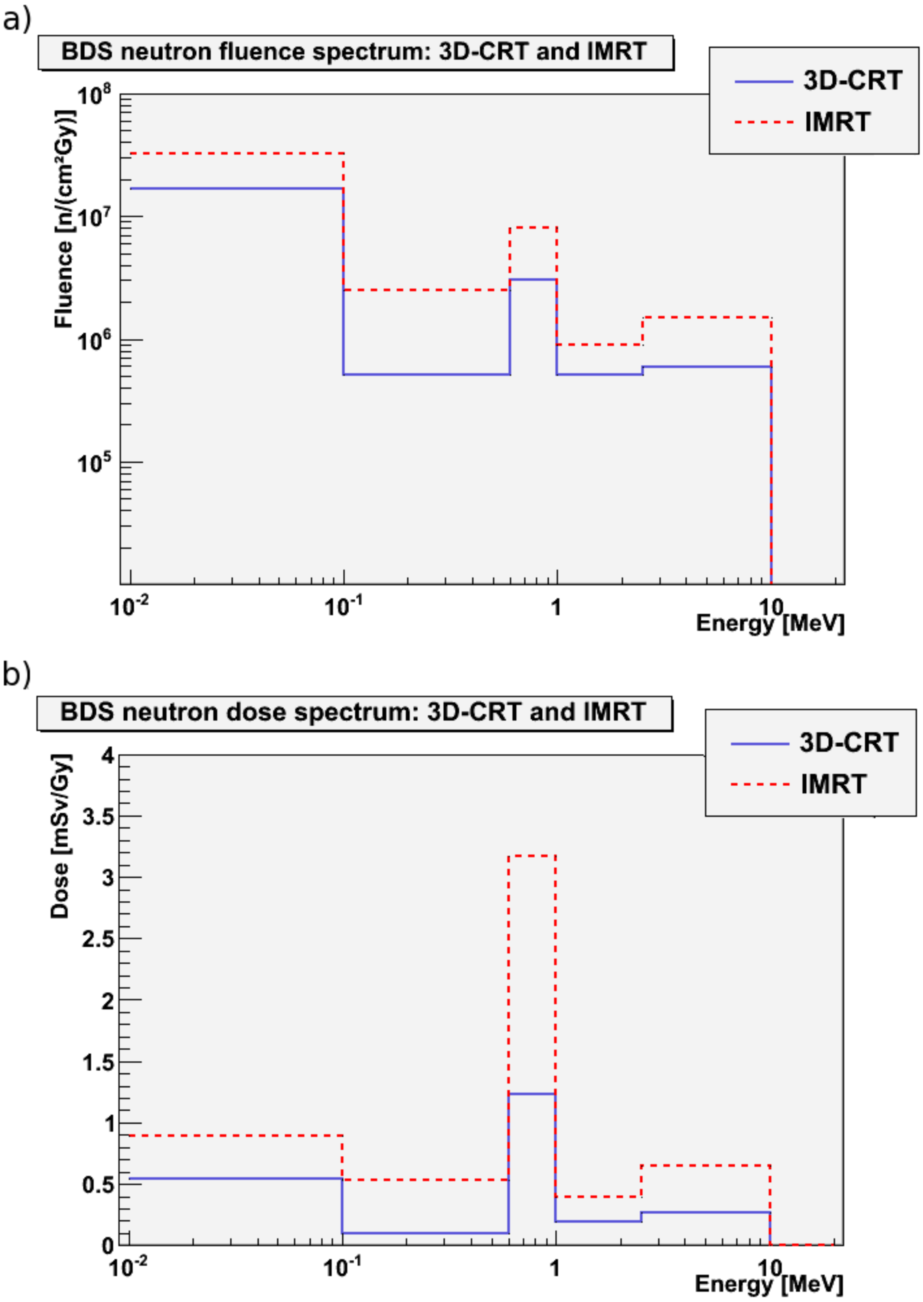

Figure 7.10: a) Neutron fluence and b) neutron equivalent dose within regions of five energy intervals during the 3D-CRT and the IMRT dose plans.

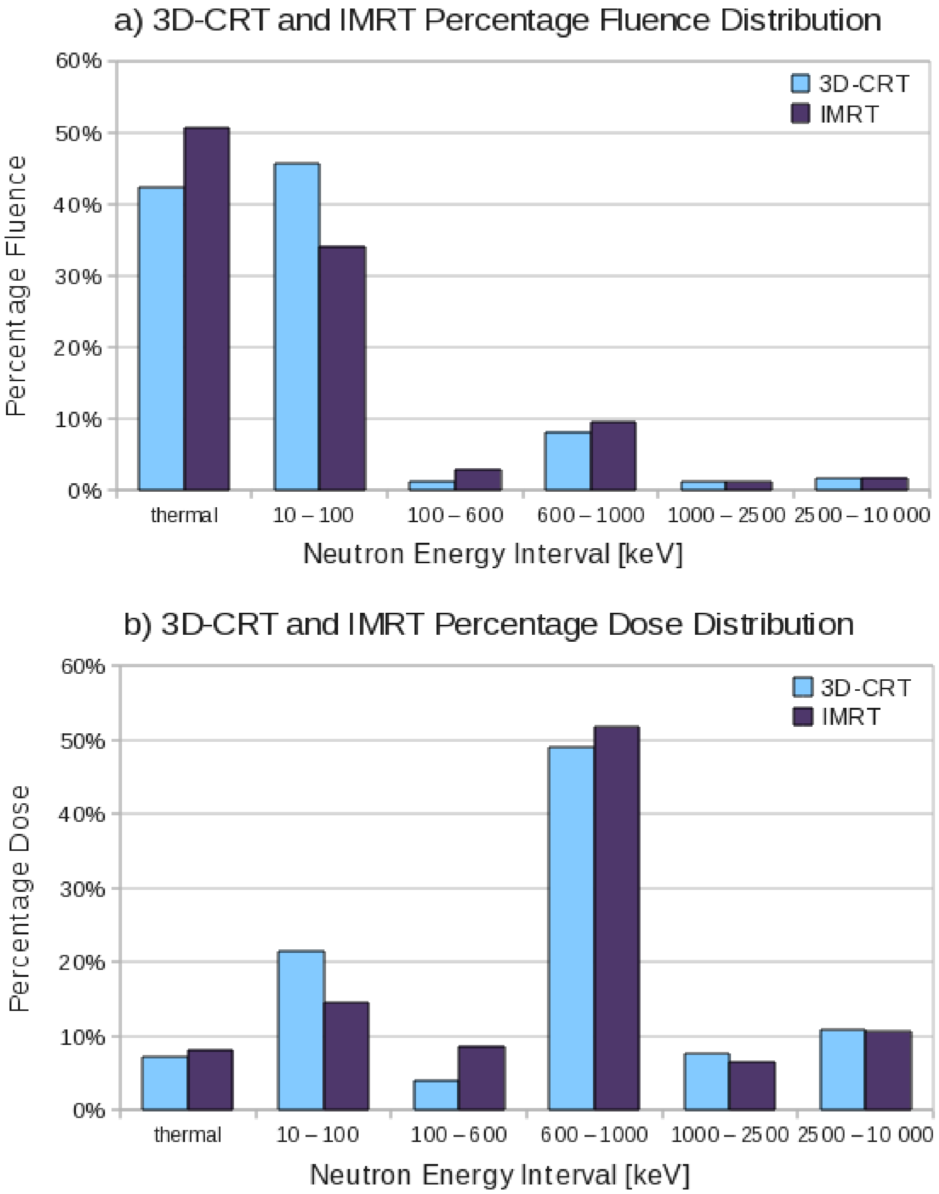

Figure 7.11: Percentage distributions of a) neutron fluence and b) neutron equivalent dose in five intervals of the energy spectrum during the 3D-CRT and the IMRT treatment plans. The lower thermal energy bin is obtained from TLD measurements, and the bins from 10 keV and up are from the BDS measurements.

In Table 7.11, a summary of the neutron fluence and dose results from the two treatment techniques is given. As can be seen, both the fluence and the dose during the IMRT measurements exceeds the results from the 3D-CRT measurements, and scales roughly as the number of MUs. The neutron dose per MU maintains approximately the same during both treatments. The result of the total dose contribution from neutrons for the entire treatment of 70 Gy is 0.2±0.1 Sv and 0.4±0.3 Sv for 3D-CRT and IMRT, respectively. The doses and fluences obtained in these measurements are on the same order of magnitude as found in similar experiments [47–49].

The mean neutron energy obtained is 0.24±0.15 MeV during the 3D-CRT plan and 0.25±0.22 MeV in the IMRT plan. Average energies during IMRT treatments have in the literature been reported to exceed the average energy in 3D-CRT treatments by a few percent [4].

Table 7.11: Summary of fluence and dose results in the 3D-CRT and IMRT dose plans.

	3D-CRT	IMRT
Total treatment dose [Gy]	70	70
Monitor Units/Gy [MU/Gy]	141	365
Mean neutron energy [MeV]	0.24±0.15	0.25±0.22
Neutron fluence/Gy [n.cm^{-2}/Gy]	$(3.8 \pm 1.5) \times 10^7$	$(8.6 \pm 4.1) \times 10^7$
Equivalent Dose/Gy [mSv/Gy]	2.5±1.5	6.1±4.8
Equivalent Dose/MU [μSv]	18±11	17±13
Total Equivalent Dose [Sv] during a 70 Gy treatment	0.2±0.1	0.4±0.3

Chapter 8

Conclusion and Outlook

The focus of this thesis has been on two main objectives. The first objective included investigations of the properties of the detectors used, and the second was applying these detectors in neutron measurements during radiotherapy with a 15 MV photon Varian iX medical linac used for cancer treatment at HUS.

Two types of bubble detectors were used; the BDS threshold detectors intended for neutron spectrometry, and the BDT detectors made for thermal neutron detection. Pairs of TLDs were also applied; the TLD-700, sensitive to photons, and the TLD-600, sensitive to photons and thermal neutrons.

The investigations of detector characteristics included reproducibility of the detectors and linearity tests. The reproducibility of the detector responses were found to be from 5% to 21% for the bubble detectors, and 2.5% to 5.5% for the TLDs. The linearity tests revealed a non-linear response for the bubble detectors, with increasing deviation from the linearity in responses above 200-250 bubbles. To enable use of the calibration sheets from the vendor, the number of bubbles obtained in the following measurements were held as near as possible to the number of bubbles obtained during the calibration.

The detectors were applied in the mixed photon thermal-neutron field of the nuclear reactor at IFE in order to perform calibration of the detectors in a known thermal neutron flux. The neutron energy sensitivity thresholds of the BDS detectors are above that of thermal energies, with the lower threshold detector starting at 10 keV. Nevertheless, bubbles were formed in all the BDS detectors. The reason for this is not fully understood.

The obtained sensitivity was 1.2×10^{-4} bubbles/(n.cm^{-2}) for the BDT detectors, a factor of four times higher than using the calibration factors supplied by the vendor. The response of the TLD measurements at IFE was dominated by the photon component of the signal. The unfolded neutron response obtained after subtracting the photon component of the response was not more than a couple of percent of the total TLD signal. For measurements where the aim is to calibrate detectors with respect to neutrons, a mixed field environment commands that the detector applied must demonstrate a reliable photon discrimination functionality. It is probably a better option to perform a TLD neutron calibration in beam lines with neutrons not exhibiting a large presence of photons resulting from the fission processes.

A measure of the thermal neutron sensitivity was obtained by an in-phantom cross-calibration using the 15 MV photon beam at HUS. The neutron sensitivity of the TLDs after subtracting the photon component of the signal was found to be $(1.1 \pm 0.5) \times 10^{-5}$ nC/(n.cm^{-2}).

The second objective incorporated in-phantom measurements of the undesirable photoneutron contribution outside the target volume while applying a 15 MV photon beam used for radiotherapy at HUS. Two types of experiments were performed: Measurements of the spatial neutron distribution were done and a comparison of the two radiation treatment techniques; 3D-CRT and IMRT was made. In this part of the work the emphasis has been on the relative differences between the neutron responses, preferentially by the use of raw-data, i.e. the number of bubbles and charge response in nC, uncorrelated to fluence and dose, as the correlation between the detector response and the quantities of neutron fluence and equivalent dose was not well defined. Especially the BDS energy threshold sensitivities need further investigation.

Measurements of the spatial distribution of neutrons (and photons) were performed with TLD pairs situated in multiple positions in a solid state phantom. The phantom was applied a photon beam shaped by the secondary collimators into a 5x5 cm^2 field configuration. The photon sensitive TLD-700, mainly detected the scattered photons depositing dose close outside the primary photon field along the central beam axis. These results were in good agreement with the photon dose distribution calculated by the dose plan system Eclipse. The majority of the neutrons were detected in the outer layers of the phantom, and drops off exponentially as phantom depth increases. The outer layer positions are located close to the linac head of where the neutrons are produced.

By use of the dose plan system Eclipse, 3D-CRT and IMRT dose plans were created on a solid state phantom in order to investigate the difference in the neutron production between the two treatment techniques. The measurements were performed with TLD and BDS detectors positioned 7 centimetres away from the central beam axis of the field, at 7 centimetres depth in the phantom.

The IMRT dose plan produced a higher neutron yield than the 3D-CRT dose plan. The ratio between the neutron yield measured when delivering the IMRT dose plan and the neutron yield measured when delivering the 3D-CRT dose plan was found to be 2.6 ± 0.2 measured with the TLDs, and

2.5±0.5, measured with the BDS detectors. This ratio equals the ratio in MUs between the two treatment plans, calculated by the Eclipse dose plan system; the IMRT dose plan required 2.6 times as many MUs as the 3D-CRT dose plan. This is in agreement with results from other experiments.

The results for the two treatment techniques converted into fluences was on the order of 10^7 n.cm^{-2}/Gy and the dose was on the order of mSv. For a full treatment of 70 Gy, this corresponds to an additional neutron dose of 0.2±0.1 Sv for the 3D-CRT plan, and 0.4±0.3 Sv for the IMRT plan.

The mean energy in the neutron spectrum measured while delivering the dose plans was found to be 0.24±0.15 MeV for the 3D-CRT plan and 0.25±0.22 MeV for the IMRT plan. Two characteristic features of the neutron energy spectrum were observed in both the IMRT and the 3D-CRT measurements; the low-energy distribution from the neutron evaporation processes and the direct knock-out neutrons at higher energies.

To enable an accurate conversion of the neutron response into dosimetric quantities, future work should include further investigations of the correlation of the response to the fluence and to the dose.

The sensitivity of the BDS detectors to neutron energies outside their sensitivity range should be examined systematically, and the potential sensitivity to other particles, especially photons, should be looked into.

In order to perform an absolute calibration of the TLDs, the detectors should preferably be exposed to thermal neutrons in a photon free field. The photon response of the two types should also be further examined, as well as their energy dependence and potential effects perturbing the photon discrimination.

When unfolding the fluence spectrum of the BDS detectors there is inherent an error propagation that induces quite large theoretical uncertainties. To reduce the uncertainties due to the error accumulation, improved reproducibility are preferred. The reproducibility obtained for the TLDs are superior to that of the bubble detectors, and the TLDs can be applied as an alternative in neutron energy threshold measurements. It is suggested that future neutron measurements around medical linacs can be performed with the TLDs, and possibly with moderators applied in order to obtain information on the neutron energy spectrum.

Future work concerning neutron contributions outside a target volume may also include neutron doses during particle therapy.

Bibliography

[1] N. M. Spyrou J. B. Awotwi-Pratt. Measurements of Photoneutrons in the Output of 15 MV Varian Clinac 2100C LINAC Using Bubble Detectors. *Journal of Radioanalytical and Nuclear Chemistry*, 271(3):679–684, 2007.

[2] V. M. Hernandez-Davila A. Ortiz-Hernandez H. R. Vega-Carrillo, B. Hernandez-Almaraz. Neutron spectrum and doses in a 18 MV LINAC. *J. Radioanal Nucl. Chem*, 2009.

[3] H. Paganetti G. Xu, B. Bednarz. A review of dosimetry studies on external-beam radiation treatment with respect to second cancer induction. *Phys. Med. Biol.*, 53:193–241, 2008.

[4] M. S. Ferenci R. M. Howell. Investigation of secondary neutron dose for 18 MV dynamic MLC IMRT delivery. *Med. Phys.*, 32(3), March 2005.

[5] A. J. Peurrung. Recent developments in neutron detection. *Nuclear Instruments and Methods in Physics Research Section A: Accelerators, Spectrometers, Detectors and Associated Equipment*, 443(2-3):400 – 415, 2000.

[6] K. Ytre-Hauge. Measurements of Neutron Doses from Radiotherapy with ^{12}C Ions and Photons. Master's thesis, University of Bergen, Norway, May 2009.

[7] D. Schulz-Ertner et al. Results of carbon ion radiotherapy in 152 patients. *Radiat. Oncol. Biol. Phys.*, 58:631–640, 2004.

[8] W. M. Yao et al. (Particle Data Group). J. Phys. G 33, 1, (2006) and 2007 partial update for the 2008 edition.

[9] G.F. Knoll. *Radiation Detection and Measurement.* John Wiley and Sons Inc, 2000.

[10] A. Garcia E. M. Henley. *Subatomic Physics.* World Scientific Publishing Co. Rte. Ltd., 2007.

[11] NCRP National Council on Radiation Protection and Measurements. Neutron contamination from medical electron accelerators. Technical report, No. 79, 1995.

[12] J.E. Turner. *Atoms, Radiation, and Radiation Protection.* WILEY-VCH Verlag, Weinheim, 2007.

[13] A. Zanini, et al. Neutron spectra in a tissue equivalent phantom during photon radiotherapy treatment by LINACS. *Radiat Prot Dosimetry*, 110(1-4):157–160, 2004.

[14] W.R. Leo. *Techniques for Nuclear and Particle Physics Experiments.* Springer Verlag, 1994.

[15] E. C. Finch C. F. G. Delaney. *Radiation Detectors.* Oxford Science Publications, 1992.

[16] P. Rinard. Neutron interactions with matter. In N. Ensslin D. Reilly and H. Smith Jr., editors, *Passive Nondestructive Assay of Nuclear Materials*, pages 357–377. 1991.

[17] J. Neufeld W. S. Snyder. Calculated Depth Dose Curves in Tissue for Broad Beams of Fast Neutrons. *Br J Radiol*, 28(331):342–350, 1955.

[18] International Commission of Radiological Protection. 1990 Recommendations. ICRP Publication 60. Annals of ICRP, Pergamon Press, 1991.

[19] International Commission of Radiation Units and Measurements. Quantities and units in radiation protection dosimetry. ICRU Publication 51., 1993.

[20] A. J. Giaccia E. J. Hall. *Radiobiology for the Radiologist.* Lipincott Williams and Wilkins, 2006.

[21] G. Kraft. Tumor therapy with heavy charged particles. *Progress in Particle and Nuclear Physics*, 45:473–544, 2000.

[22] R. R. Wilson. Radiological use of fast protons. *Radiology*, 47:487–491, 1946.

[23] Radiation Oncology at the UAB Comprehensive Cancer Center. History of radiation oncology. World Wide Web electronic publication, 2003.

[24] F. M. Khan. *The Physics of Radiation Therapy.* Lippincott, Williams and Wilkins, 1994.

[25] E. Tanabe C. J. Karzmark, C. S. Nunan. *Medical Electron Accelerators.* McGraw-Hill, Inc., 1993.

[26] Lecture 'Stråling og Terapi' Universtity of Bergen. O. H. Odland, Oct 2008.

[27] Particle Therapy Co-Operative Group (PTCOG). Statistics of patients treated in hadron therapy centers worldwide: http://ptcog.web.psi.ch, 30/8/2009.

[28] H. Tsujii et al. Overview of clinical experiences on carbon ion radiotherapy at NIRS. *Radiotherapy and Oncology*, 73(2):41–49, December 2004.

[29] National Institute of Radiological Sciences. Reasearch Center for Charged Particle Therapy,www.nirs.go.jp, 29/8/2009.

[30] J. Sisterson. Ion beam therapy in 2004. *Nuclear Instruments and Methods in Physics Research*, B(241):713–716, 2005.

[31] G. Kraft. Tumor therapy with heavy ions. *Verein zur Frderung der Tumortherapie mit schweren Ionen e.V., Darmstadt, Germany, www.gsi.de/informationen/verein-tuthe/*, May 2007.

[32] G. Kraft M. Scholz U. Bechthold. Tumor therapy and track structure. *Radiat Environ Biophys*, 38:229–237, 1999.

[33] A primer on heavy ion physics, GSI internal presentation, Darmstadt, Germany. Prof. Dr. M. Durante, 12/8/2008.

[34] Activity of the biophysics group in the future FAIR facility, GSI presentation. Prof. Dr. M. Durante, FAIR monthly, GSI, Germany, 19/5/2009.

[35] G. Kraft U. Amaldi. Recent applications of synchrotrons in cancer therapy with carbon ions. *Europhysics news*, 36(4):114–118, 2005.

[36] H. Tsujii D. Schulz-Ertner. Particle Radition Therapy Using Proton and Heavier Ion Beams. *Journal of Clinical Oncology*, 25(8), 2007.

[37] D. Schardt R. S. Simon K. Gunzert-Marx, H. Iwase. Secondary Beam Fragments Produced by 200 MeV/u ^{12}C Ions in Water and their Dose Contributions in Carbon Ion Radiotherapy. *New Journal of Physics*, 10, 2008.

[38] Universitats Klinikum Heidelberg. Heidelberg Ion-Beam Therapy Center (HIT): http://www.klinikum.uni-heidelberg.de, 30/8/2009.

[39] P. J. Bostrom and M. S. Soloway. Secondary cancer after radiotherapy for prostate cancer: Should we be more aware of the risk? *European Urology*, 52(4):973 – 982, 2007.

[40] N.M. Spyrou A. Alfuraih, M. P. W. Chin. Measurements of the photonuclear neutron yield of 15 MV medical accelerator. *Journal of Radioanalytical and Nuclear Chemistry*, 278(3), 2008.

[41] S. Kry, M. Salehpour, D. Followill, M. Stovall, D. Kuban, A. White, and I. Rosen. Risk assessment of secondary malignancies from imrt treatments. *International Journal of Radiation Oncology*Biology*Physics*, 60(Supplement 1):S354 – S355, 2004.

[42] A. Alghamdi A. Alfuraih N. M. Spyrou A. Ma, J. Awotwi-Pratt. Monte Carlo study of the photoneutron production in the Varian Clinac 2100C linac. *Journal of Radioanalytical and Nuclear Chemistry*, 276(1), 2007.

[43] D.S. Followill M. Stovall D. A. Kuban R. A. White I. I. Rosen S.F. Kry, M. Salehpour. The calculated risk of fatal secondary malignancies from intensity-modulated radiation therapy. *Int J Radiat Oncol Biol Phys*, 62(4):1195–203, 2005.

[44] S. Breen S. Huang M. Van Prooijen J. Ringash L. Fenkell, I. Kaminsky. Dosimetric comparison of imrt vs. 3d conformal radiotherapy in the treatment of cancer of the cervical esophagus. *Radiotherapy and Oncology*, 89(3):287 – 291, 2008.

[45] T. Wiezorek et al. Experimental Determination of Peripheral Doses for Different Techniques Delivered by a Siemens Linear Accelerator. *Strahlentherapie und Onkologie*, 184:73–79, 2008.

[46] Radiation Dosimetry and Safety. *Calculations of photoneutrons from Varian Clinac Accelerators and their transmissions in materials.* J. C. Liu, K. R. Kase, X. S. Mao, W. R. Nelson, J. H. Kleck, S. Johnson, March 1997.

[47] A. Zanini et al. Monte Carlo simulation of the photoneutron field in linac radiotherapy treatments with different collimation systems. *Phys. Med. Biol.*, 49:571–582, January 2004.

[48] C. C. Lin J. P. Lin, W. C. Liu. Investigation of photoneutron dose equivalent from high-energy photons in radiotherapy. *Radiation Protection Dosimetry*, 133(3):130–135, March 2009.

[49] O. A. Yasin C. Tuniz F. I. Habbani M. K. Saeed, O. Moustafa1. Doses to patients from photoneutrons emitted in a medical linear accelerator. *Radiation Protection Dosimetry*, 133(3):130–135, March 2009.

[50] P-U. Renberg A. V. Prokofieva, A. N. Smirnova. A Monitor of Intermediate-Energy Neutrons Based on Thin Film Breakdown Counters, The Svedberg Laboratory, Department of Radiation Sciences, Uppsala University, Sweden. *Report series 0284-2769*, 1999.

[51] D. Cole T. Cousins R. B. Jammal E. J. Waller, T. J. Jamieson. Experimental and Computational Determination of Neutron Dose Equivalent Around Radiotherapy Accelerators. *Radiation Protection Dosimetry*, 107(4):225–232, 2003.

[52] L. Visca E. Durisi M. Perosino J.R.M. Annand A. Zanini, F. Fasolo and K.W. Burn. Test of a bubble passive spectrometer for neutron dosimetry. *Phys. Med. Biol*, 50:4287–4297, 2005.

[53] M. P. Indiguez H. R. Vega M. Voytchev R. Barquero, R. Mendez. Thermoluminescence Measurements of Neutron Dose Around Medical Linac. *Radiation Protection Dosimetry*, 101(1-4):493–496, 2002.

[54] Z. Wang J. Hutchinson G. D. Fullerton R. M. Howell, N. E. Hertel. Calculation of effective dose from measurements of secondary neutron spectra and scattered photon dose from dynamic mlc imrt for 6 mv, 15 mv, and 18 mv beam energies. *Medical Physics*, 33(2):360–368, 2006.

[55] A. J. J. Bos F d'Errico, M. Matzke. Passive Detectors for Neutron Personal Dosimetry: State of the Art.

[56] R. E. Apfel. Superheated drop detector: A possible alternative for neutron dosimetry. *Nucl. Instrum. and Meth.*, 162:603–608, 1979.

[57] T. Koble G. Kruzinzki P. Thesing G. Jaunich H.-L. Kronholz W. Rosenstock, J. Schulze. Estimations of Neutron Energy Spectra With Bubble Detectors: Potential and Limitations. *Radiation Protection Dosimetry*, 61(1-3):133–136, 1995.

[58] T. D. McLean H. Ing, R.A. Noulty. Bubble Detector - A Maturing Technology. *Radiation Measurements*, 27(1):1–11, 1997.

[59] M. Matzke F. d'Errico. Neutron Spectrometry in Mixed Fields: Superheated Drop (Bubble) Detectors. *Radiation protection dosimetry*, 107:111–124, 2003.

[60] M.J. Harper and M.E. Nelson. Experimental Verification of a Superheated Liquid Droplet (Bubble) Neutron Detector Theoretical Model. *Radiat Prot Dosimetry*, 47(1-4):535–542, 1993.

[61] F. Seitz. On the theory of the bubble chamber. *Physics of Fluids*, 1(1):2–13, 1958.

[62] P. Spiegler A. Norman. Radiation Nucleation of Bubbles in Water. *Nuclear Science and Engineering*, 16:213–17, 1963.

[63] BTI Bubble Technology Industires. Personal Communication. 5th of October, 2009.

[64] BTI Bubble Technology Industries. BTI Bubble Detector Spectrometer BDS. For Low Resolution Neutron Spectroscopy. BDS MANUAL, 2009.

[65] A. J. M. Plompen E. Wattecamps H. Thierens. F. Vanhavere, M. Loos. A combined use of the bd-pnd and bdt bubble detectors in neutron dosimetry. *Radiation Measurements*, 29:573–577, 1998.

[66] BTI Bubble Technology Industries. BDS and BDT Calibration Certificate. BDS CALIBRATION SHEET, 2009.

[67] T. Cousins M. A. Bucknert, R. A. Noulty. The Effect of Temperature Threshold on the Neutron Energy Threshold of Bubble Technology Industries' Bubble Detectors Spectrometer. *Radiation Protection Dosimetry*, 55(1):23–30, 1995.

[68] H. Ing. Neutron Measurements Using Bubble Detectors - Terrestrial and Space. *Radiation Measurements*, 33:275–286, 2001.

[69] A. Scharmann M. Oberhofer. *Applied Thermoluminescence Dosimetry*. Adam Hilger Ltd, Bristol, 1979.

[70] Harshaw TLD Products, Thermo Scientific . http://www.thermo.com/com/cda/product/detail/0,1055,22706,00.html, 21/10/2009.

[71] S. Freeman Y.S. Horowitz. Response of LiF-6 and LiF-7 Thermoluminescent Dosimeters to Neutrons Incorporating the Thermoluminescent Linear Energy Transfer Dependency. *Nuclear Instruments and Methods*, 157:393–396, 1978.

[72] Use of TLD at CERN, RADMON meeting. M. Silari, J. Wolf (SC/RP), 22/7/2004.

[73] Institute for Energy Technology - IFE. http://www.ife.no, 10/12/2009.

[74] Nuclear Physics and Reactor Theory. *U.S. Department of Energy, Washington, D.C.*, volume 1. National Technical Information Services, U.S. Department of Commerce, Port Royal Springfield, 1993.

[75] National Physical Laboratory NPL. Kay and Laby. Tables of Physical and Chemical Constants, S. Bennet, M. Sene, O. C. Jones, D. Craston, http://www.kayelaby.npl.co.uk, 2004,.

[76] V. V. Verbinski, Hans Weber, and R. E. Sund. Prompt Gamma Rays from $U235(n,f)$, $Pu239(n,f)$, and Spontaneous Fission of $Cf252$. *Phys. Rev. C*, 7(3):1173–1185, Mar 1973.

[77] Sverre Hval, Institute for Energy Technology. Personal Communication, Nov 2009.

[78] Buchillier et al. Calibration and Testing of a TLD Dosemeter for Area Monitoring. *Radiation protection dosimetry*, 110(14):705, 2004.

[79] N. E. Hertel K. G. Veinot. Effective quality factors for neutrons based on the revised ICRP/ICRU recommendations. *Radiat Prot Dosimetry*, 115(1-4):536–541, 2005.

Appendix A

Unfolding the Bubble Detector Spectrum

The bubble detectors' energy spectrum is unfolded using a the method called 'spectral striping'. The upper regions are calculated prior to the lower bins. Due to this, the method is known to suffer from error accumulation, especially in the lower energy bins which' value depend on the higher bins. Unfolding of the data from the bubble detector spectrometer is based on a number of assumptions [64]:

1. The derived unfolded spectrum can be adequately approximated by a 6-region histogram.
2. The energy of the detected neutrons do not exceed 20 MeV.
3. Fluence per unit energy is constant over the histogram interval.

Calculations:

1. Number of bubbles in each detector, (A_i), is determined.
2. A_i is normalized by dividing by the sensitivity of the current detector. This obtains the standardized response, R_i.
$$R_i = \frac{A_i}{(sensitivity)_i} \tag{A.1}$$
3. Average all the standardized responses for each threshold. This gives six averaged responses where R_1 corresponds to BDS-10, R_2 corresponds to BDS-100 and so on.
4. The neutron fluence in each energy interval, N_i can then be calculated by using the cross sections in various energy intervals given in table A.1.

$$R_6 = \sigma_{66} \times N_6 \tag{A.2}$$

which gives

$$N_6 = \frac{R_6}{\sigma_{66}} \tag{A.3}$$

where σ_{66} is the average response of the BDS-10000 detector over the interval 10 - 20 MeV. N_6 is the total fluence between 10 - 20 MeV.

5. When N_6 is determined it is possible to determine the fluence in the next interval:

$$R_5 = \sigma_{55} \times N_5 + \sigma_{56} \times N_6 \tag{A.4}$$

which leads to

$$N_5 = \frac{R_5 - \sigma_{56} \times N_6}{\sigma_{55}} \tag{A.5}$$

Following this pattern, equations for the remaining energy intervals can also be deduced

$$N_4 = \frac{R_4 - \sigma_{45} \times N_5 - \sigma_{46} \times N_6}{\sigma_{44}} \tag{A.6}$$

$$N_3 = \frac{R_3 - \sigma_{34} \times N_4 - \sigma_{35} \times N_5 - \sigma_{36} \times N_6}{\sigma_{33}} \tag{A.7}$$

$$N_2 = \frac{R_2 - \sigma_{23} \times N_3 - \sigma_{24} \times N_4 - \sigma_{25} \times N_5 - \sigma_{26} \times N_6}{\sigma_{22}} \tag{A.8}$$

$$N_1 = \frac{R_1 - \sigma_{12} \times N_2 - \sigma_{13} \times N_3 - \sigma_{14} \times N_4 - \sigma_{15} \times N_5 - \sigma_{16} \times N_6}{\sigma_{11}} \tag{A.9}$$

In certain histogram intervals, there may be some or very few neutrons in the source spectrum. Under such circumstances, the value of N_i may come out as negative in the unfolding procedure due to statistical uncertainty. In such situations, the value of N_i should be set to zero, and is referred to as 'non-negativity'.

6. The total fluence, $\Phi[n/cm^2]$, over the time of detector exposure is given by

$$\Phi = \sum_{n=1}^{6} N_i \tag{A.10}$$

Table A.1: Average cross sections of BDS over various energy ranges $[\frac{bubble}{n.cm^{-2}}]$ [64].

Detector I.D.	J =	1	2	3	4	5	6
	MeV	(0.01 - 0.1)	(0.1 - 0.6)	(0.6 - 1)	(1 - 2.5)	(2.5 - 10)	(10 - 20)
BDS-10	1	5.00×10^{-6}	2.50×10^{-5}	2.92×10^{-5}	2.97×10^{-5}	4.15×10^{-5}	4.78×10^{-5}
BDS-100	2	-	2.27×10^{-5}	3.14×10^{-5}	3.23×10^{-5}	4.47×10^{-5}	5.09×10^{-5}
BDS-600	3	-	-	1.60×10^{-5}	3.27×10^{-5}	4.75×10^{-5}	5.45×10^{-5}
BDS-1000	4	-	-	-	1.32×10^{-5}	3.50×10^{-5}	5.90×10^{-5}
BDS-2500	4	-	-	-	-	2.99×10^{-5}	8.70×10^{-5}
BDS-10000	4	-	-	-	-	-	4.35×10^{-5}

Appendix B

Unfolding TLD Response

To unfold the TLD response, two steps are performed [78]:

(1)

The photon response for TLD-600 is lower than that of TLD-700. This is expressed as variable $k = R_{700}/R_{600}$, and retrieved by irradiating both types in a neutron-free photon field. Having obtained k, the the neutron response, R^n, can be unfolded in a mixed photon neutron field:

$$R^n = R_{600}^{n+\gamma} - \frac{R_{700}^{n+\gamma}}{k}. \tag{B.1}$$

$R_{600}^{n+\gamma}$ and $R_{700}^{n+\gamma}$ refers to the response of TLD-600 and TLD-700, respectively, exposed to a mixed photon neutron field.

(2)

For converting the signal in nC to dose, D, the TLDs must be exposed to a known neutron source.

Appendix C

Neutron Conversion Factors

Table C.1: Fluence to dose conversion factors [79].

Energy interval [MeV]	Fluence-to-dose factor [$pSv\,cm^2/n$]
0.01 - 0.1	31.2
0.1 - 0.6	215.4
0.6 - 1	396.2
1 -2.5	445.3
2.5 - 10	437.25
0.025×10^{-6} (thermal)	11.3

Appendix D

Measurement Data

D.1 Calibration Data

Table D.1: Response of the BDS detectors exposed to a thermal neutron fluence of 1.3×10^6n.cm^{-2} in the field the nuclear reactor. The response in bubbles correspond to neutron doses on the order of mSv.

Detector type	Response [bubbles]
BDS 10	81
BDS 100	87
BDS 600	143
BDS 1000	243
BDS 2500	281
BDS 10 000	15

Photon Calibration in the Isocenter of a 6 MV Field

BDT and TLD in-phantom measurements were also performed in the isocenter of the 6 MV linac field. This was in order to relate the response of the detectors to the linac calibrated photon dose. The results are shown in Table D.2. The results show that the BDTs are sensitive to photons at high dose rates: 10 bubbles per Gy. Measurements performed outside the field does not produce bubbles.

Table D.2: Photon calibration performed in-phantom in a 6 MV linac beam.

Detector	Response
BDT	10±1 bubbles/Gy
TLD-600	5400±100 nC/Gy
TLD-700	3400±200 nC/Gy

D.2 Dose Plan Neutron Measurements

Table D.3: BDS fluence in intervals of the neutron energy spectrum during the 3D-CRT and IMRT treatment plans.

Energy interval [keV]	3D-CRT Fluence [n.$cm^{-2}Gy^{-1}$]	IMRT Fluence [n.$cm^{-2}Gy^{-1}$]	IMRT/3D-CRT
10-100	1.7×10^7	2.9×10^7	1.7
100-600	4.7×10^5	2.5×10^6	5.3
600-1000	3.1×10^6	8.0×10^6	2.6
1000-2500	4.3×10^5	9.0×10^5	2.1
2500-10 000	6.2×10^5	1.5×10^6	2.4
Total	$(2.2\pm1.4)\times10^7$	$(4.2\pm3.6)\times10^7$	1.9

Table D.4: BDS equivalent dose in intervals of the neutron energy spectrum during the 3D-CRT and IMRT treatment plans.

Energy interval [keV]	3D-CRT Dose [mSv/Gy]	IMRT Dose [mSv/Gy]	IMRT/3D-CRT
10-100	0.54	0.89	1.7
100-600	0.10	0.53	5.3
600-1000	1.23	3.17	2.6
1000-2500	0.19	0.40	2.1
2500-10 000	0.27	0.65	2.4
Total	2.3±1.5	5.6±4.8	2.4

BDS Uncertainty

Table D.5: Estimated theoretical uncertainty in the BDS fluence energy spectrum for the 3D-CRT and IMRT data. Calculated as described in Section E.

Energy interval [keV]	3D-CRT [%]	IMRT [%]
10-100	81	122
100-600	461	221
600-1000	42	39
1000-2500	44	55
2500-10 000	10	9
Total	64	86

Appendix E

Theoretical Uncertainty

The uncertainties in this work are estimated from the root-mean-square (rms) values obtained from the reproducibility measurements. These uncertainties are the theoretical estimates, and the uncertainties in the results are expected to also include other factors not considered in this calculation.

The rms value is obtained using the following formula:

$$\sigma = \sqrt{\frac{1}{N}\sum_{i=1}^{N}(x_i - \bar{x})^2} \tag{E.1}$$

Propagation of Errors

Most of the results obtained in this work are a combination of several detector units and must be unfolded by combining the results of the various segments. The combined uncertainty σ_z of value z consists of quantities x and y each having associated errors σ_x and σ_y. Assuming the values are not correlated, following formulas have been used depending on the relation of x and y:

Sums and Differences

$$\sigma_z = \sqrt{(\sigma_x)^2 + (\sigma_y)^2} \tag{E.2}$$

Multiplication and Division

$$\sigma_z = z \times \sqrt{\left(\frac{\sigma_x}{x}\right)^2 + \left(\frac{\sigma_y}{y}\right)^2} \tag{E.3}$$

BDS Error Propagation

The unfolding procedure of the BDS spectrum is known to suffer from error accumulations, especially affecting the lower energy regions of the spectrum.

The theoretical uncertainties in the various energy intervals are calculated as follows [6]:

The error propagation of a function, f, depending on the variables x_1, x_2 and x_3, and assuming non-correlated data, the uncertainty is then given by:

$$\sigma_f^2 = \left(\frac{\partial f}{\partial x_1}\right)^2 \times \sigma_{x_1}^2 + \left(\frac{\partial f}{\partial x_2}\right)^2 \times \sigma_{x_2}^2 + \left(\frac{\partial f}{\partial x_3}\right)^2 \times \sigma_{x_3}^2 \tag{E.4}$$

This formula is used in estimating the theoretical uncertainty in each individual energy interval for the neutron spectra obtained with the BDS detectors. As the contribution of neutrons with energies above 10 MeV were negligible, the highest region, N_6, is empty. This leads to the uncertainty in the highest fluence interval (1 MeV - 2.5 MeV) is given by:

$$\sigma_{N_5} = \frac{\sigma_{R_5}}{s_{55}} \tag{E.5}$$

$$N_4 = \frac{R_4 - s_{45} \times N_5}{s_{44}} \tag{E.6}$$

$$\sigma_{N_4}^2 = \left(\frac{\partial N_4}{\partial R_4}\right)^2 \times \sigma_{R_4}^2 + \left(\frac{\partial N_4}{\partial N_5}\right)^2 \times \sigma_{N_5}^2 \tag{E.7}$$

Applying equation A.6 yields

$$\sigma_{N_4}^2 = \left(\frac{\sigma_{R_4}}{s_{44}}\right)^2 + \left(\frac{s_{45}\sigma_{N_5}}{s_{44}}\right)^2 \tag{E.8}$$

In the same procedure equations for σ_{N_3}, σ_{N_3}, σ_{N_2} and σ_{N_1} are obtained

$$\sigma_{N_3}^2 = \left(\frac{\sigma_{R_3}}{s_{33}}\right)^2 + \left(\frac{s_{34}\sigma_{N_4}}{s_{33}}\right)^2 + \left(\frac{s_{35}\sigma_{N_5}}{s_{33}}\right)^2 \tag{E.9}$$

$$\sigma_{N_2}^2 = \left(\frac{\sigma_{R_2}}{s_{22}}\right)^2 + \left(\frac{s_{23}\sigma_{N_3}}{s_{22}}\right)^2 + \left(\frac{s_{24}\sigma_{N_4}}{s_{22}}\right)^2 + \left(\frac{s_{25}\sigma_{N_5}}{s_{22}}\right)^2 \tag{E.10}$$

$$\sigma_{N_1}^2 = \left(\frac{\sigma_{R_1}}{s_{11}}\right)^2 + \left(\frac{s_{12}\sigma_{N_2}}{s_{11}}\right)^2 + \left(\frac{s_{13}\sigma_{N_3}}{s_{11}}\right)^2 + ... \tag{E.11}$$

Appendix F

Kjeller Neutron Flux

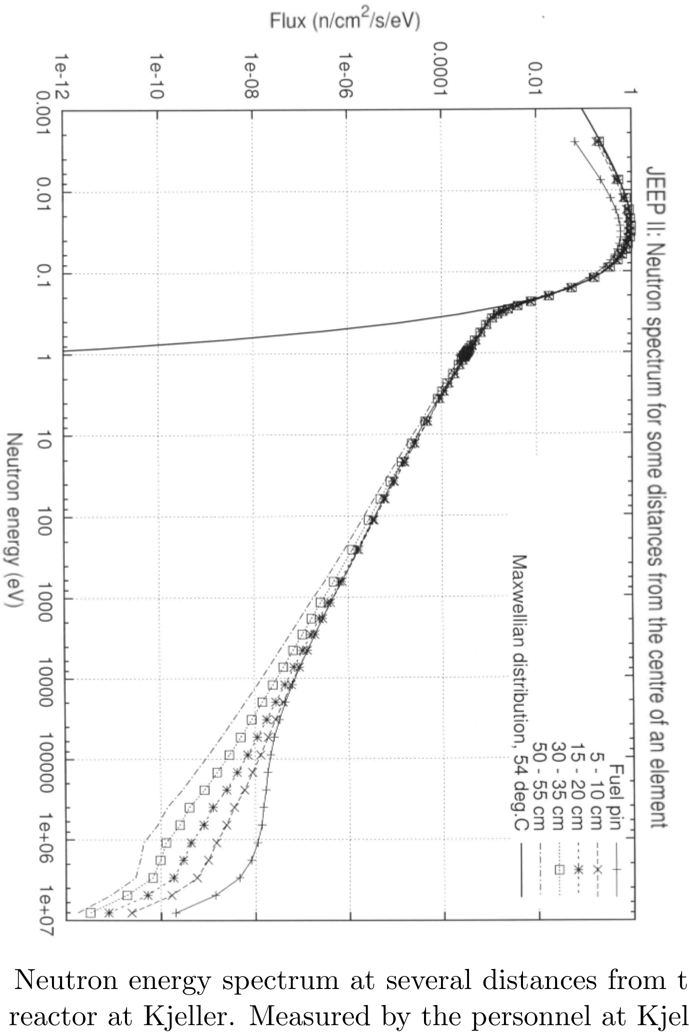

Figure F.1: Neutron energy spectrum at several distances from the core of the nuclear reactor at Kjeller. Measured by the personnel at Kjeller.

Appendix G

Particle Therapy Facilities

Table G.1: Carbon therapy facilities in operation [27]. *Patients treated at the end of October 2007.

Center	Start of treatment	♯ patients treated
HIMAC, Chiba, Japan	1994	4504
GSI Darmstadt, Germany	1997	384*
HIBMC, Hyogo, Japan	2002	454
TOTAL		5342

Table G.2: Proton therapy facilities in operation [6, 27].

Center	Start of treatment	♯ patients treated
ITEP, Russia	1969	4024
St.Petersburg, Russia	1975	1327
PSI, Switzerland	1984	5076
Dubna, Russia	1999	489
Uppsala, Sweden	1989	929
Clatterbridge, England	1989	1803
Loma Linda, CA, USA	1990	13500
Nice, France	1991	3690
Orsay, France	1991	4497
iThemba labs, South Africa	1993	503
MPRI, IN, USA	2004	632
UCSF, CA, USA	1994	1113
Triumf, Vancouver, Canada	1995	137
PSI, Switzerland	1996	426
HZB Berlin, Germany	1998	1227
NCC, Kashiwa, Japan	1998	607
HIBMC, Hyogo, Japan	2001	2033
PMRC, Tsukuba, Japan	2001	1367
NPTC, Boston, USA	2001	3515
INFN-LNS, Catania, Italy	2002	151
Shizuoka, Japan	2003	692
WERC, Tsuruga, Japan	2002	56
WPTC, Zibo, China	2004	767
MD Anderson, TX, USA	2006	1000
FPTI, FL, USA	2006	988
NCC, South Korea	2007	330
TOTAL		61122

Table G.3: Particle therapy centers under construction or in a planning stage [27].

Center	Particle	Planned opening
Med-Austron, Austria	p, C-ion	2013
CNAO, Pavia, Italy	p, C-ion	2010
HIT, Heidelberg, Germany	p, C-ion	2009
PTC, Marburg, Germany	p, C-ion	2010
NRoCK, Kiel, Germany	p, C-ion	2012
Maebashi, Japan	C-ion	2010
RPTC, Munich, Germany	p	2009
PSI, Switzerland	p	2009
UPenn, PA, USA	p	2010
Trento, Italy	p	2011
iThemba Labs, South Africa	p	-
RPTC, Köln, Germany	p	-
WPE, Essen, Germany	p	2009
CPO, Orsay, France	p	2010
Chicago, IL, USA	p	2010
Taipei, Taiwan	p	2011
Oklahoma City, OK, USA	p	2009
Hampton, VA, USA	p	2010
PMHPTC Protvino, Russia	p	2010
CCRS, Bratislava, Slovak. Rep.	p	2010
Ruzomberok, Slovak. Rep.	p	2010
SJFH, Beijing, China	p	2010
Skandion Clinic, Uppsala, Sweden	p	2012